2018

The Microstructural Annealing Response of Cold Gas Dynamically Sprayed Al 6061

Clayton Andrew Cushway
University of North Florida, n00718983@ospreys.unf.edu

The Microstructural Annealing Response of Cold Gas Dynamically Sprayed Al 6061

by

Clayton Cushway

A thesis submitted to the School of Engineering

in partial fulfillment of the requirements for the degree of

Master of Science in Mechanical Engineering

University of North Florida

COLLEGE OF COMPUTING, ENGINEERING, and CONSTRUCTION

December 2018

The thesis "The Microstructural Annealing Response of Cold Gas Dynamically Sprayed Al 6061" submitted by Clayton Cushway in partial fulfillment of the requirements for the degree of Master of Science in Mechanical Engineering has been

Approved by the thesis committee: **Date**

_____ _____

Dr. Paul Eason

Thesis Advisor and Committee Chairperson

_____ _____

Dr. Murat Tiryakioğlu

_____ _____

Dr. Stephen Stagon

Accepted for the School of Engineering:

_____ _____

Dr. Osama Jadaan
Director of the School of Engineering

Accepted for the College of Computing, Engineering, and Construction:

_____ _____

William F. Klostermeyer

Dean of the College

Accepted for the University:

_____ _____

Dr. John Kantner

Dean of the Graduate School

Dedication

This thesis is dedicated to my Fiancée Rachel Mattoon for her

continued love and support throughout this adventure.

Acknowledgments

I would like to thank my advisor and committee chair Dr. Paul Eason, for introducing me to research and helping me along my path through graduate school. I would also like to thank Dr. Stephen Stagon and Dr. Murat Tiryakioğlu for their knowledge and advice over the time that I have known them. Finally, I would like to thank UNF for my time and growth as a student and their support for the Material Science and Engineering Research Facility (MSERF).

Table of Contents

List of Figures

List of Tables

Symbols and Abbreviations

AR - As Received

AS - Arc Spraying

BCC - Body Centered Cubic

BSE - Backscatter Electron

CS - Cold Gas Dynamic Spray

DE - Deposition Efficiency

DG - Detonation Gun

ECAP - Equal Channel Angular Pressing

EBSD - Electron Backscatter Diffraction

EBSP - Electron Backscatter Pattern

FCC - Face Centered Cubic

FEG - Field Emission Gun

FSP - Friction Stir Processing

HCP - Hexagonal Closed Packed

HT - Heat Treated

HV - Vickers Microhardness

HVOF - High Velocity Oxygen Fuel

IPF - Inverse Pole Figure

PD - Packing Density

PFS - Powder Flame Spraying

PS - Plasma Spray

SE - Secondary Electron

SEM - Scanning Electron Microscope

SPD - Severe Plastic Deformation

TS - Thermal Spray

UFG - Ultra-Fine Grains

WFS - Wire Flame Spraying

Abstract

The Cold-Gas Dynamic-Spray process also known as Cold Spray (CS) has been researched for three decades. The CS process is a solid-state deposition technique via supersonic velocity of powder particles at a temperature significantly below the melting point of the spray material. This thesis presents background on the overall CS process parameters, and additional information on the microstructural and mechanical properties of typical Cold Sprayed materials.

This Thesis primarily presents a study on the microstructural annealing response of CS Al 6061. It should be noted that for this study, the term “annealing” is used in the sense of the classical metallurgical definition of annealing, and not a specific temper designation for the 6061 alloy. Cross sections of CS Al 6061 were imaged with a scanning electron microscope (SEM) in secondary electron (SE), backscatter electron (BSE), and electron backscatter diffraction (EBSD) imaging mode for quantitative and qualitative information on the grain size and orientation of the CS microstructure. The detailed SE, BSE and EBSD mode images present the grain size and grain orientation of the original powder, as received (AR) state and after heat treating at 200°C for 1 hour, 10 hours, and 100 hours. Three different regions, characterized with distinctly differing microstructures, are labeled as low, medium, and high deformation regions, and their microstructures, and evolving features are discussed.

Vickers microhardness testing are performed to examine the differences in hardness values between different heat treatments, and for correlation with the level of deformation and grain refinement in the microstructure. SEM imaging was used in BSE mode to correlate microhardness variation to the different regions within the CS microstructure.

Chapter 1: Introduction

This process was first pioneered in early to mid-1980s at the institute of Theoretical and Applied Mechanics of the Russian Academy of Sciences in Novosibirsk by Dr. Anatolii Papyrin and his colleagues. The first U.S. patent of Cold Spray was issued in 1994 [1]. The Cold Spray process deposits metal powders onto a substrate using an apparatus that entrains the powder into a supersonic gas stream to deposit powder at a high impact velocity. The process imparts cold work to the substrate, and deposited powder particle from the initial and subsequent impacts, forming a heavily deformed, layered structure.

The irregular particle shape distorts the surface and results in different deformation regions in the CS microstructure. These different deformation sites require characterization to assess grain reduction and change in grain orientation from the cold work. With better understanding of the microstructure, properties of CS coatings and bulk deposits can be more accurately modeled.

1.1 Research Objectives

The scope of this project includes characterizing the Cold Spray structure of the 6061 aluminum, which includes grain size, and grain orientation. Therefore, the following research objectives were generated: To identify the annealing change in the microstructures of the aluminum Cold Spray samples for different regions, to correlate the hardness indents on the Cold Spray deformation regions, to determine anomalies that could occur during electron backscatter diffraction.

1.2 Thesis Description

Chapter 2 presents background information on the Cold Spray process and previous literature relevant to the characterization methods involved in the current study. The background includes an overview of the process and parameters used to create the microstructures that are found in the Cold Spray materials, as well as a discussion of the previous efforts to characterize the microstructure of these materials and the limitations of the methodologies used. The background also includes the annealing behavior of CS and deformed Al, and microstructural characterization of the CS regions.

Chapter 3 presents the design of experiment and experimental procedures that were used for this study, including sample preparation, characterization, and material testing. The microstructural characterization procedures included scanning electron microscopy (SEM), and electron backscatter diffraction (EBSD). The technique used for post processing of EBSD samples is described. The experimental process for microhardness testing was performed to assess the dependence of microhardness on the microstructure under the indent, and to determine the change in properties within regions of differing degrees of deformation, due to the various exposure times at an elevated temperature.

Chapter 4 presents the microstructural characterization results of the powder of the different deformation regions (low, medium, and high) within the CS samples (AR, 1 hr, 10 hr, and 100 hr). These results show correlative data between the SE, BSE, and EBSD mode images per region and sample. The data presented in chapter 4 also indicates the different average grain sizes between the low, medium, and high deformation regions, and grain growth in the high deformation regions between the AR, 1 hr, 10 hr, and 100hr. Additionally, the results of microhardness indents are presented with correlative BSE mode images per region and sample.

Chapter 5 presents conclusions drawn from the results from chapter 4 which includes the grain size, grain orientation, and microhardness data. The microhardness data results were consistent with expectations; as the amount of localized deformation increased, microhardness increased. The microhardness decreased in each deformation region the longer it was annealed, which is also consistent with expectations. A brief presentation of future works that could further the understanding of CS microstructures is included.

Chapter 2: Literature review

2.1 Background

Cold-Gas Dynamic-Spray was first developed in the early to mid-1980s at the Institute of Theoretical and Applied Mechanics of the Siberian Branch of the Russian Academy of Sciences in Novosibirsk [2]. The Cold-Gas Dynamic-Spray process also known as “Cold Spray” (CS) is a solid-state material deposition technique used to bond powder particles to a substrate. These particles deform due to the high velocity impact resulting in a large amount of plastic deformation. The velocity of these particles is governed by numerous process variables of the CS apparatus such as the geometry of the de Laval nozzle, type of process gas, temperature of gas, pressure of gas, particle size and morphology [3-15]. Other factors that will change the deposition of powder particles in the CS process are feedstock material properties, oxide films, substrate, and standoff distance [3, 4, 16]. These parameters will be discussed in detail later in the chapter.

In the CS process compressed gas enters the apparatus as powder is being released into the gas stream and flows through the de Laval nozzle to obtain a supersonic velocity. To increase the velocities through the nozzle there is sometimes a gas heater that will preheat gas temperatures in excess of 900K, according to the ideal gas law and KE = 3/2RT the velocities of the gas increases with increasing temperature [5]. The gas temperature for Cold Spray is dependent on the melting temperature of the materials. The powder particles time in the gas stream is short and does not increase the temperature of the powder above cold working [5]. Figure 1 displays a schematic of a typical CS apparatus.

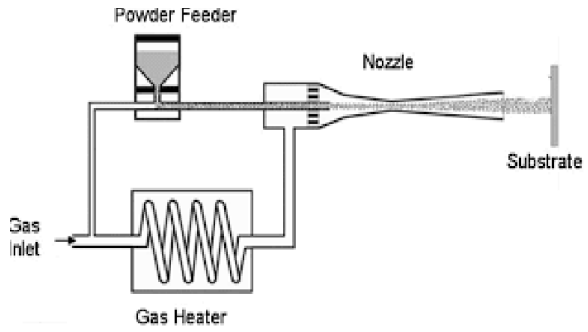

Figure 1. Schematic representation of a typical CS Apparatus [17].

2.1.1 Thermal Spray and its relation to Cold Spray

Prior to the development of CS, the preferred spray technique used for material deposition for coating applications was Thermal Spray (TS). TS employs melting of the feedstock material, which results in fusion. There are six common types of TS apparatuses; four are based on combustion process and two on electric arc. The combustion process apparatuses are Powder Flame Spraying (PFS), Wire Flame Spraying (WFS), Detonation Gun (DG), and High Velocity Oxygen Fuel (HVOF). The electric arc processes are Arc Spraying (AS), and Plasma Spray (PS) [18] . The TS combustion and the arc process are both similar in that they both melt the material being deposited to the substrate prior to deposition; feedstock melting does not occur in the CS process.

TS combustion processes use a fuel gas, (such as acetylene, hydrogen, propane, or propylene), to melt the feedstock material and propel the melted material. The electric arc process uses a DC electric arc in order to melt the feedstock material [18]. These spray coating processes are effective at applying the feedstock material to the substrate, but oxidation occurs within the process due to the high temperatures, and presence of oxygen in the carrier gas. Figure 2 shows the different TS and CS processes for the average range of velocities and temperatures reached per process [19].

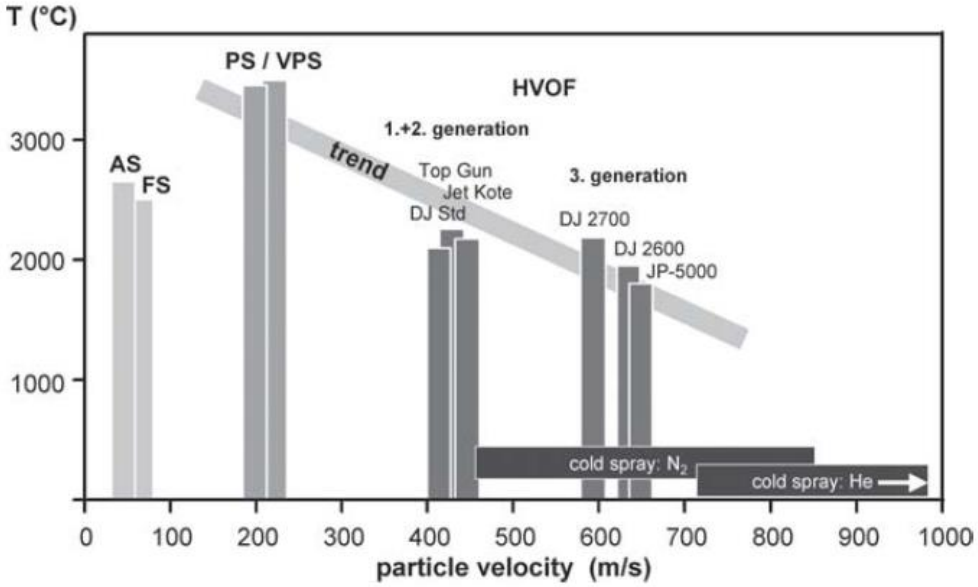

Figure 2. Particle temperatures and velocities obtained in different thermal spray and cold spray processes, as a measure of high density materials. The trend bar is of recent developments in the spray process. [19].

2.1.2 Cold Spray Applications

The CS process offers a large range of applications that include; metal restoration and sealing, thermal barriers, heat dissipation, electrically conductive coatings, dielectric coatings, localized corrosion protection, additive manufacturing, and more [18, 20-24]. One of the greatest advantages of CS is the ability to deposit feedstock material without any thermally induced phase transformations in either the feedstock or substrate; this is due to the feedstock material being heated below the melting temperatures, thus solid state deformation can occur [1].

Other benefits to CS include, high density compaction, minimal surface preparation, building of multilayer deposits, no undesirable chemical reactions, waste powder can be recycled, reduction in material input and the future elimination of mold and melt pour costs with increasing CS technology [18, 20]. These benefits can help produce more economically and

environmentally friendly parts. For example when magnesium (Mg) rotorcraft components are damaged from corrosion the part can be restored with Mg by utilizing CS rather than replacement of the entire component at significant cost [22]. Example of the CS application also includes applying corrosion resistant layer of aluminum to create a corrosion resistant barrier, thus extending the service life of a part [22].

2.2 Parameters of Cold Spray Process

The most important parameter for successful CS is the velocity of the particles; therefore parameters relating to the velocity affect the particle deposition efficiency (DE) which is a measure of success. The velocity is the most direct indicator of DE, therefore the parameters that affect velocity are of the most important. Parameters that change the velocity include the geometry of the de Laval nozzle, type of process gas, temperature of gas, pressure of gas, particle geometry, and particle size [3-14].

A critical velocity range must be maintained for the particles to bond, or else the particles at a velocity significantly lower or higher than critical velocity range can either ricochet or cause erosion to the surface [7]. To maintain these critical values the parameters that effect velocity of the CS process can be altered to achieve the critical velocity range. These parameters will be discussed in detail in individual sections.

2.2.1 De Laval Nozzle

Numerous studies have been performed on the fluid dynamic of converging nozzles. The de Laval nozzle (Figure 3) is a convergent-divergent nozzle that allows for the particle to approach high velocities of up to 1200 m/s [1]. In the literature four different nozzle geometries, nozzles A, B, C, and D (Table 1) were compared; in nozzle A and C the expansion ratio (i.e., the

exit cross section divided by the throat cross section) has a ratio of 6, while the expansion ratio in B and D has a ratio of 9. Figure 4 shows the DE based on the study of the different expansion ratio and nozzle geometries shown in Table 1 for nozzles A, B, C, and D [5].

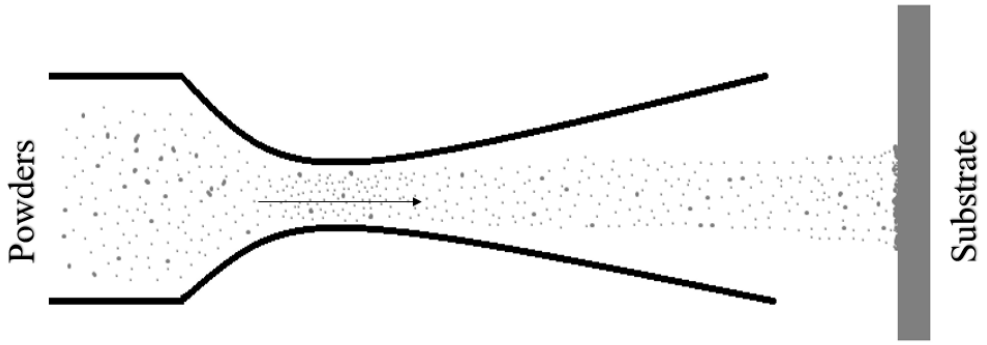

Figure 3. Schematic of De Laval nozzle drawing for a CS apparatus, the arrow represents the direction of flow.

Table 1. Change in geometry of two different nozzle geometries (conical) A, B, and (bell shaped) C, and D. Data attained from literature [5].

Nozzle	Expansion ratio	Divergent Section Shape	Length ratio
A	6	Conical	Set Length
B	9	Conical	B = A
C	6	Bell Shaped	C = 1.5*A
D	9	Bell Shaped	D = 1.8*A

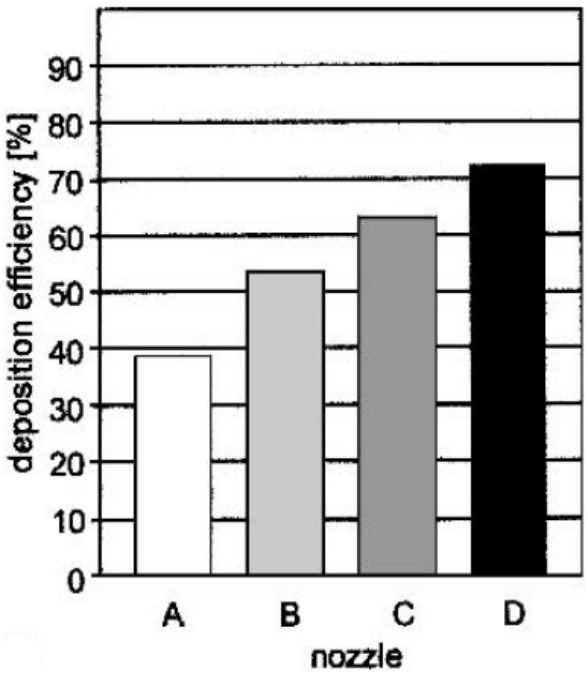

Figure 4. Deposition efficiency for CS of Cu with four different nozzle geometries A, B conical and C, and D bell shaped [5].

Fluid dynamic calculations suggest that boundary layer phenomena lead to a significant loss in energy for narrower nozzles. Wider nozzles minimize the boundary layer influence and may increase the particle velocity up to 60 m/s [6]. In one study, a theoretical comparison between a trumpet-shaped nozzle and a bell-shaped nozzle with nitrogen as the process gas at an inlet pressure of 30 bars and gas temperature of 320℃. The bell-shaped nozzle typically results in exit velocities greater than 50 m/s with respect to the trumpet-shaped nozzle for different particle sizes. Studies have proven that the bell-shaped nozzle is better for deposition compared to the trumpet-shaped [7, 8].

2.2.2 Process Gas

There are three commonly used gases used for the CS process; air, helium (He) and nitrogen (N_2) [3, 4]. The pressure and temperature of the process gas along with the type of gas will change the particle velocity. The most readily available and economically feasible process gas is air. But due to the higher density of air with respect to other process gases, air produces a lower DE at the same process conditions as N_2 or He. He provides a higher DE and lower porosity at the same process conditions than air or N_2. However, He is more expensive, due to the added expense of recovery and recapture of the gas given the current worldwide shortage [3].

Other parameters of the process gas include the pressure and temperature of the gas. Figure 6 compares the DE of Cu particles, in process gas air, to the (a) change in pressure and (b) change in temperature. These two graphs show that a reasonable DE for air is still achievable with air as the process gas. The graphs show that the temperature has a higher effect on DE than the inlet gas pressure [5].

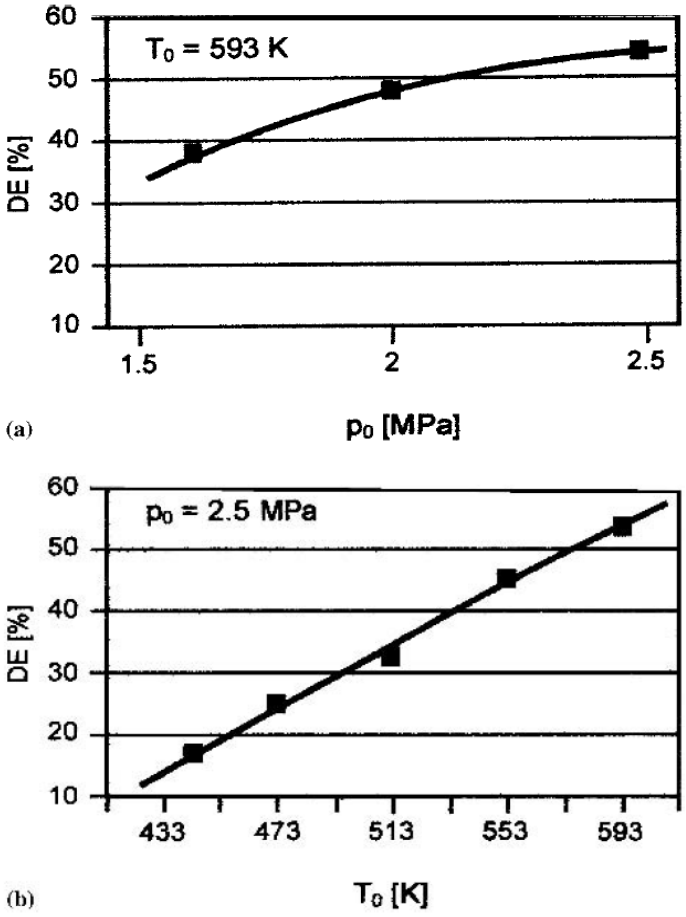

Figure 5. Influence of (a) gas pressure (b) gas temperature on the deposition efficiency of Cu-powder ranging in size from 5-25 µm, a spray distance of 30mm, and a standard nozzle B (shown in Table 1) [5].

Figure 6 is a comparison between DE versus the gas temperature as well as the particle velocity for both He and N_2. In the data, the comparison between the two types of gases exhibit an increase in DE and mean particle velocity for the He gas [4]. A higher velocity acquired for bonding is more easily achievable with He. The velocity range will be discussed in greater detail in section 2.2.5.

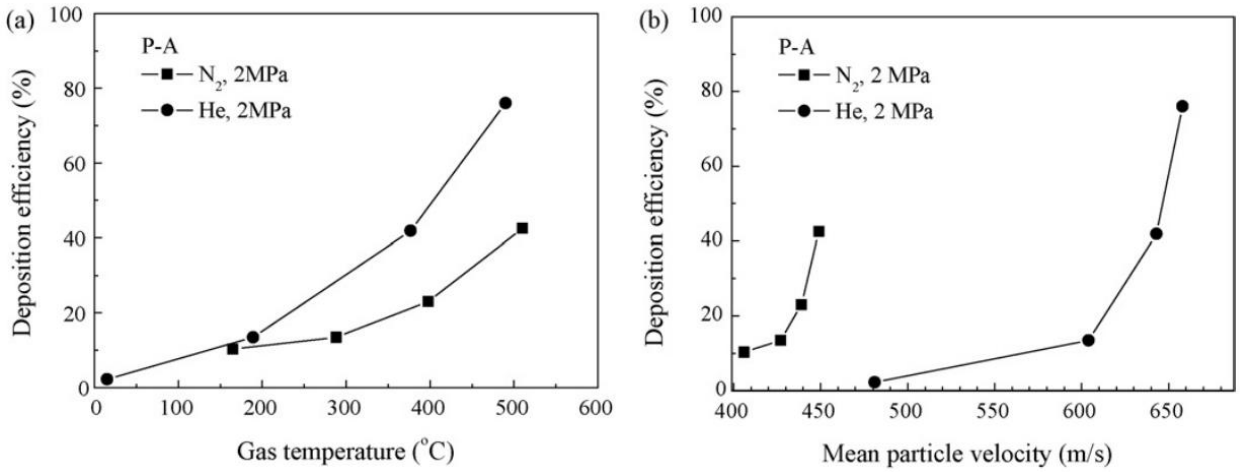

Figure 6. (a) Effect of the gas temperature and type on deposition efficiency and (b) change of deposition efficiency with mean particle velocity for N_2 and He at 2MPa [4].

2.2.3 Effect of particle characteristics on the Cold Spray Process

The particle morphology, size, crystal structure, and the powder production method are all important factors to consider when using CS. The morphology of a particle has an effect on both the drag force of the particle and the velocity before impact. The manufacturing process of the particles can affect, the geometry, size, and how much oxidation occurs to each particle [10-14, 16, 25].

Figure 7 shows images of 2618 Aluminum powders produced by atomization (a) and as-cryomilled (b). The gas atomized powders are more spherical in shape and the as-cryomilled is more irregular.

Table 2 shows the average particle velocity for two different types of powders as well as two different powder size ranges sprayed. This demonstrated that both the morphology and the size of the particle will affect the particle's velocity [10]. Similar results were obtained in a study between gas atomized and dendritic porous electrolytic Ni powders [12].

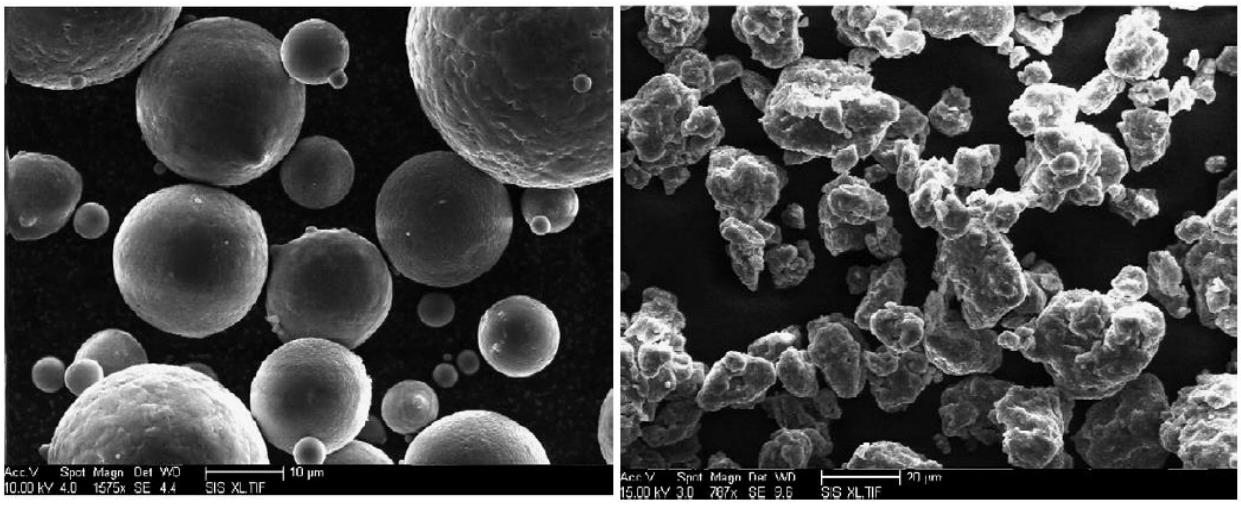

(a) (b)

Figure 7. SEM micrograph taken in SE mode for 2618 Al as-atomized powder (a) as-cryomilled powder (b) [10].

Table 2. Average particle velocity measure for two different powder morphologies (as-atomized and as-cryomilled) and two different powder size ranges (d = particle diameter) [10].

Powder morphology and size range	Measured velocity (m/s)
As-atomized, $d<25$ µm	747±120
As-cryomilled, $d<25$ µm	790±150
As-atomized, 25 µm$<d<$38 µm	641±98
As-cryomilled, 25 µm$<d<$38 µm	716±132

In Figure 8 images of two different gas-atomized Al powders can be seen; the main difference between these two gas-atomized powders is morphology. The Valimet H-20 powder has more of a spherical shape with an average particle size of 25 µm. The Brodmann Flomaster powder has both a spherical and globular shapes with an average particle size of 26 µm. The difference in particle morphology demonstrates that the gas atomization process does not produce a specific morphology [13].

Table 2 shows the differences in velocity of particles based on morphology and size.

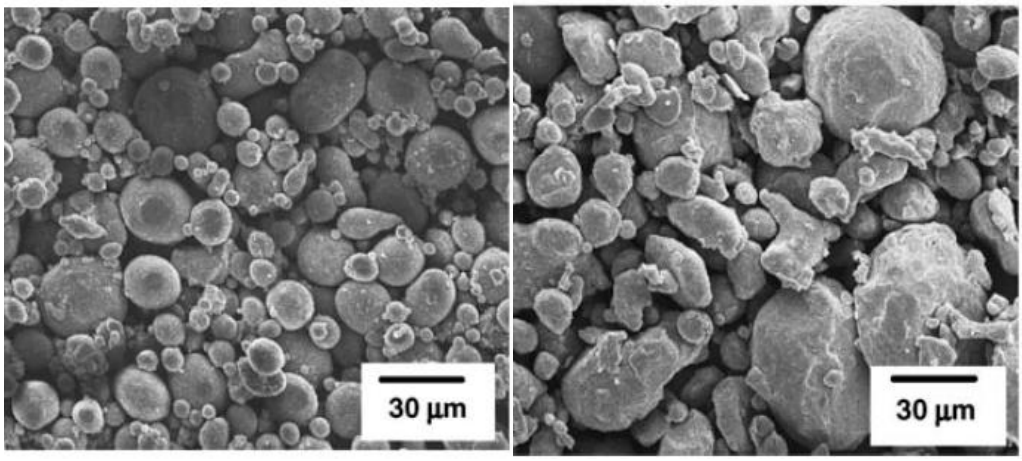

(a) (b)

Figure 8. SEM micrograph taken in SE mode of Valimet H-20 powder (a) and Brodmann Flomaster powder (b) with 30 µm scale bars [13].

Experiments conducted between two different titanium (Ti) commercially pure powders were produced in spherical and globular morphologies. The average particle diameters for the powders were 29 µm and 63 µm for spherical and globular. The average velocities ranged from 608 to 805 m/s for spherical and 652 to 859 m/s for globular, staying consistent with the globular geometry having a higher velocity. Figure 9 shows the overall effects of carrier gas, temperature, and the pressure on the spherical and globular particle velocity. This study explains that as the temperature of the gas increased so did the particle velocity. Figure 10 shows the percentage of porosity versus the velocity of spherical or globular particles compared to that of bulk Ti. The spherical powders produced coatings typically having less porosity than that of the globular powder produced coatings. The CS coatings produced from spherical powder had lower porosity than CS coatings produced from globular powder [14].

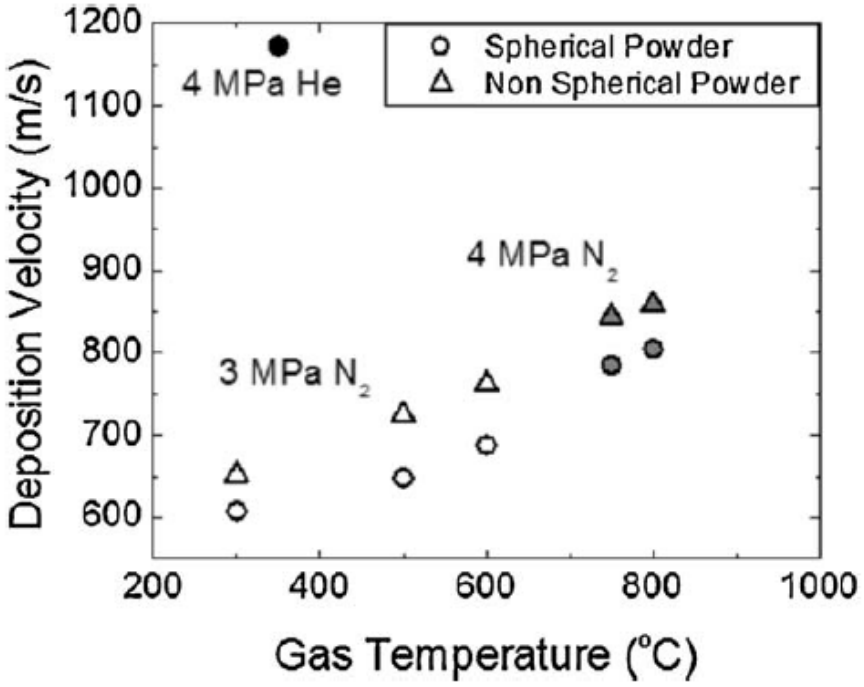

Figure 9. Effect of the carrier gas, temperature, and pressure on the spherical and globular particle velocity with the spherical and non-spherical powder. In open circle and triangle being N_2 being sprayed at 3 MPa, the filled circle and triangle N_2 at 4 MPa, and the black dot shows He sprayed at 4 MPa [14].

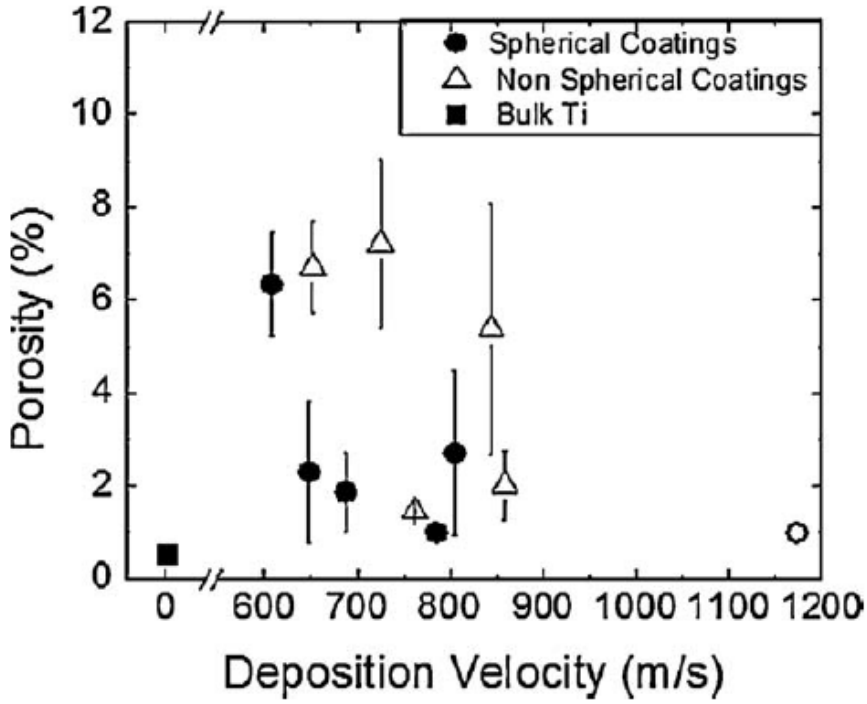

Figure 10. Deposition velocity with respect to porosity percentage. The spherical coatings deposited with N2 are plotted as filled circles while the spherical coating deposited with He gas is plotted as an open circle. Closed square represents Bulk Ti, filled sphere shows spherical coating, and open triangle is non-spherical coatings [14].

While the size and geometry of the particle are both important characteristics, the crystal structure of the material becomes important in deformation and plays the largest role in the critical velocity that is needed to apply the coating to the substrate. The material's crystal structure influences the mobility of the dislocations and the interactions that occur during the deformation process. The deformation is also associated with other parameters such as grain size and phases within the material. There are many metals used in CS; the metals can be easily classified into different isomechanical groups. Isomechanical groups have similar mechanical properties and are sorted by crystal structure. Three isomechanical groups that have been observed for CS include face-centered cubic (FCC), body-centered cubic (BCC), and hexagonal close-packed (HCP) [16].

The FCC metals are usually easier to deform due to a packing density (PD) of .74 and a large number of slip planes. The HCP metals are the second easiest to deform due to a PD of .74 with a reduced number of slip planes than FCC metals. The BCC metals are the hardest of the three groups to deform due to a lower PD of .68 and typically requires more energy to activate screw dislocation movement [16]. Therefore, the FCC materials typically exhibit higher deformation within the microstructure, due to the large number of slip planes than HCP and BCC.

2.2.4 Cold Spray Process Geometry and Other Parameters

The geometry of the CS apparatus includes the tilt angle and the standoff distance, distance from the nozzle exit to the substrate. Other parameters of the process include the feed rate of the powder into the gas stream, and the traverse intervals [3, 26]. The powder feed rate influences the total mass fraction between the gas and particle, reducing or increasing the amount

of powder that is feed into the gas stream [3]. The traverse intervals (number of spray cycles) changes the thickness of the CS sample [26].

A comparison between the angled and normal impact (Figure 11), suggests that an angled impact is more beneficial for a higher DE at lower velocities [3].

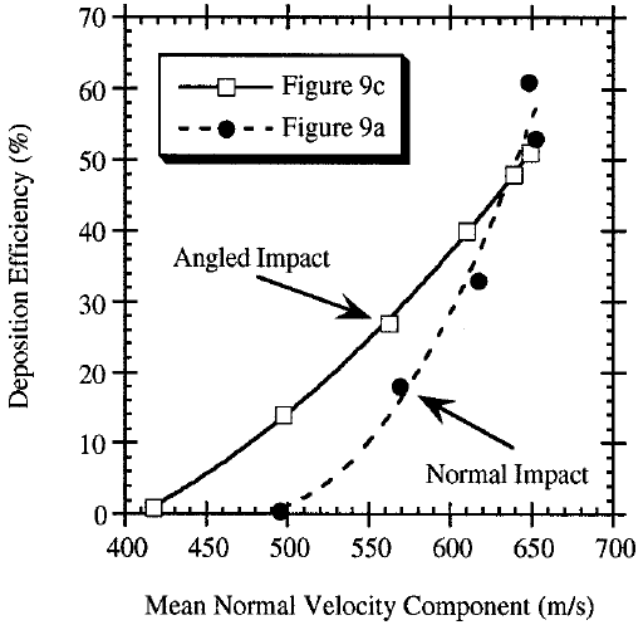

Figure 11. Deposition efficiency versus mean normal velocity [3].

The standoff distance can also play an important role as to where the gas stream starts to mix with the ambient atmosphere around the apparatus. The substrate can play an influential role on moving the particle immediately prior to impact of the particle to the substrate. This effect is dependent on the size of the particle. Figure 12 demonstrates that a particle with a diameter of 1 μm is influenced more drastically by the gas stream in proximity to the substrate surface than the 5 μm and 22 μm particles [3].

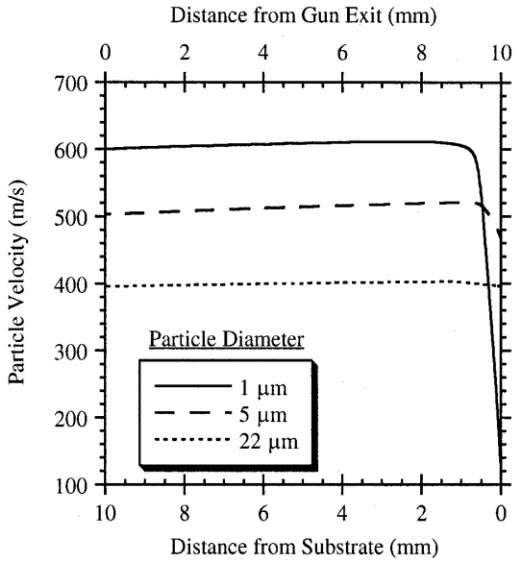

Figure 12. Theoretical calculations of particles deceleration near substrate for 10 mm gun standoff, fully dense Cu powder at 27 ℃ with 2.1 MPa and air as the driving gas [3].

2.2.5 Critical Velocity

The critical velocity required for bonding a particle to either the substrate or another particle can vary greatly. Therefore, the critical velocity is presented as an estimated range that is observed both experimentally and determined theoretically to allow for the most successful deposition. Having a particle velocity below the critical velocity range for deposition can result in a collision event, which could results in no deposition or disruption of the native oxide layer. Exceeding the critical velocity can induce delamination and erosion of the deposited particles or the substrates surface [27, 28]. Figure 13 shows a diagram of the material depositions at different stages with a Cu powder on low carbon steel [7].

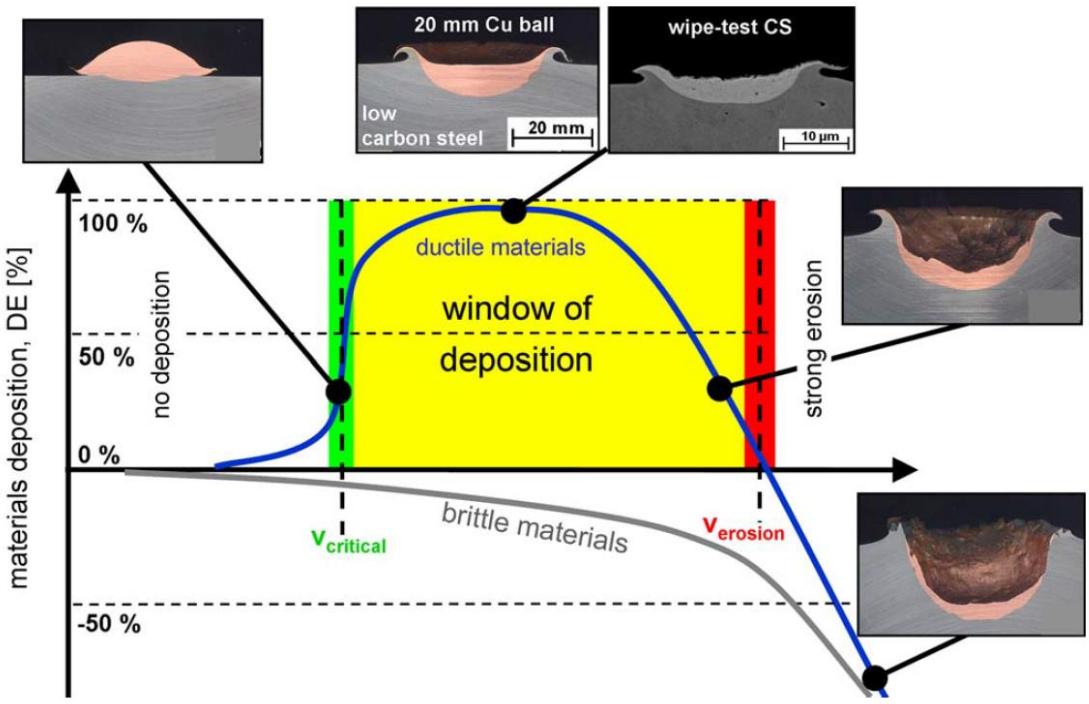

Figure 13. Schematic correlations between particle velocity, deposition efficiency and impact effects for a constant impact temperature [7].

The minimum critical velocities (Table 3) were gathered from articles that focused on 20 µm and 25 µm powders [6-8, 19, 27, 29]. This table presents an approximate starting point for the initial window of deposition. Parameters that can affect critical velocity for deposition are the substrate and substrate temperature shown on page 40.

Table 3. Typical estimated minimum critical velocities for specific materials, values taken from the following literature [6-8, 19, 27, 29].

Materials		V_{crit} estimated minimum for 20&25 μm particles (m/s)
Magnesium	Mg	760
Aluminum	Al	620
Titanium	Ti	700
Tin	Sn	160
Zinc	Zn	360
Zirconium	Zr	510
Iron	Fe	650
Stainless Steel 316L		700
Copper	Cu	460
Nickel	Ni	610
Niobium	Nb	575
Molybdenum	Mo	630
Silver	Ag	350
Lead	Pb	130
Tantalum	Ta	490
Gold	Au	250
Tungsten	W	480

2.3 Typical Microstructural Features of CS deposits

When a particle is sprayed at the substrate and possesses the necessary critical velocity, the particle undergoes an extensive deformation when it impacts the substrate. Deformation induced by the collision event causes the powder particles to plastically deform from spherical to a lenticular, or pancaked, shape (Figure 14). The direct and angled impact of the particle typically exhibits-jetting (extrusion of powder material), around the particle [7, 30].

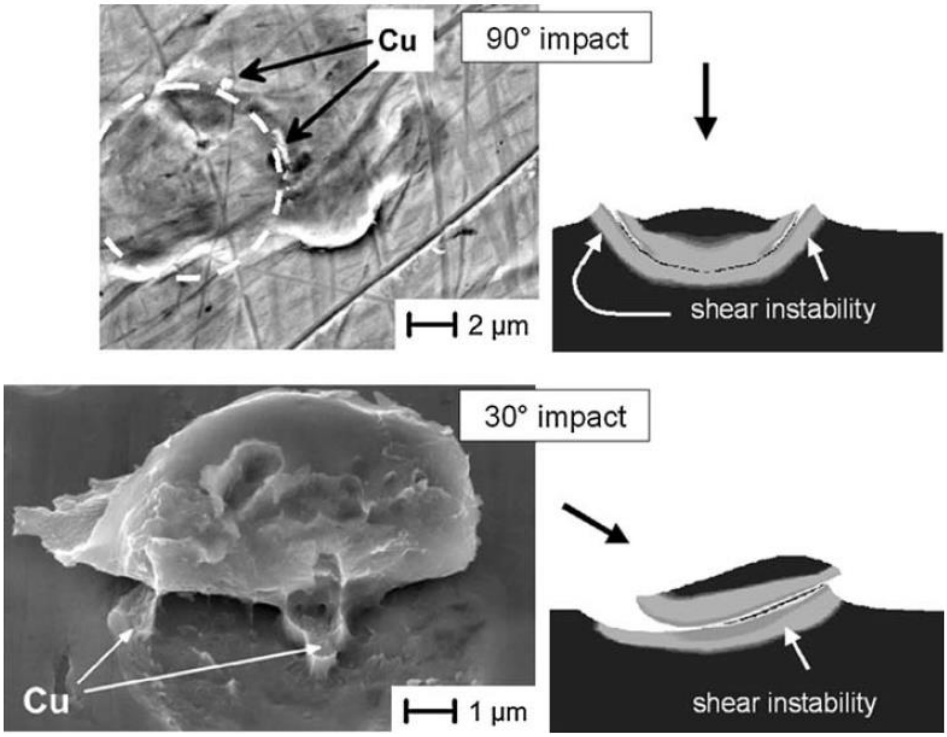

Figure 14. Particle morphology for direct and angled impacts showing shear instability [7].

The grains of the CS microstructure are usually flattened elongated grains perpendicular to the spray direction (Figure 15 and Figure 16) [31]. The process typically results in a high degree of grain refinement, with the resulting grains exhibiting widths on the order of tens of nanometers and a length of hundreds or thousands of nanometers (Figure 17) [32, 33].

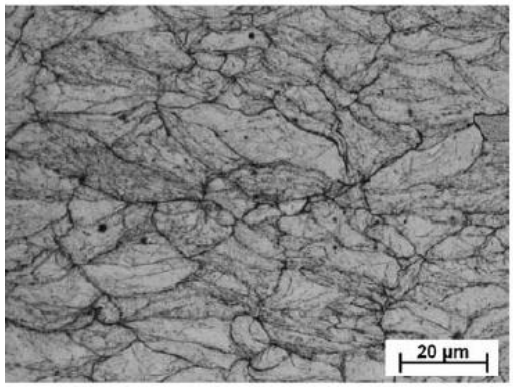

Figure 15. Microstructure image of CS Cu-coatings on Cu-substrate in the as-sprayed state as obtained by OM of etched of etched cross-section processed with nitrogen gas [31].

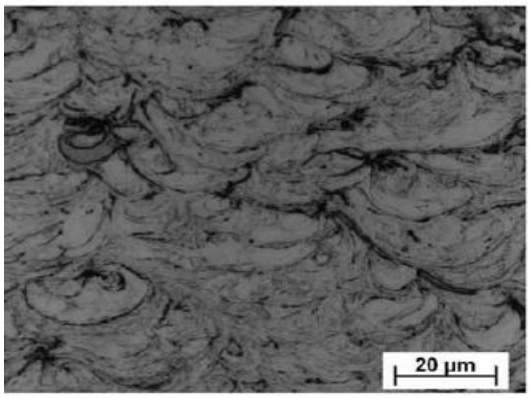

Figure 16. Microstructure image of CS Cu-coatings on Cu-substrate in the as-sprayed state as obtained by OM of etched of etched cross-section processed with helium gas [31].

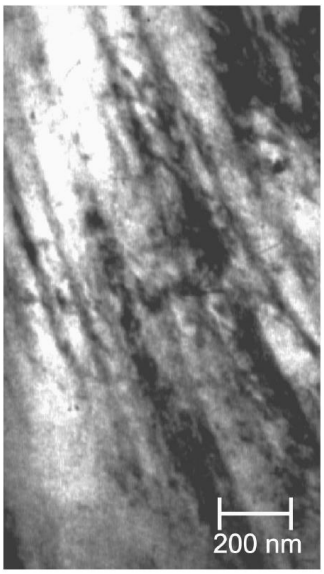

Figure 17. TEM micrograph image of a CS copper coating with elongated grains with a width of some tens of nm and a length of several hundred nm [32].

A comparison of the porosity between the N_2 and He CS microstructures show the He sprayed materials contains a much lower porosity then that of N_2. The lower porosity can be due to the higher velocity achieved by the He gas using the same parameters as the N_2 sprayed material. In Figure 18 and Figure 19 it was discussed by Stoltenhoff et al. that by switching from nitrogen to helium the deposition efficiency only increased by 10 to 20%. Note the black arrow in Figure 18 and Figure 19 indicates the interface between the coating and substrate [31].

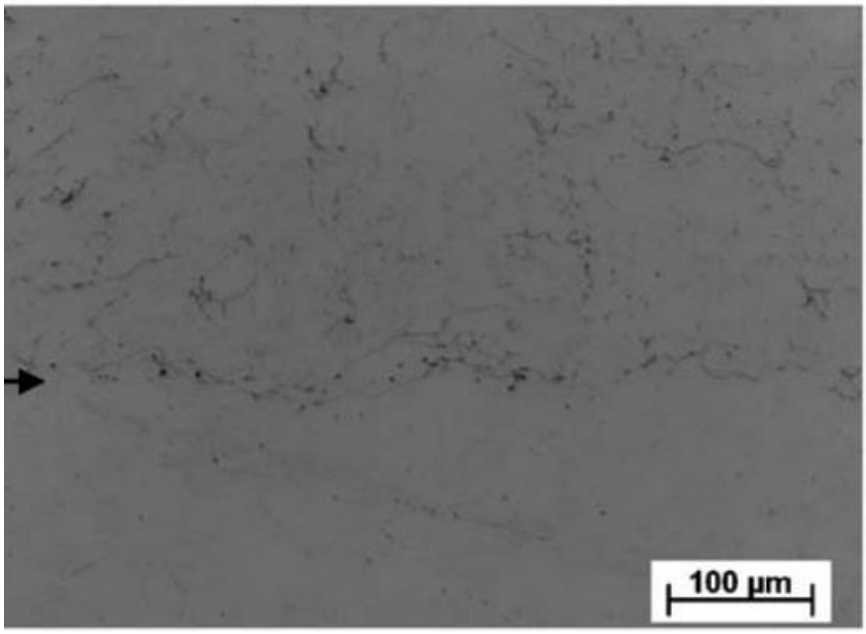

Figure 18. Microstructure image of CS Cu-coating on Cu-substrate (process gas: nitrogen) [31].

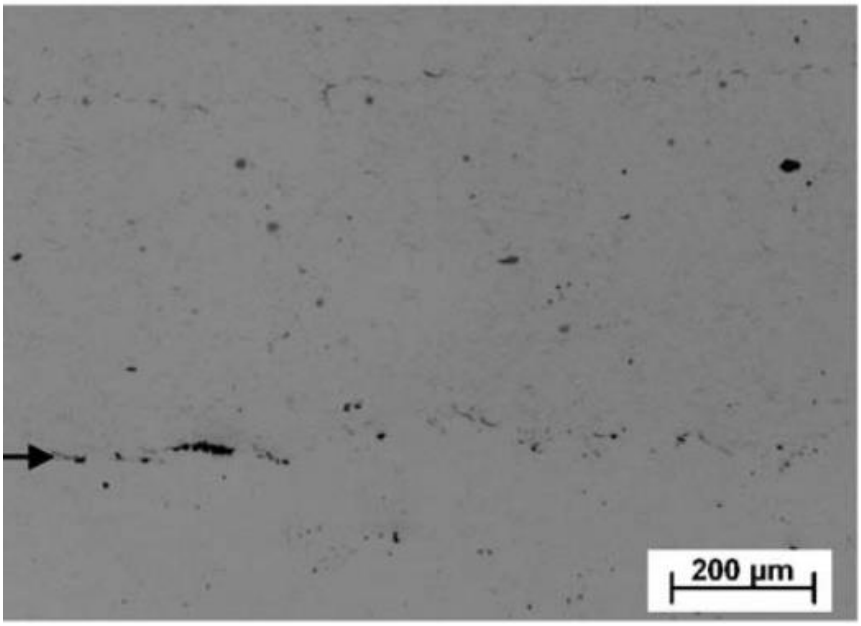

Figure 19. Microstructures image of CS Cu-coatings on Cu-substrate (process gas: helium) [31].

2.4 Inter-particle bonding mechanisms

In order to achieve a successful metallic bond through cold spraying, the particles must travel at a sufficient velocity to break down oxide films on the particle surfaces. As a result of the velocity of impact, the particles undergo plastic deformation. In Figure 20 the particle has impacted the substrate and displays both jetting as well as signs of metallic bonding on a particle-particle interface, caused by adiabatic shear instability [34]. The jetting process is believed to break up the oxide film to allow for metallurgical bonding [35]. The particles will also undergo severe tamping due to the building up of particles causing more plastic deformation, regardless of if the particles are bonded or not [36, 37].

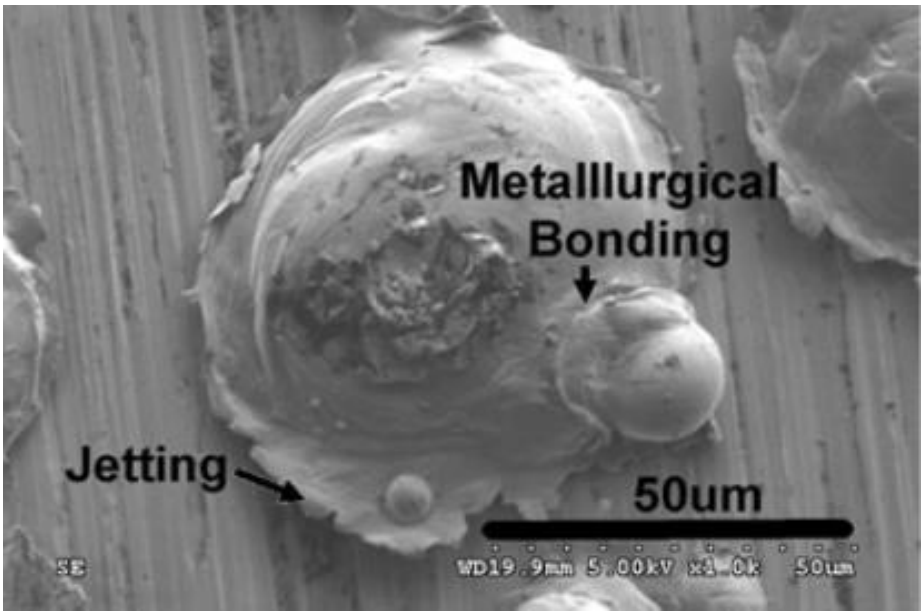

Figure 20. SEM micrograph image of CP Ti splats deposited at 750˚C, and 3 MPa (770 m/s) [34].

Different mechanisms of mechanical bonding can be achieved through multi-particle interactions such as interlocking and extrusion. The interlocking and extrusion effects are shown in Figure 21 and Figure 22 [37]. The mechanical interlocking depends on the topography of the impacting surface, including the penetration depth of impacting particles and if an overlap of particles occurs.

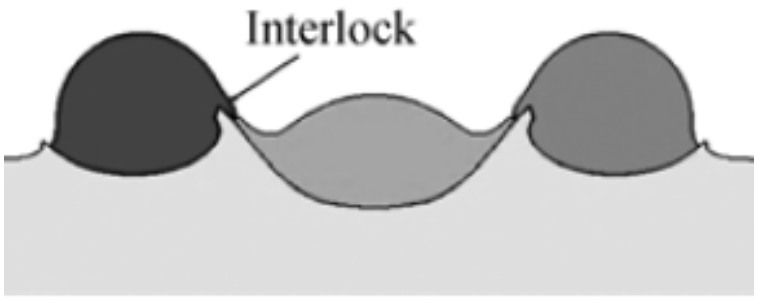

Figure 21. Multi-particle interaction for an impacting velocity of 600 m/s: interlocking effect [37].

Figure 22. Multi-particle interaction for an impacting velocity of 600 m/s: extrusion effect [37].

The high impact velocity reached during deposition in the CS process causes large amounts of plastic deformation and strain hardening, through plastic shock wave to the adjacent particles and substrate. The plastic shock wave is the rapid rise of pressure, which can possibly help lead to the continually enhanced bonding of the particles to substrate and other particles. [16]. The degree of deformation can be compared to the high collision pressure that is exerted in explosive welding [38].

2.5 The effect of Heat Treating Cold Sprayed Material

Heat treating a CS material after spraying can be extremely beneficial if the cold worked microstructure post deposition undergoes the process of recovery, recrystallization and/or grain growth, while experiencing sintering of the remaining unbonded particle surfaces. The as-sprayed samples are cold worked to such a high degree that all the physical and mechanical properties are greatly altered from their typical values. It should be noted that for this study, the term “annealing” is used in the sense of the classical metallurgical definition of annealing, and not a specific temper designation for the 6061 alloy.

In the recovery stage of annealing, the physical and microstructural properties that suffered changes because of cold working begin to recover their original values. While movement and annihilation of dislocations are faster with the higher amount of deformation within a region, increasing temperature can also speed up the recovery time. The movement of the edge dislocations can form low-angle grain boundaries or subboundaries within deformed material [39].

The recrystallization process in CS is dependent on the amount of cold work the regions have undergone. The higher the cold work within a region the lower the activation energy needed. During recrystallization the hardness starts to decrease, and the realignment of the crystal starts to occur, until new grains are formed [39]. Recrystallization has been observed in the CS microstructure from the high deformation caused by the CS process [40]. There are two types of recrystallization that can be found in CS, dynamic and static recrystallization. Dynamic recrystallization is when nucleation of new crystals occurs during deformation, where static recrystallization is produced from nucleation and growth of new grains from heat treatment, in the absence of ongoing deformation. Dynamic recrystallization has been observed in CS deposits

that have no undergone any additional heat treatment. Two possible mechanisms can be found to create dynamically recrystallized grains, these are grain boundary migrations and crystalline rotational [40]. The mechanism of migration based dynamic recrystallization is characterized by the movement of pre-existing high angle grain boundaries creating strain free region in the grain. Dynamic recrystallization through crystal rotation is defined as a gradual increase in misorientation of a dynamically recovered dislocation sub-cell microstructure [41].

Similar dynamic recrystallization phenomena have been observed in other processing techniques such as equal channel angular pressing (ECAP), in which ultra-fine grains (UFG) were observed after processing. These grains were approximately 60 to 100 nm in diameter when subgrains were considered. The ECAP process of Cu also showed that twins were present, showing evidence that recrystallization was occurring much like what is theorized in the high deformation regions in CS [44].

The grain growth process after recrystallization is driven by the reduction in grain boundary area throughout the material, by decreasing the number of grains, resulting in fewer grains of larger diameter. It is possible that grain growth can use excessive dislocation energy that has deformed a grain after recrystallization for boundary migration[39]. A study by Hosseini et al. on the structural evolution and grain growth kinetics for Al 6061 mechanically milled commercial chips were investigated. In the study a temperature of 200°C showed minimal grain growth (14 nm) over a 3-hour period. Factors affecting the grain growth include the activation energy needed for grain growth and the solute drag of Mg_2Si [42].

High deformation regions in CS materials indicate that those materials have undergone recrystallization stage prior to any post-spray heat treatment, while low and medium deformation

regions have yet to exhibit recovery prior to heat treatment [43]. Typically, post spray heat treatments produce the added benefit of improving the strength of the interfaces between the deposited powder particles tend to create greater interfacial adhesion through sintering and diffusion bonding [44].

The mechanical properties of the heat-treated CS materials typically increase in bond strength, increase in conductivity, decrease in hardness, increase in elongation to failure, decrease in yield strength, and decrease in ultimate strength. All these phenomena are consistent with typical annealing behavior of heavily cold worked materials that undergo subsequent heat treatment. Mechanical behavior of CS materials has been widely investigated, and the effects of subsequent heat treatment on those properties are reported in the literature. While they are not the focus of this study, they offer valuable insight into the structure-processing-property-relationships of these materials. The reader is directed to the following papers for more information on these types of studies [13, 26, 31, 36, 43, 45-49].

2.6 SEM and EBSD of CS Microstructures

Given the scale of features of concern in CS materials (ranging from tens of nanometers to microns), the Scanning electron Microscope is the gold standard for microstructural characterization. Figure 23 presents an SEM image of a coating produced by CS from as-atomized 2618 Al powder [10]. This coating shows the different deformation regions created from the impact of the powder in the CS process. These regions can be seen as low deformation regions showing equiaxed grains, medium deformation regions showing elongate grains, and high deformation regions with ultra-fine grains. The use of a Scanning Electron Microscope equipped with a Field Emission Gun (FEG-SEM) is also required for the high deformation

regions of CS. Tungsten thermionic emission sources produce large spot size compared to FEG sources and are not capable of nm scale resolution [50].

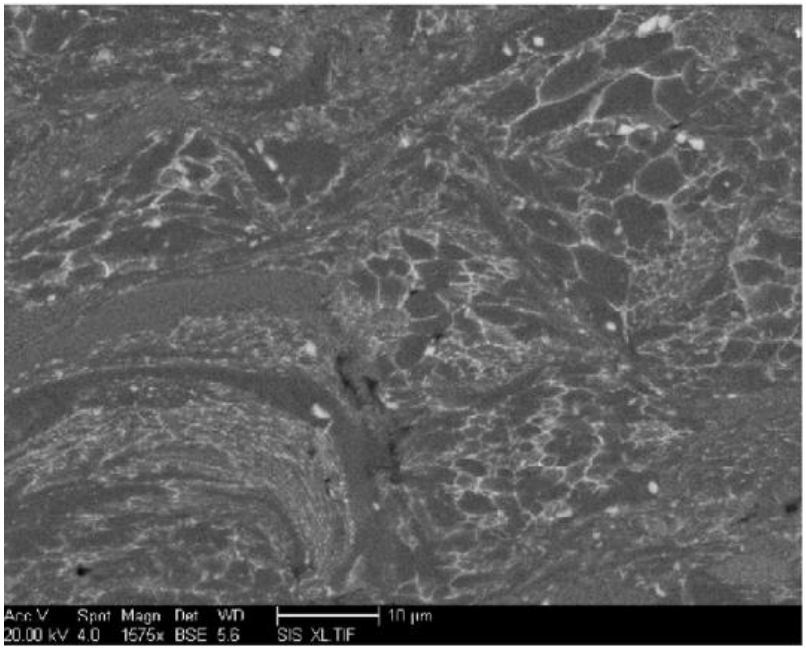

Figure 23. SEM backscatter image of coating produced by CS from as-atomized 2618 Al powder with low (equiaxed grains), medium (elongated grains), and high deformation regions (ultra-fine grains) [10].

Electron backscatter diffraction (EBSD) is a technique that produces an electron backscatter pattern (EBSP) in order to determine the crystallographic orientation of individual grains in a polycrystalline material. This characterization technique allows for understanding the grain orientation, local deformation structure, grain size, grain shape, and phase(s) present in the material. For an EBSD measurement a flat/polished crystalline specimen is placed in the SEM chamber at an angle of 70° with the sample facing the diffraction camera [51]. Finally, as the incident beam hits the sample surface the electron backscatter diffraction is produced and hits the phosphor screen and causes an EBSP or Kikuchi lines on the phosphor screen. The EBSP is then read by the detector and processed to recognize the individual patterns for indexing.

EBSD over the past decade has focused on finer grain sizes for severe plastic deformation (SPD) processes. These processes include CS [40, 52-55], equal channel angular pressing (ECAP) [56], Friction stir processing (FSP) [57], and more. The grain size from SPD processes can be on the order of 0.1-1 μm, which are referred to as ultra-fine grains and for grains with diameters less than or equal to 0.1 μm, the term nanostructured or nanocrystalline grains is standard convention [58].

The EBSP is produced by a backscatter diffraction of a stationary beam of high-energy electrons within approximately a depth of 50 nm. Parameters of EBSD include working distance between column and sample, working distance between EBSD camera and sample Figure 24. voltage, beam intensity, EBSD CCD camera binning mode, gain, exposure time, band detection mode, Hough resolution, step size, scan area, tilt correction. Parameters that can change the spatial resolution include the sample working distance, voltage, and beam intensity [59]. Note that the higher beam intensity and longer acquisition time to collect the data will result in more contamination of hydrocarbons within the chamber which can result in image drift making it difficult to take high resolution EBSD images [60, 61]. Other common errors in EBSD include instrument calibration, specimen tilt axis, and sample alignment [62].

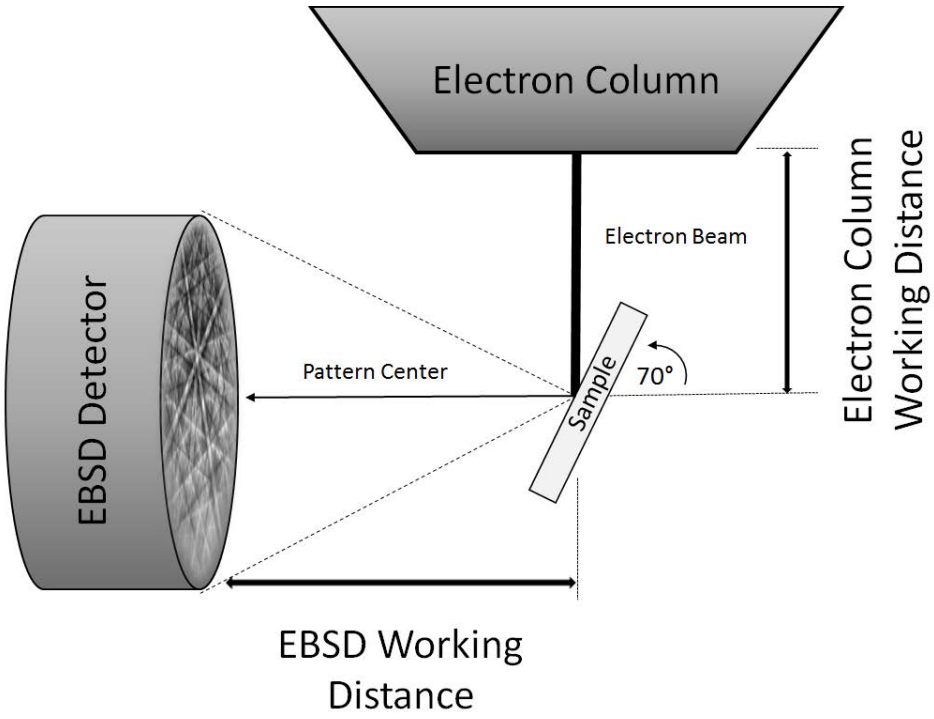

Figure 24. Schematic representing the sample and detector geometry used in EBSD analysis in the SEM.

CS microstructure exhibits ultra-fine grains that have been observed to be as small as 100-200 nm in diameter [40]. The CS microstructure is nonhomogeneous shown by the deformation shown in Figure 25. The formation of these ultra-fine grains is associated with dynamic recrystallization, resulting from enough deformation from the process to reduce the recrystallization temperature to that of the gas stream [40].

Analytical methods enabled by EBSD include grain size determination, grain orientation analysis, relative phase distribution by area, and strain analysis. The grain boundary threshold for grain size analysis by EBSD is typically below 15° of mis-orientation for low-angle grain boundaries and above 15° of mis-orientation for high-angle grain boundaries [56, 63]. The grain orientation analysis can be plotted with respect to the material by comparing the grain orientation

to the pole figure or inverse pole figure [64]. The methods used for looking at grain boundaries and grain orientation have been used for CS and ECAP for ultra-fine grains shown in the following literature [40, 45, 63, 65].

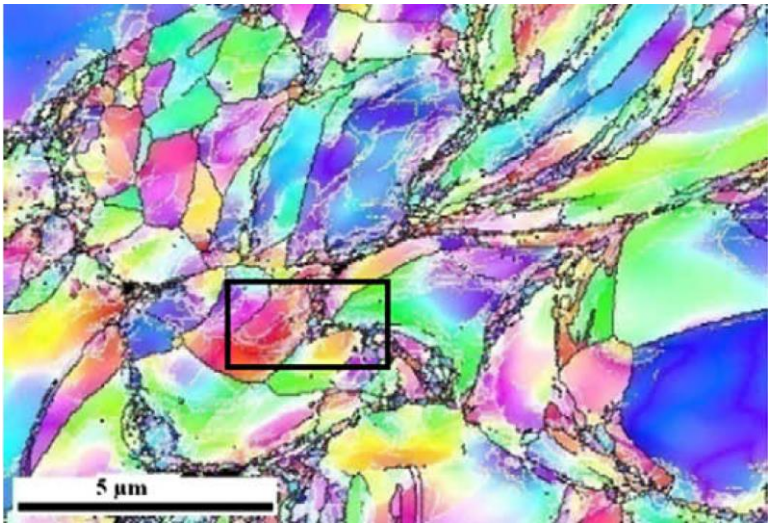

Figure 25. EBSD characterization of the cross-section of as-sprayed coating, Euler angle Map. The black box is to represent another figure within the literature [40].

.

2.7 Microhardness data

Microhardness is often used to characterize the inhomogeneous mechanical properties of cold sprayed deposits and the substrates upon which they are sprayed. Microhardness of the deposit and substrate can be influenced by the surface roughness of the substrate before deposition. In a study the surface microhardness of a CS Cu material was the lowest when deposited on the ground surface (105.9 kgf/mm^2), and highest when grit-blasted (179.1 kgf/mm^2) [35]. Typically as the distance of the CS surface is closer to the substrate the values will become closer to that of the bulk 1100 Al (Figure 26) [66]. The different sized powder particles can also influence the microhardness [67]. The microhardness of the CS material is typically higher than that of the bulk material [14, 19, 31, 34, 46, 68-70]. The effect of the grain boundaries on the

microhardness properties can be seen using the Hall-Petch relationship where the smaller the grain size the greater the hardness. The microhardness may also vary with the crystal orientation [39].

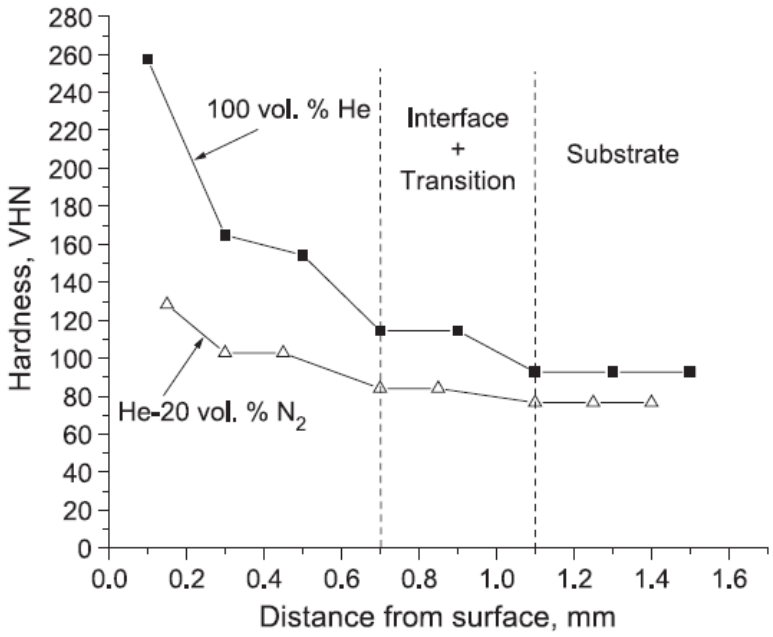

Figure 26. Mechanical properties of 1100 Al coatings in terms of hardness VHN [66].

In a study conducted by Eason et al. Vickers microhardness profiles were taken across the substrate through the interface of the CS bulk copper. These microhardness values were compared to post annealing and after annealing at 400C for 1 hr. These two different states of the copper showed that before annealing the hardness was higher the closer to the interface and decreased with increasing distance. When annealed the sample hardness decreased compared to the post annealed hardness. These microhardness results can be seen in Figure 27 [71]. Another study by Eason et al. showed that for Cu the CS microhardness was harder than cold rolled (90% reduction) after annealing, and the hardness was less before annealing than the cold rolled (90% reduction) Cu. Figure 28 shows a microhardness indent encompassing multiple CS regions [72].

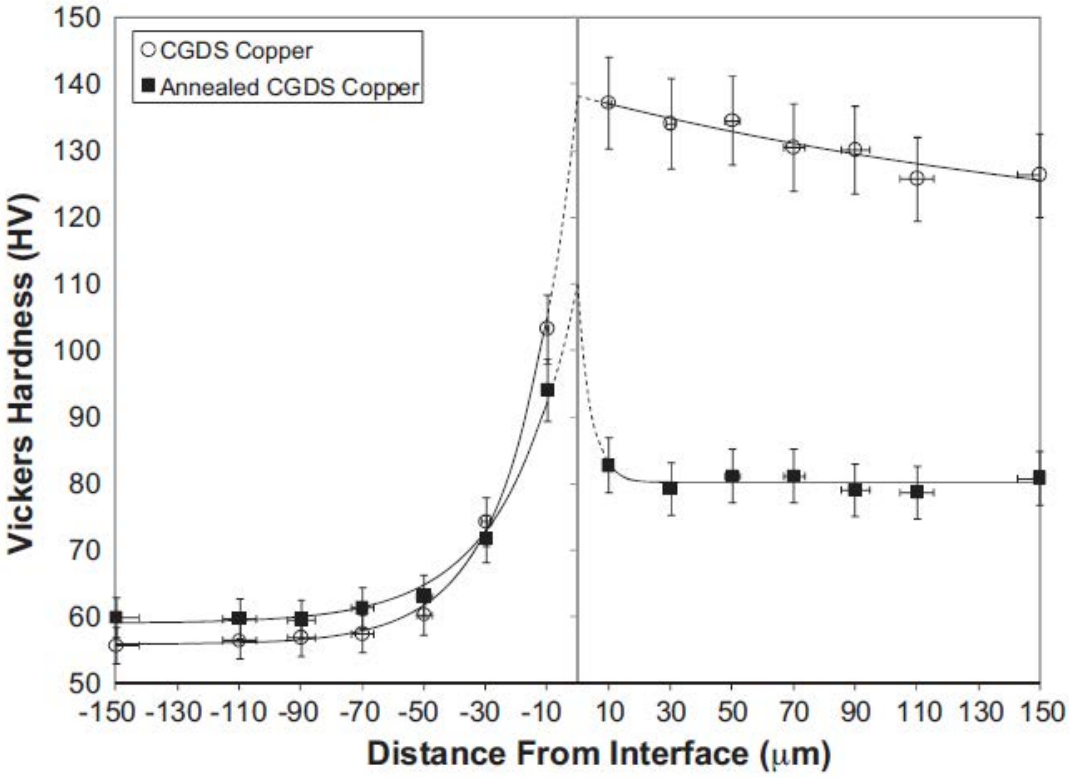

Figure 27. Vickers microhardness profiles taken across the substrate (left), interface (μm = 0), and spray (right) of bulk copper sprayed on powder metallurgy copper [71].

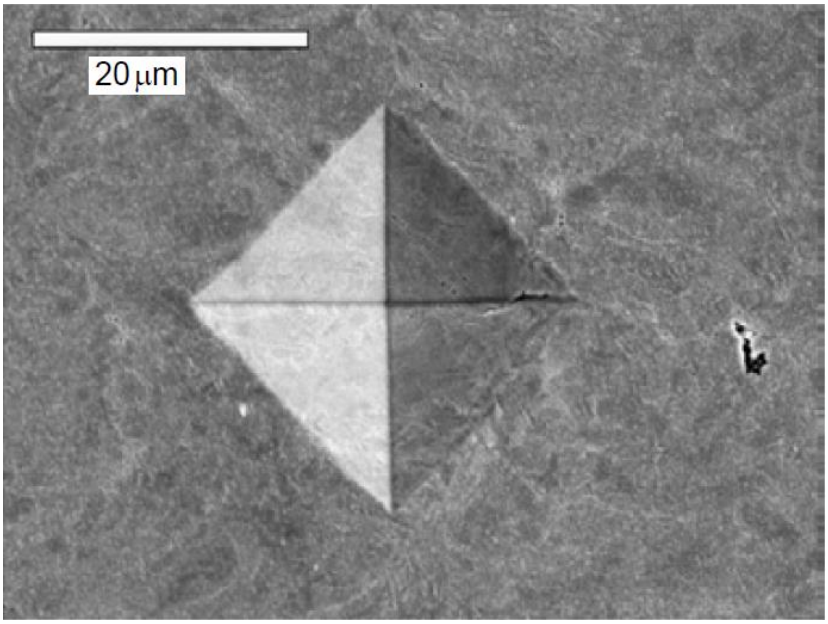

Figure 28. SEM image of a microhardness indent on a CS Cu as-sprayed sample encompassing multiple regions [72].

Chapter 3: Experimental Procedure

The following chapter provides an overview of the Cold Spray methodology for sample production and experiments performed. The experiment was designed in order to further understand the microstructure of the 6061 Al CS, and its response to heat treatment. Five samples were analyzed. One cross sectioned powder and 4 different annealing state samples cut from the same CS bulk sample. In order to analyze these samples, they had to be polished for EBSD analysis with correlating SEM SE and BSE mode images. After EBSD, microhardness testing was completed to determine if there was a difference in microhardness between different regions.

3.1 Cold Spray Parameters for Deposition

For this current project, a total of 5 specimen conditions were analyzed (CS-220 powder, AR, 1 hr, 10 hr, and 100 hr). With the exception of the unsprayed powder, all specimens were sectioned from a single deposit of sprayed material, and therefore all CS samples share the same CS process parameters. The spray parameters that were used for the CS sample are listed in Table 4, and constant operating parameters in Table 5. The substrate was prepared by grit blasting before CS deposition. The CS as-received sample and powder were provided by the Army Research Lab.

Table 4. Aluminum Cold Spray Sample Parameters Variables.

Sample Number	Powder Composition	Powder Source and Condition	N2 Pressure (bar)	N2 Flow (m3/hr)	Feeder RPM	Traverse Intervals or (# of cycles)
CS-220	6061	Brodmann HT100c to dry overnight	25	181	2	12

Table 5. Cold Spray Gun Parameters Constants.

Carrier Gas	Powder Feeder	Gun Speed (mm/s)	Step size (mm)	Prechamber	Nozzle	Carrier Gas	Standoff Distance (in)	Gun Heater Setpoint (°C)
N2	CGT 120 hole	200	2 mm during pass 4 passes staggered .5mm each per cycle	Long	PBI Type 33, CS1104	N2	1	400

3.2 Sample preparation

To investigate the annealing response of the cold spray microstructure four sections were cut out of the CS-220 billet from the as-received state. These samples were cut from the same billet to remove any variation in samples. Three specimens were heat treated at 200 °C for an increasing time period (Table 6). 200 °C was chosen as the temperature to study whether there was recovery, recrystallization, and grain growth within each region, and to investigate the annealing response. The three samples were isothermally heat treated within a tube furnace in air. The three samples were heat treated at 200 °C and removed at each interval 1 hour, 10 hours, and 100 hours in order to investigate the interrupted annealing response of the sample.

Table 6. Sample altered states after received from Army Research Lab.

Sample Name	Temperature	Time	Atmosphere
220 Powder	N/A	N/A	N/A
220 AR	N/A	N/A	N/A
220 HT1	200 °C	1 hour	Air
220 HT10	200 °C	10 hours	Air
220 HT100	200 °C	100 hours	Air

For microstructural analysis, samples were epoxy mounted and set in a vacuum to remove air bubbles and left to cure overnight. Grinding and polishing were completed with the MetPrep3 with power head. The samples were prepared by traditional metallographic techniques down to 0.04 μm colloidal silica suspension polishing media.

After polishing, the CS samples were extracted from sample mounts and any remaining epoxy mounting material was removed from all surfaces. The step of removing the mounting material was performed to eliminate the effects of excess hydrocarbon contamination in the SEM chamber, which can be detrimental to long duration EBSD scans. The powder mounted sample was carbon coated using the Ted Pella 108C Auto/SE Carbon Coater to create a conductive path for imaging.

3.3 Scanning Electron Microscope and Electron Backscattering Diffraction

The SEM that was used for this study was the Tescan Mira3 field emission SEM equipped with Nordlys Nano EBSD with Aztec software. The field emission SEM was used for its higher resolution capabilities than a tungsten source SEM. The SE and BSE mode images were taken at an accelerating voltage of 15kv with a spot size of 5.8 nm, and a working distance

of 15 mm for high resolution images. The SE and BSE mode images were used to examine the microstructure and the contrast difference between the grains.

The initial set up and physical parameters for the EBSD program and camera include phase aluminum, crystal structure FCC, lattice parameter 4.05Å, 84 reflectors (the number of reflectors tells the Oxford software how many theoretical kikuchi bands to use during the indexing process), and camera insert distance: 221.6 mm. The EBSD camera settings include binning mode of 4x4 and high gain. The SEM parameters for EBSD analysis and images were taken at an accelerating voltage of 12 kV, a spot size of 9.5 nm, and a working distance 20 mm for low and medium deformation regions and 5.1 nm and a working distance of 15 mm was used for high deformation regions to achieve a spot size of less than 10 nm. This data was collected to look at the grain size and orientation. Other parameters for EBSD for window size, step size, and time per sample can be found in Table 7. Step sizes were chosen based on the predicted grain size and time for acquisition.

Table 7. EBSD parameters for window size, step size, and time per sample.

Sample	Window size (um)	Step size (nm)	Time (hr:min:sec)
220 AR – low	10 µm x 10 µm	50 nm	2:01:53
220 AR – medium	10 µm x 10 µm	50 nm	2:01:53
220 AR – high	1 µm x 2 µm	10 nm	1:08:55
220 HT1 – low	10 µm x 10 µm	50 nm	2:01:53
220 HT1 – medium	10 µm x 10 µm	50 nm	2:01:53
220 HT1 – high	1 µm x 2 µm	10 nm	51:10
220 HT10– low	10 µm x 10 µm	50 nm	2:01:53
220 HT10 – medium	10 µm x 10 µm	50 nm	2:01:53
220 HT10 – high	1 µm x 1 µm	10 nm	57:21
220 HT100 – low	10 µm x 10 µm	50 nm	2:01:53
220 HT100 – medium	10 µm x 10 µm	50 nm	2:01:53
220 HT100 – high	1 µm x 1 µm	10 nm	55:25

3.4 Post Processing

Post processing is needed to have smooth data to work with and gather more meaningful conclusions. The post processing is completed to have a continuous pixelated image of results, and to distinguish between the different grains. Once the EBSD data was collected in Aztec, it is was exported into Channel 5 for cleaning and extrapolation of the data. First, cleaning out wild spikes (an isolated mis-indexed pixel) in the data was performed, and then extrapolation was performed. Extrapolation was completed while comparing the SE image mode to the EBSD image mode to ensure proper fit to the observed grain boundaries.

The extrapolation works by taking the nearest neighboring pixels and assigning the zero solution (blank) pixels with a cycle of 10 iterations of the nearest neighboring pixels. Note: that the extrapolation should be used with caution for large regions of zero solution that could consist of unknown contamination or phases. Figure 29 and Figure 30 demonstrate the extrapolation of data before (no cleaning or extrapolation, showing green dots zero solution pixels) and after (complete extrapolation). In the Channel 5 software the misorientation angle between pixels is used to determine grain boundaries. High angle grain boundaries were analyzed from greater than 15° and low angle grain boundaries were analyzed above 2.5° to below 15°. Grain boundary data was analyzed from 2.5° and up. Band Contrast is also used for the image quality of the captured EBSD image, showing the average intensity of the Kikuchi bands.

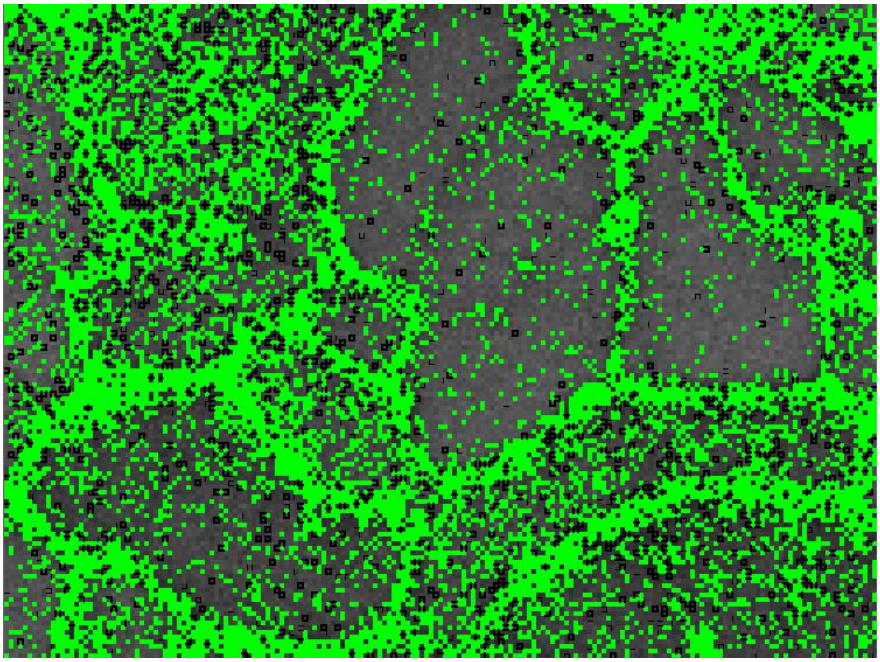

Figure 29. Image of EBSD map of powder used for CS to show an example of before cleaning and extrapolating data (grey pixels are indexed pixels and green pixels are zero solution or non-indexed pixels).

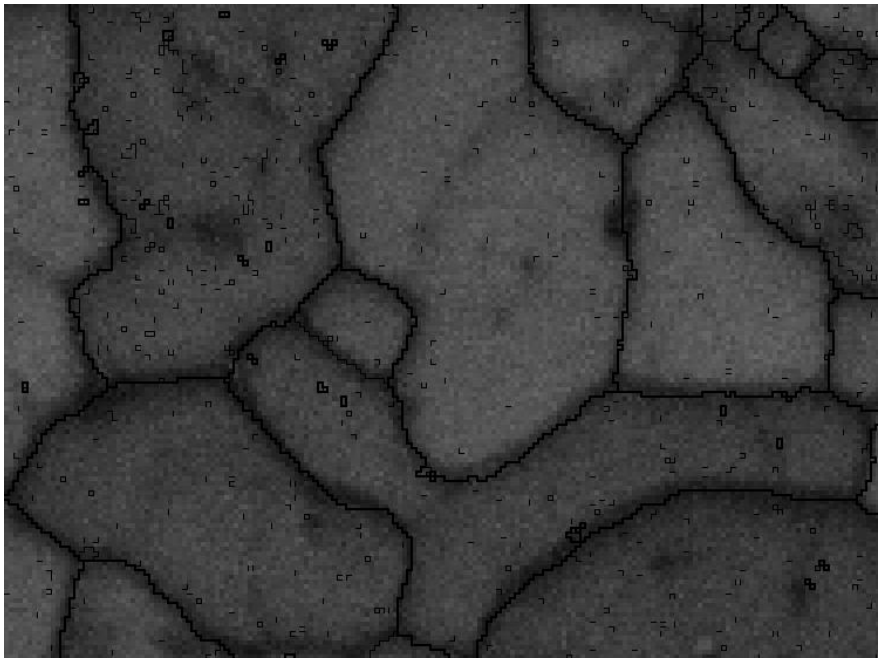

Figure 30. Image of EBSD data of powder for CS to show an example after cleaning and extrapolating data (black lines are grain boundaries outlining the individual grains).

3.5 Microhardness testing

Microhardness testing was performed with a Shimadzu HMV-G21 series microhardness tester. Arrays of 25 indents shown in Figure 31 were performed on the as-received and heat-treated specimens. Indents were taken using a 9.807×10^{-2} N force and 10 second dwell time. BSE mode images were then taken of indents from the low, medium, and high hardness values for correlation to microstructural features. Microhardness testing was performed to assess the dependence of microhardness on the microstructure under the indent, and to determine the change in properties within regions of differing degrees of deformation, due to the various exposure times at an elevated temperature.

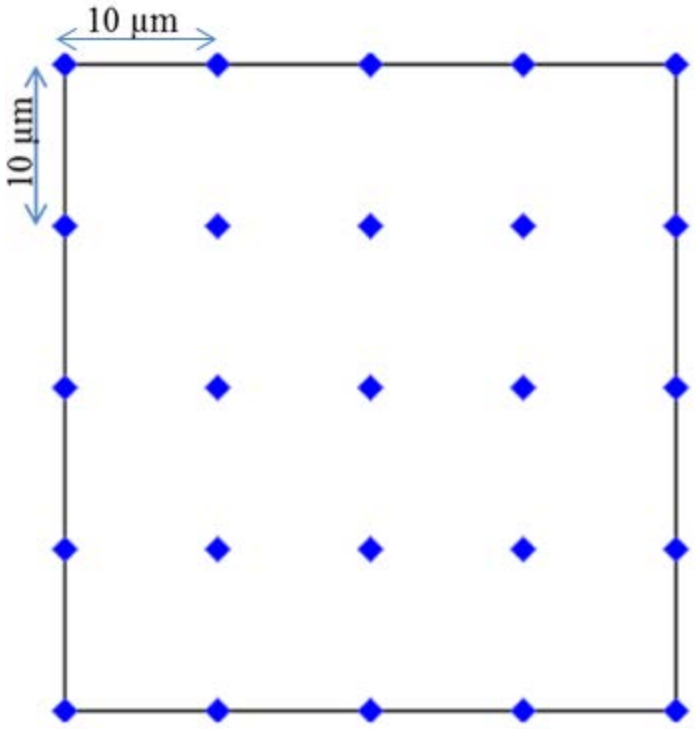

Figure 31. Schematic of microhardness indents.

Chapter 4: Results and Discussion

This chapter presents the results from the experiments laid out in the previous chapter, and provides a discussion on microstructural response to prolonged exposure to elevated temperatures. Detailed SEM and EBSD images illustrate grain size and orientation before and after annealing of all samples. The presentation of data begins with the imaging and EBSD results from unsprayed powder specimens, to provide context on the undeformed microstructural features prior to spraying. Relatively low magnification images of microstructures are presented from each of the samples (AR, 1 hr, 10 hr, and 100 hr) to highlight the difference in appearance of the different characteristic deformation regions (low, medium, and high). The sections that follow present a progressive evolution of the characteristic regions with respect to grain sizes and orientation, for successively longer exposure to elevated temperature. Finally, hardness data is presented from each sample and then compared by region in the context of the overall microstructural effects of annealing.

4.1 Characterization of Pre-Sprayed Powder

Three randomly selected powders were analyzed for grain size and orientation. The microstructure and morphology of the pre-sprayed 6061 powder is presented in Figure 32. These SE mode images show that the powder is roughly spherical and has a Si rich secondary phase present in the as-solidified structure. The powders ranged from 20 μm to 50 μm in diameter. Three randomly selected powder sites were analyzed in order to have a better understanding of the grains and to show that each powder had randomly oriented grains.

The orientation can be seen within the inverse pole figure maps and pole figure maps from the three different powder particles, showing that the grains are randomly oriented with

respect to one another. This data shows that there is no texture to the original powder. The average grain diameter range of the powder is approximately 2 to 5 μm in diameter. The grain orientation was expected to be randomly distributed showing that the powder had heterogeneous nucleation sites. The grain size data from the powders will be used to correlate between grains observed in the low, medium, and high deformation regions of the cold sprayed microstructures. The orientation data of the powder can be used to compare the orientations of the low, medium, and high deformation regions and the orientation that is present in each region. Additional EBSD maps can be found in appendix A.

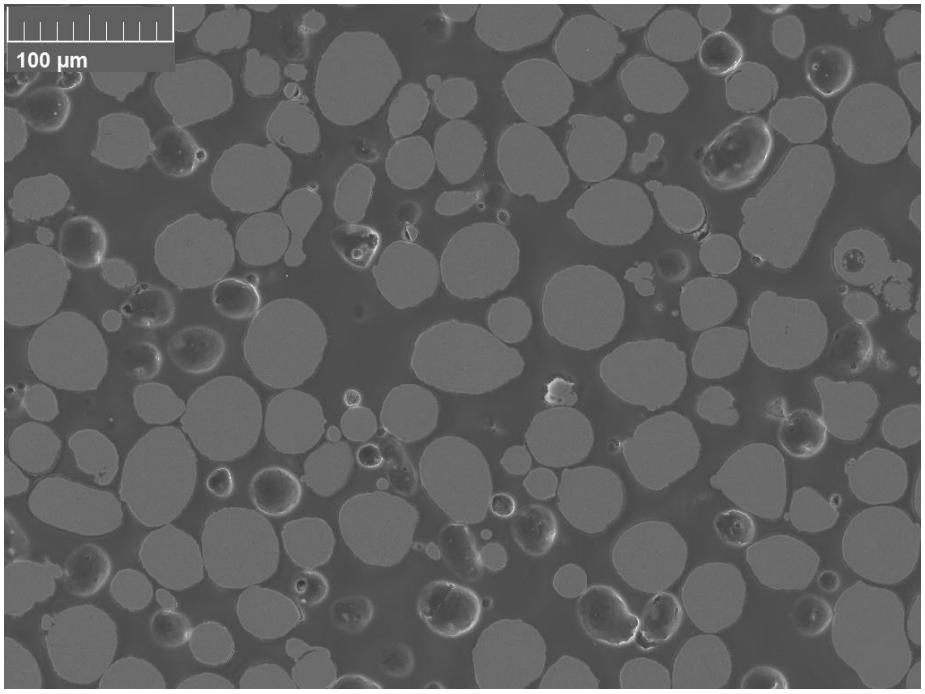

(a)

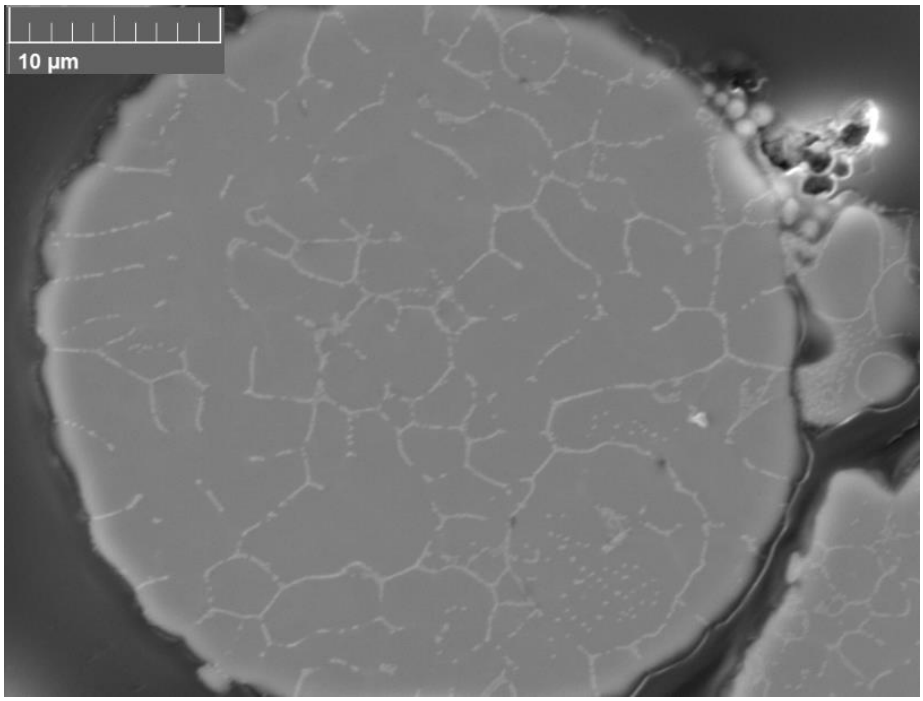

(b)

Figure 32. SEM micrographs taken in SE mode of powder particle(s) mounted in epoxy and polished in cross section. Samples were coated with carbon to achieve conductivity for imaging.

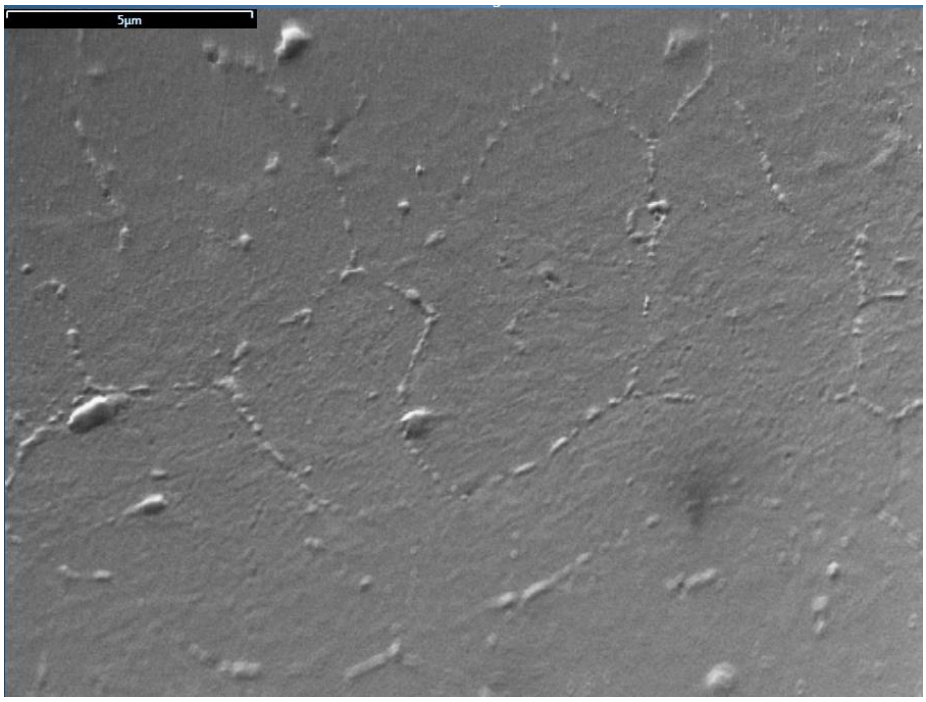

Figure 33. SEM micrograph taken in SE mode of powder site 1. Note a 5 um scale bar is presented in the image.

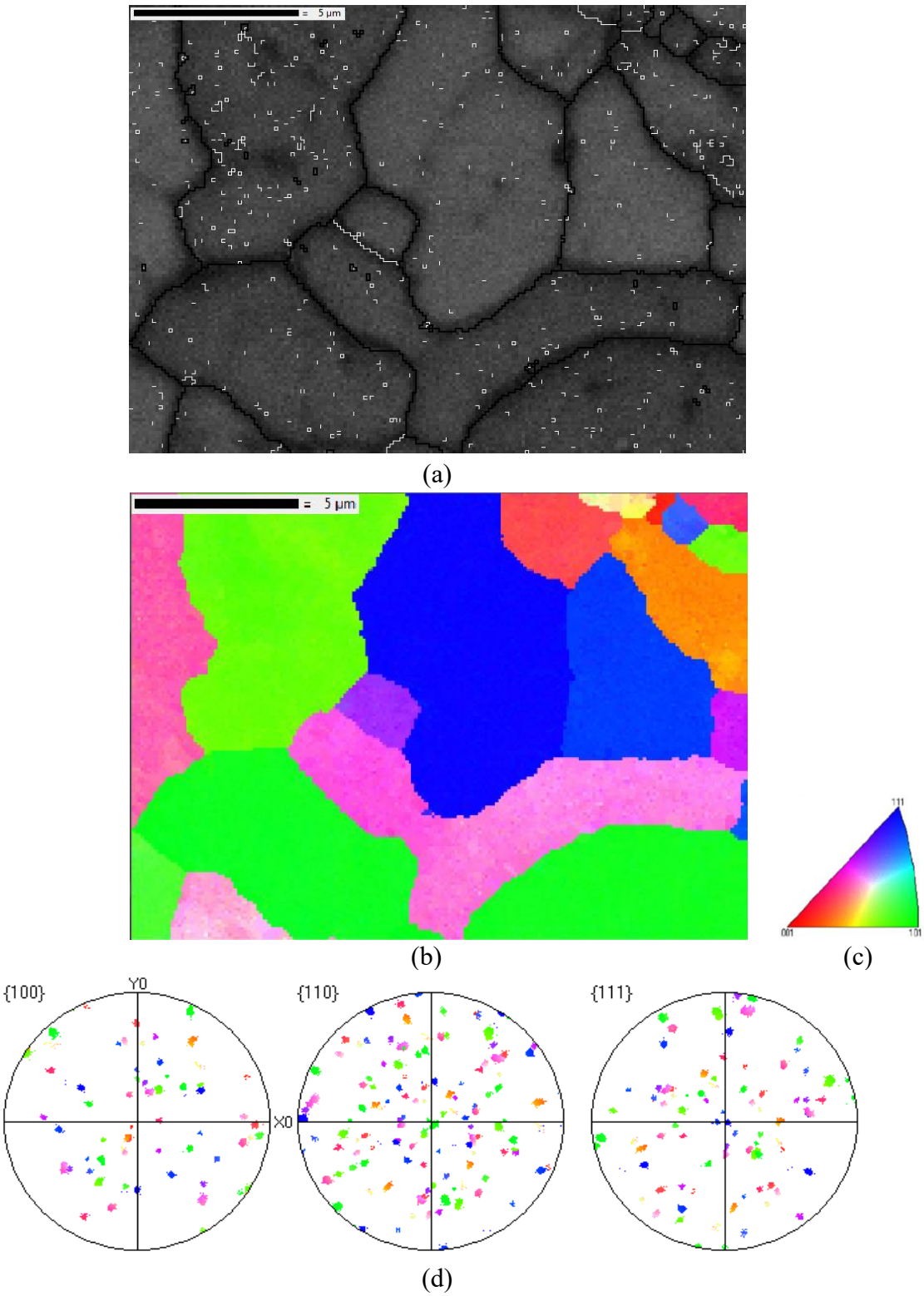

Figure 34. EBSD band contrast image (a) showing grain boundaries from powder cross section site 1 LAGB (<2.5°) white lines and HAGBs (<15°) black lines. Orthogonal IPF map Z (b) for a randomly selected powder cross section site 1. IPF legend (c). Note: 5 µm scale bar is presented in each image. Pole figure map (d) of {100}, {110}, and {111} for site 1.

4.2 CS Microstructure and Characteristic Deformation Regions

The overall microstructural images, taken at low magnification, are presented for AR (Figure 35), 1 hr (Figure 36), 10 hr (Figure 37), and 100 hr (Figure 38). In these figures three characteristic regions can be observed; 1) low deformation, 2) medium deformation, 3) high deformation. These regions were chosen as low, medium, and high deformation because of the resulting degree of deformation to the grains from the impact of the particle. The center of the powder results in the lowest amount of deformation and would keep a similar structure as the original powder. The middle of the powder being between the edge and center of the particle, results in higher deformation than low deformation region. The high deformation is on the edge of the particle resulting in the largest deformation force from the particle impact. These regions are observed in all the samples, and persist without obvious change, despite long exposure to elevated temperature. This suggests that annealing does not drastically alter microstructural features at this scale. However, characterization at higher magnification suggests otherwise.

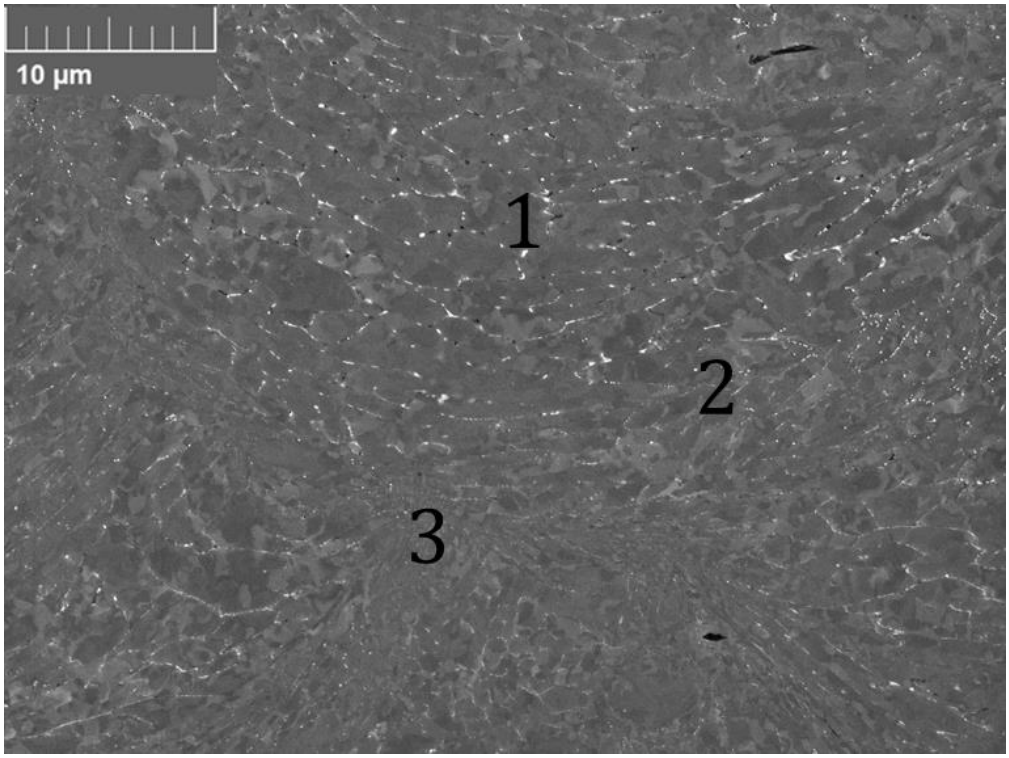

Figure 35. SEM micrograph taken in SE mode of AR sample showing the overall microstructure of a Cold Spray surface 1) low deformation region, 2) medium deformation region, and 3) high deformation region.

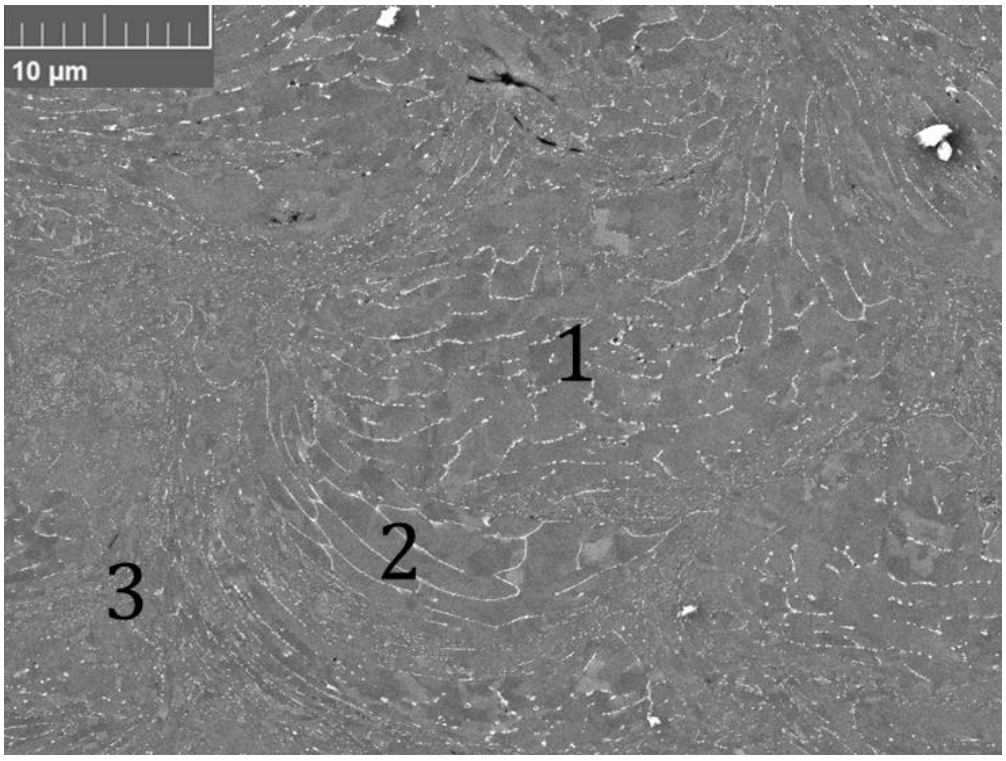

Figure 36. SEM micrograph taken in SE mode of 1 hr sample showing the overall microstructure of a Cold Spray surface 1) low deformation region, 2) medium deformation region, and 3) high deformation region.

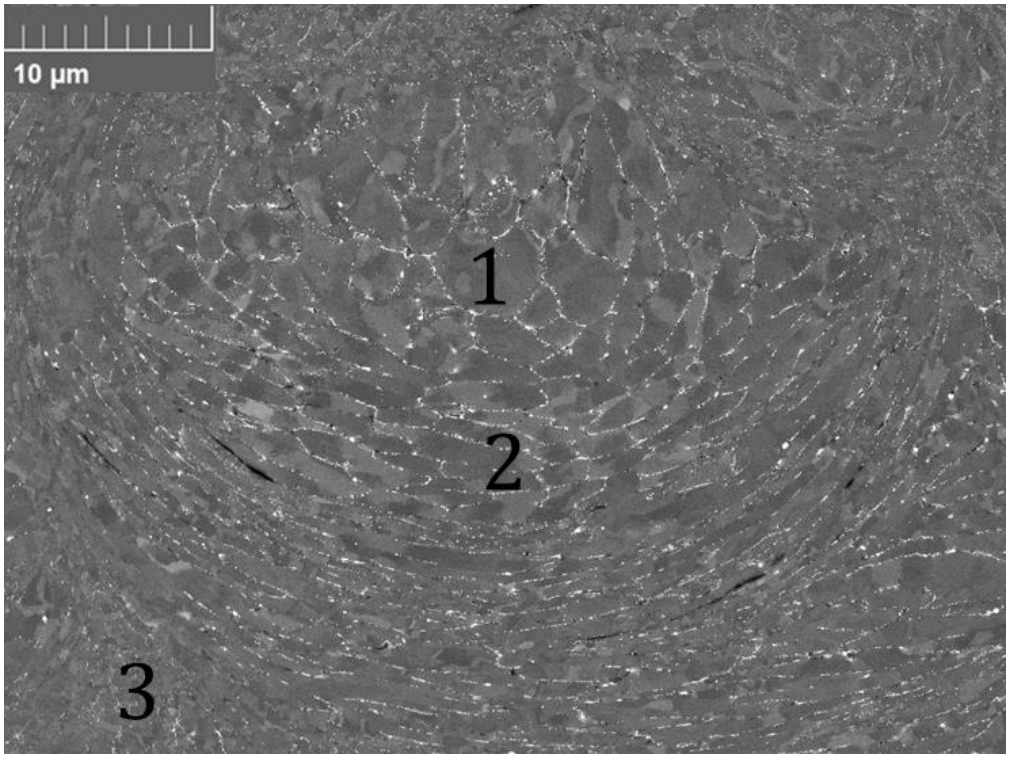

Figure 37. SEM micrograph taken in SE mode of 10 hr sample showing the overall microstructure of a Cold Spray surface 1) low deformation region, 2) medium deformation region, and 3) high deformation region.

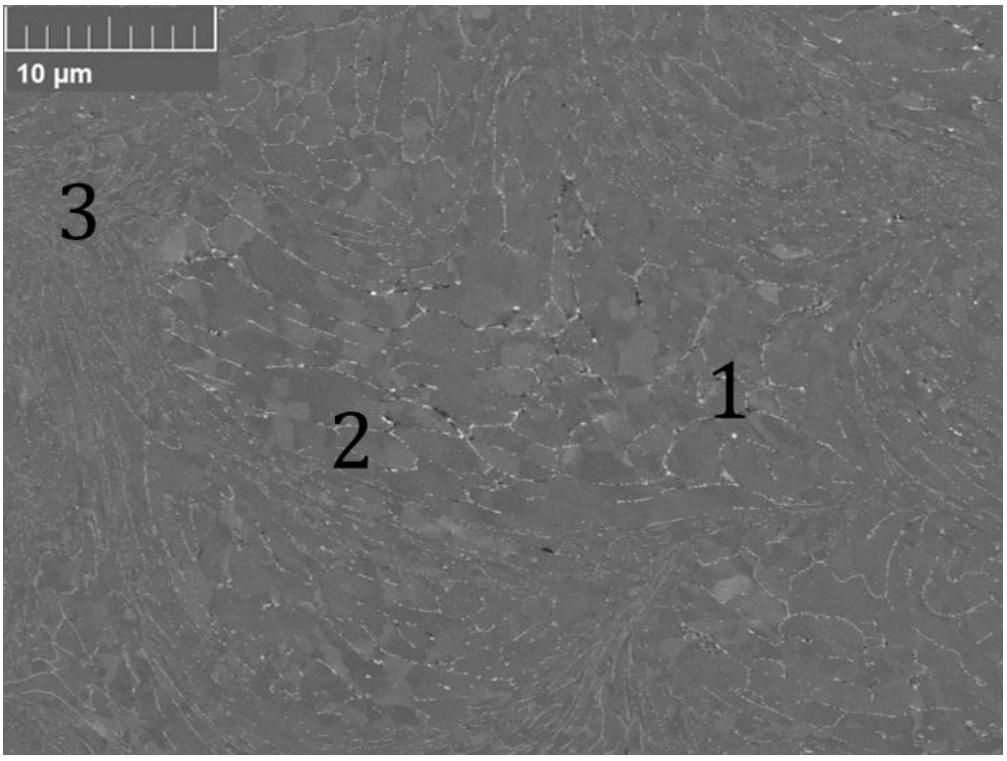

Figure 38. SEM micrograph taken in SE mode of 100 hr sample showing the overall microstructure of a Cold Spray surface 1) low deformation region, 2) medium deformation region, and 3) high deformation region.

4.3 Low Deformation Regions

The grain size of the low deformation regions has a grain diameter on the order of 2 to 3 μm. This grain diameter range for the low deformation regions compares to grain diameter range observed in the powder. SEM micrographs in SE and BSE mode show that the electron beam channeling contrast compared to the inverse pole figure map correlates the difference in grain deformation/misorientation and the "tie-dye" contrast within grains. The SE and BSE images also correlate well to the results of the extrapolated EBSD data to the SE and BSE images on the different contrast. Deformation within the microstructure is shown in the AR sample Figure 36.

The microstructural effects of recovery and recrystallization were observed by interrupted heat treatment from the AR samples through 100 hr. The LAGBs within the material show that there are regions of deformation with excess dislocations from the impact of the powder. No grain growth was observed in the as-received to 100 hr samples. The lack of grain growth could also be due to impurities (i.e. Mg_2Si white outline of grains in SE and BSE micrographs.) which would inhibit grain growth.

The inverse pole figure maps from the low deformation region in as-received to 100 hr sample shows there is no texture, as expected when compared to the original powder sample. The random grain orientation observed is comparable to the random orientation of the original powder. This information shows that the deformation process does not cause the same amount of deformation around the medium deformation region and that the removal of "tie-dye" shows grain recrystallization within grains. For instance, samples AR to 10 hr show "tie-dye", while sample 100 hr show very few grains with "tie-dye" contrast in grains. Figure 51 shows the overall EBSD maps for low deformation regions.

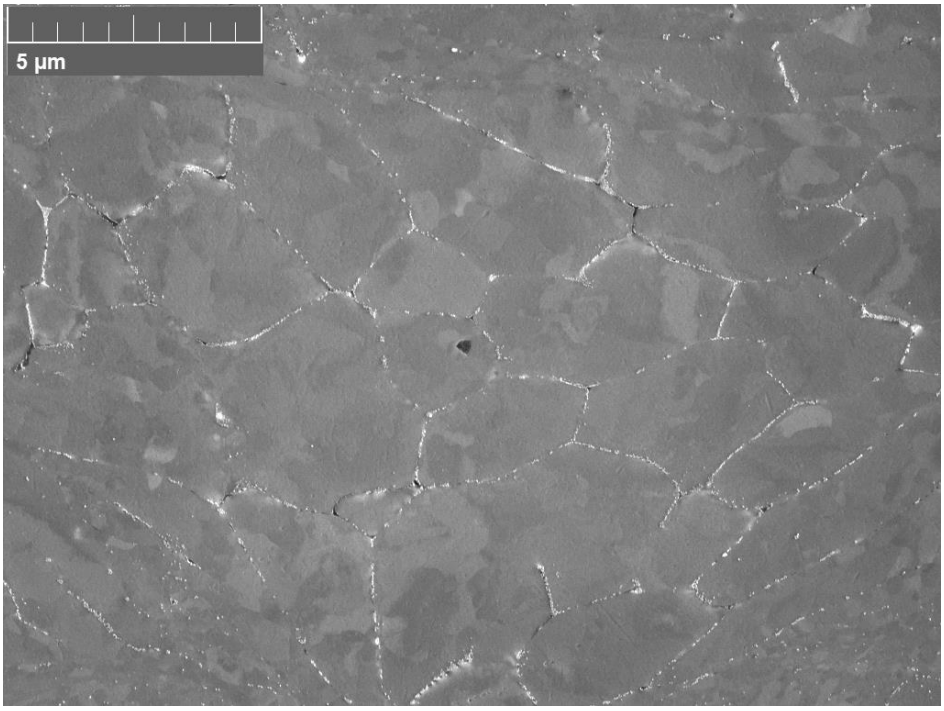

Figure 39. SEM micrograph taken in SE mode of AR low deformation.

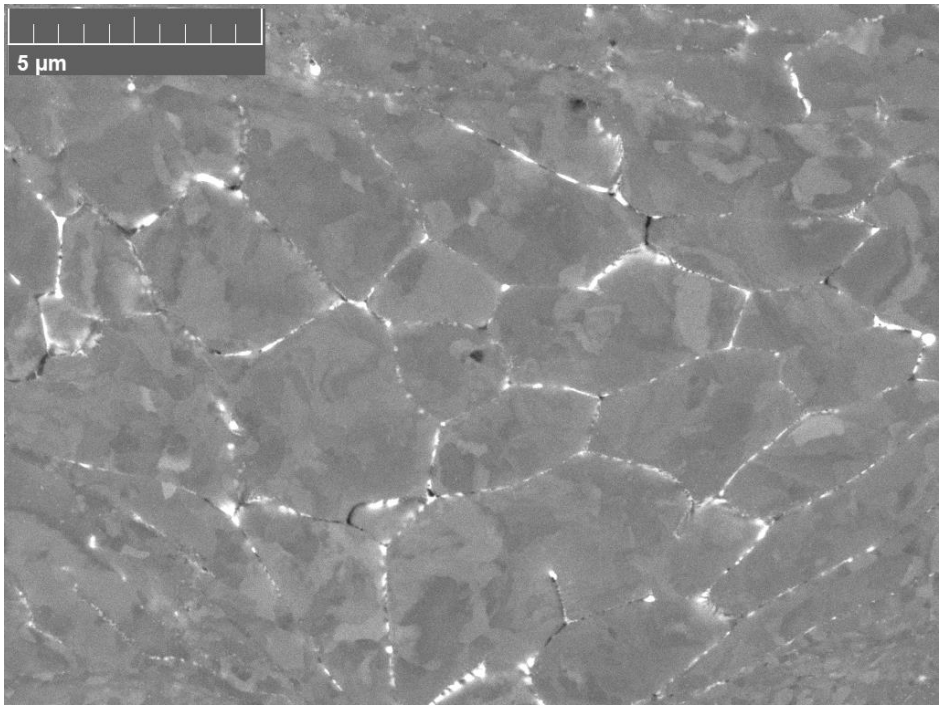

Figure 40. SEM micrograph taken in BSE mode of AR low deformation.

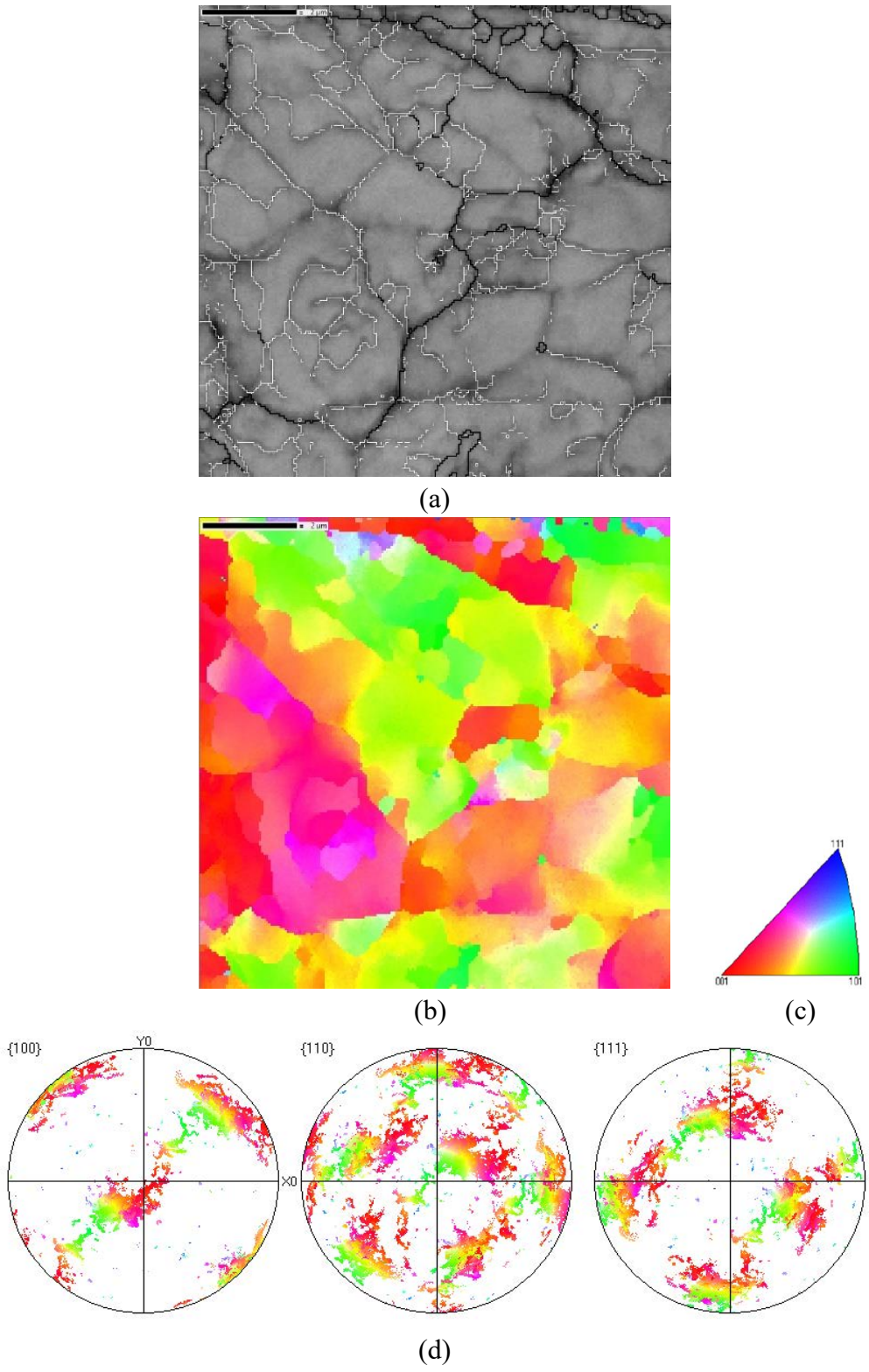

Figure 41. EBSD band contrast image (a) showing grain boundaries for AR low deformation region LAGB (<2.5°) white lines and HAGBs (<15°) black lines. Orthogonal IPF map Z (b) for AR low deformation region. IPF legend (c). Note: 2 µm scale bar is presented in the image. Pole figure map (d) of {100}, {110}, and {111} for IPF.

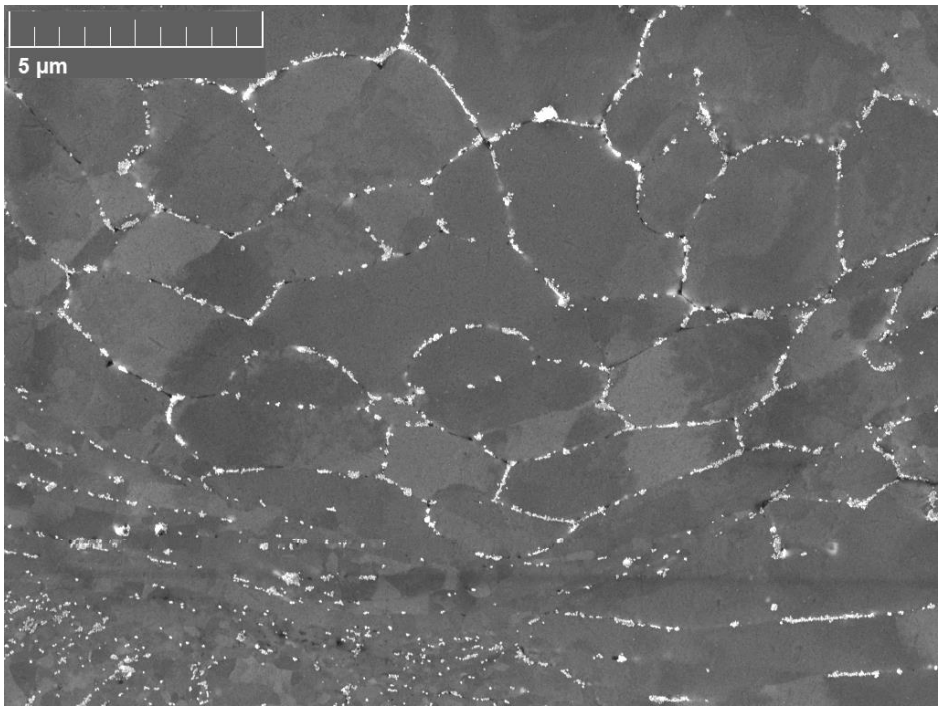

Figure 42. SEM micrograph taken in SE mode of 1 hr low deformation region.

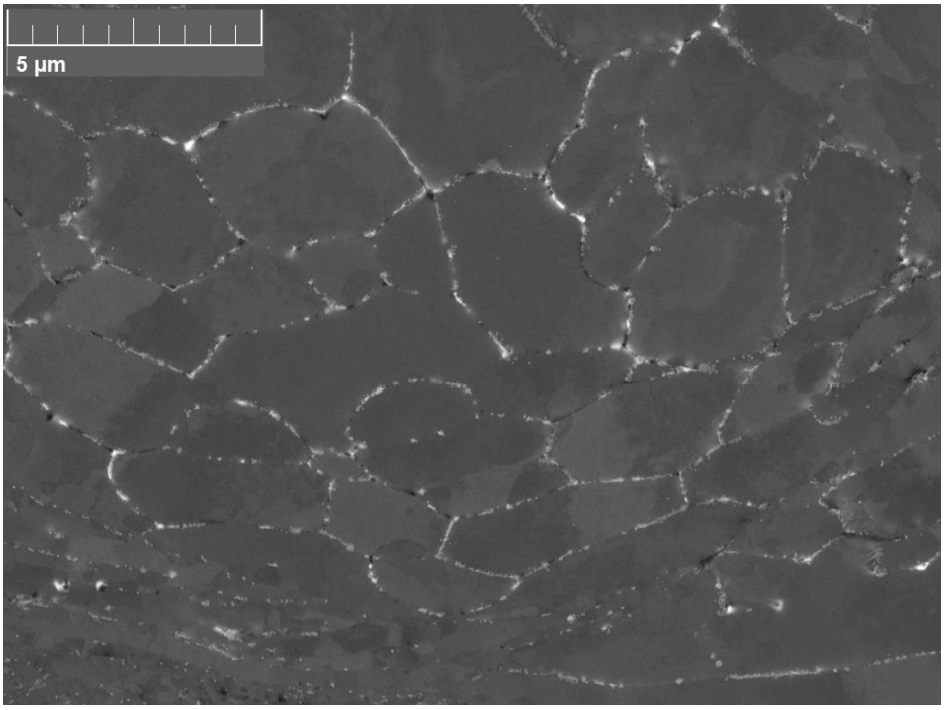

Figure 43. SEM micrograph taken in BSE mode of 1 hr low deformation region.

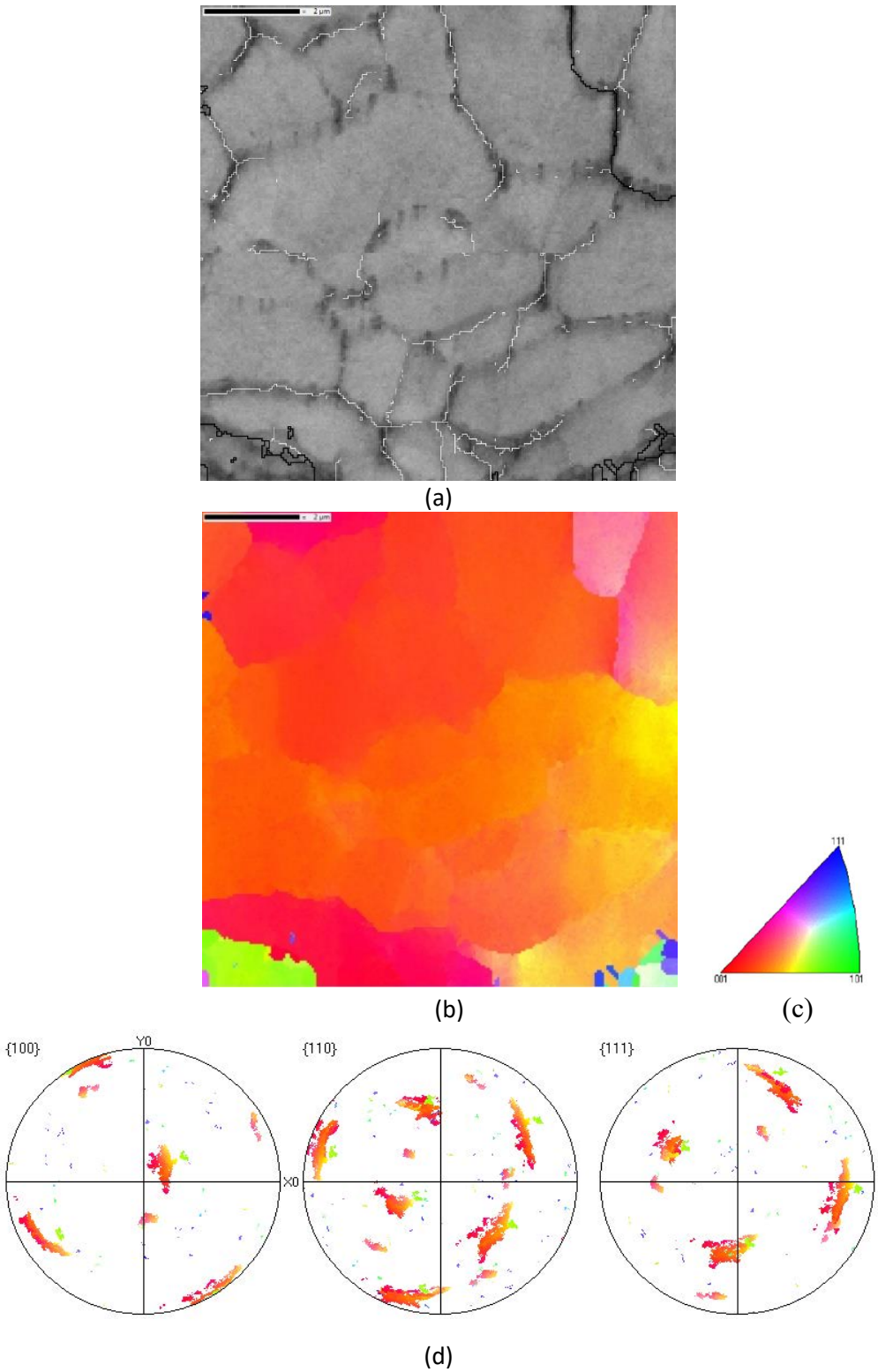

Figure 44. EBSD band contrast image (a) showing grain boundaries for 1 hr low deformation region LAGB (<2.5°) white lines and HAGBs (<15°) black lines. Orthogonal IPF map Z (b) for 1 hr low deformation region. IPF legend (c). Note: 2 µm scale bar is presented in the image. Pole figure map (d) of {100}, {110}, and {111} for IPF.

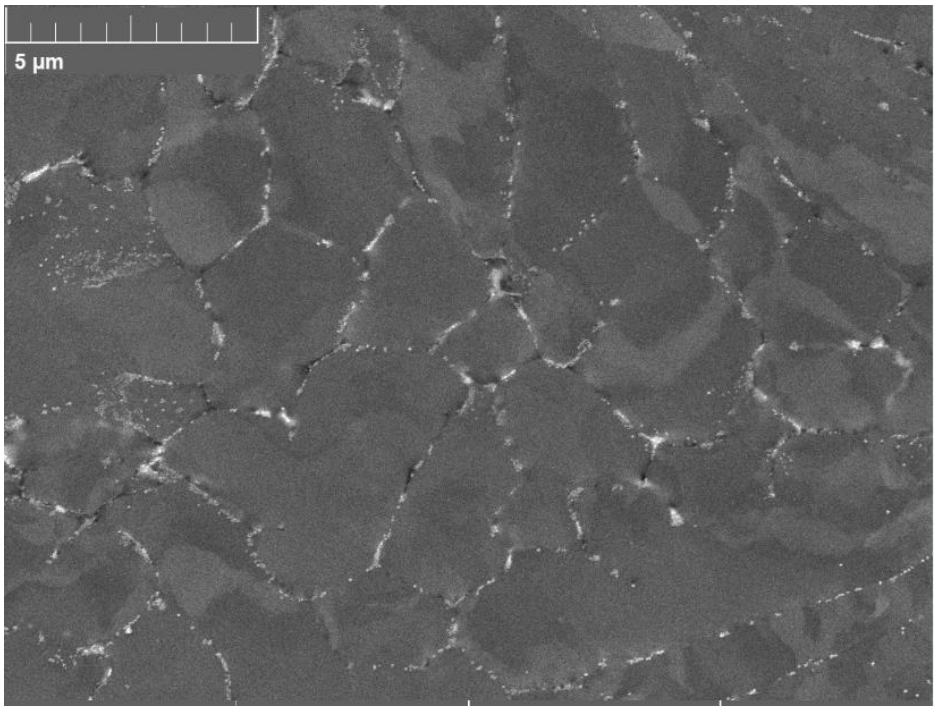

Figure 45. SEM micrograph taken in SE mode of 10 hr low deformation region.

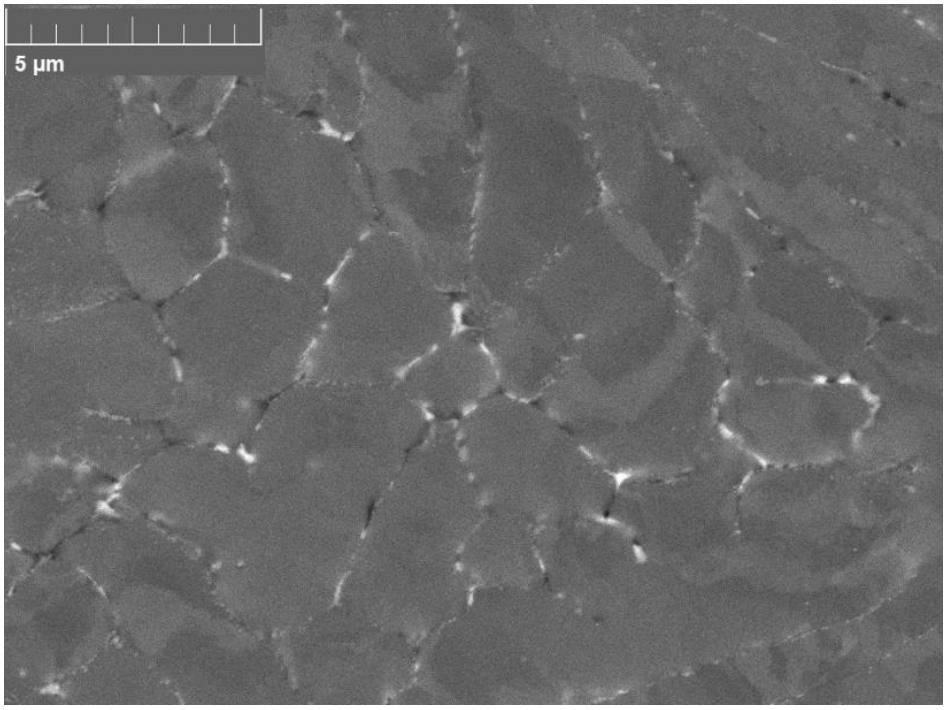

Figure 46. SEM micrograph taken in BSE mode of 10 hr low deformation region.

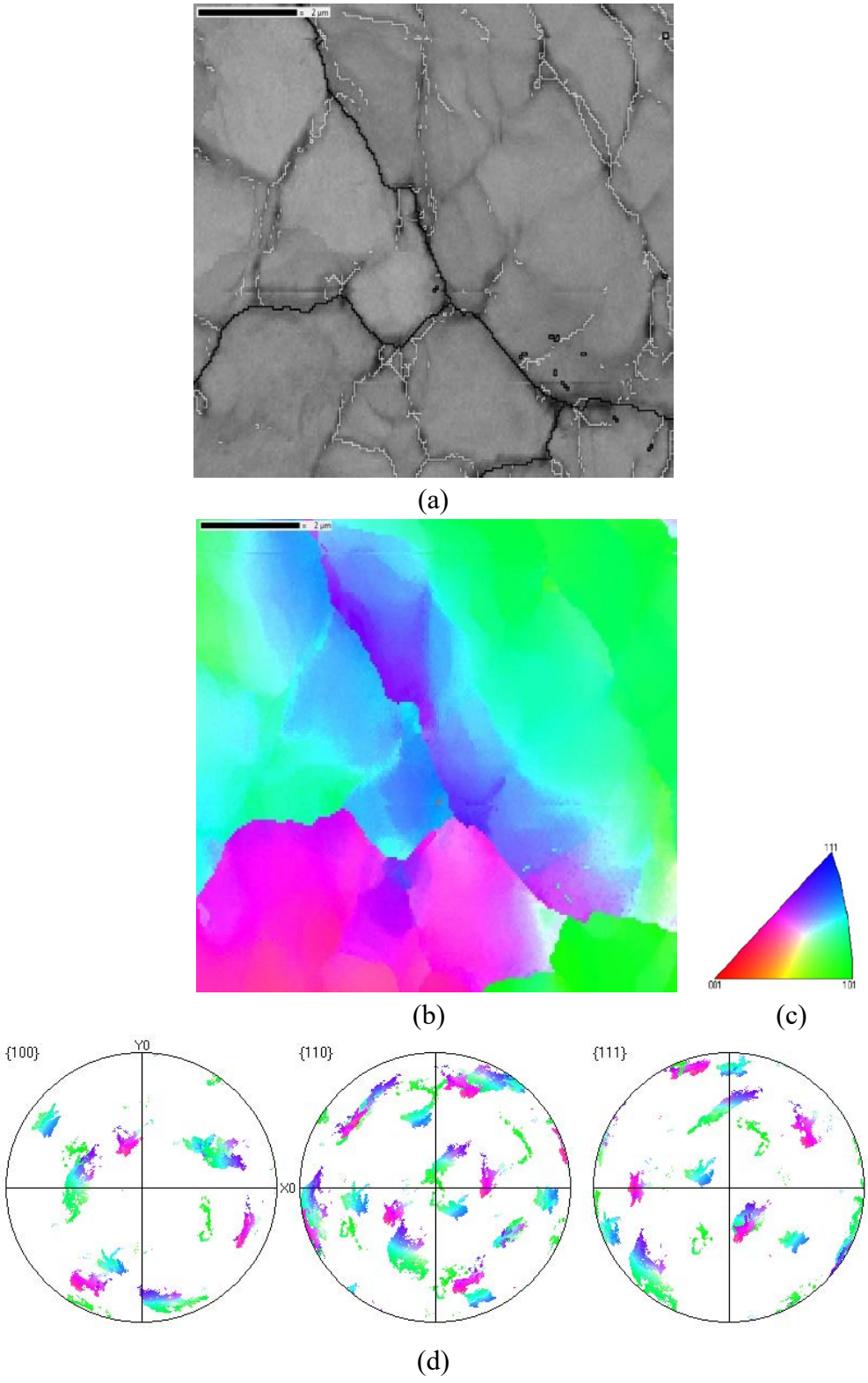

Figure 47. EBSD band contrast image (a) showing grain boundaries for 10 hr low deformation region LAGB (<2.5°) white lines and HAGBs (<15°) black lines. Orthogonal IPF map Z (b) for 10 hr low deformation region. IPF legend (c). Note: 2 µm scale bar is presented in the image. Pole figure map (d) of {100}, {110}, and {111} for IPF.

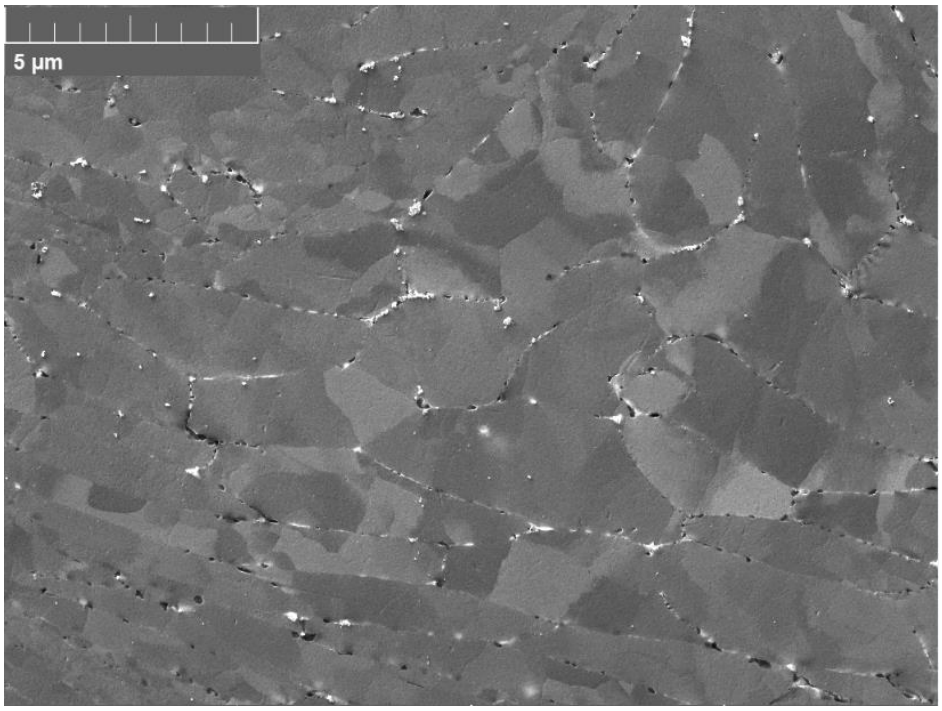

Figure 48. SEM micrograph taken in SE mode of 100 hr low deformation region.

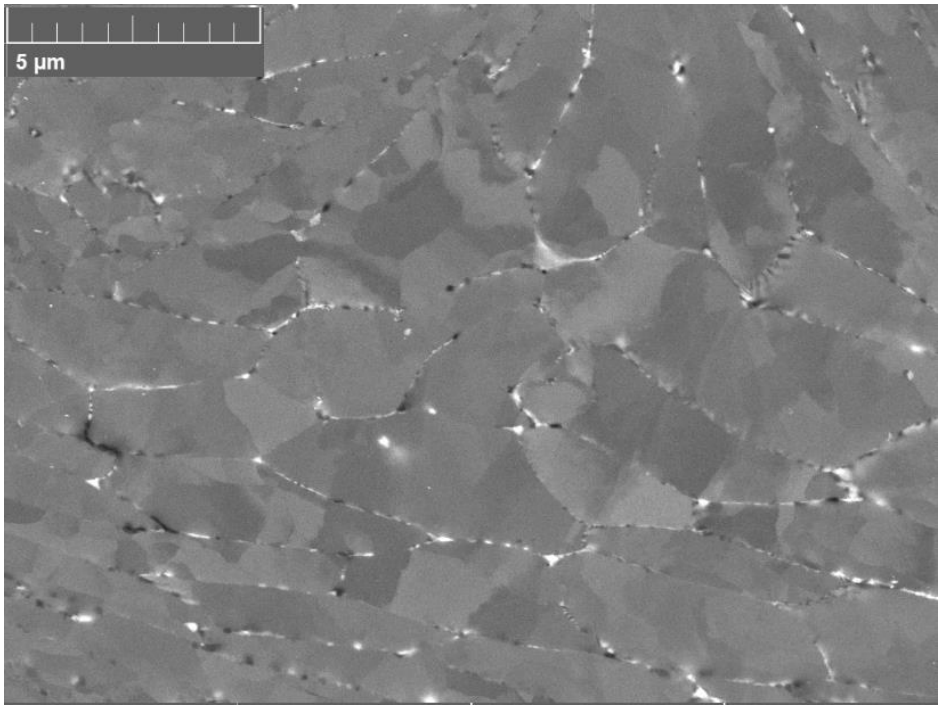

Figure 49. SEM micrograph taken in BSE mode of 100 hr low deformation region.

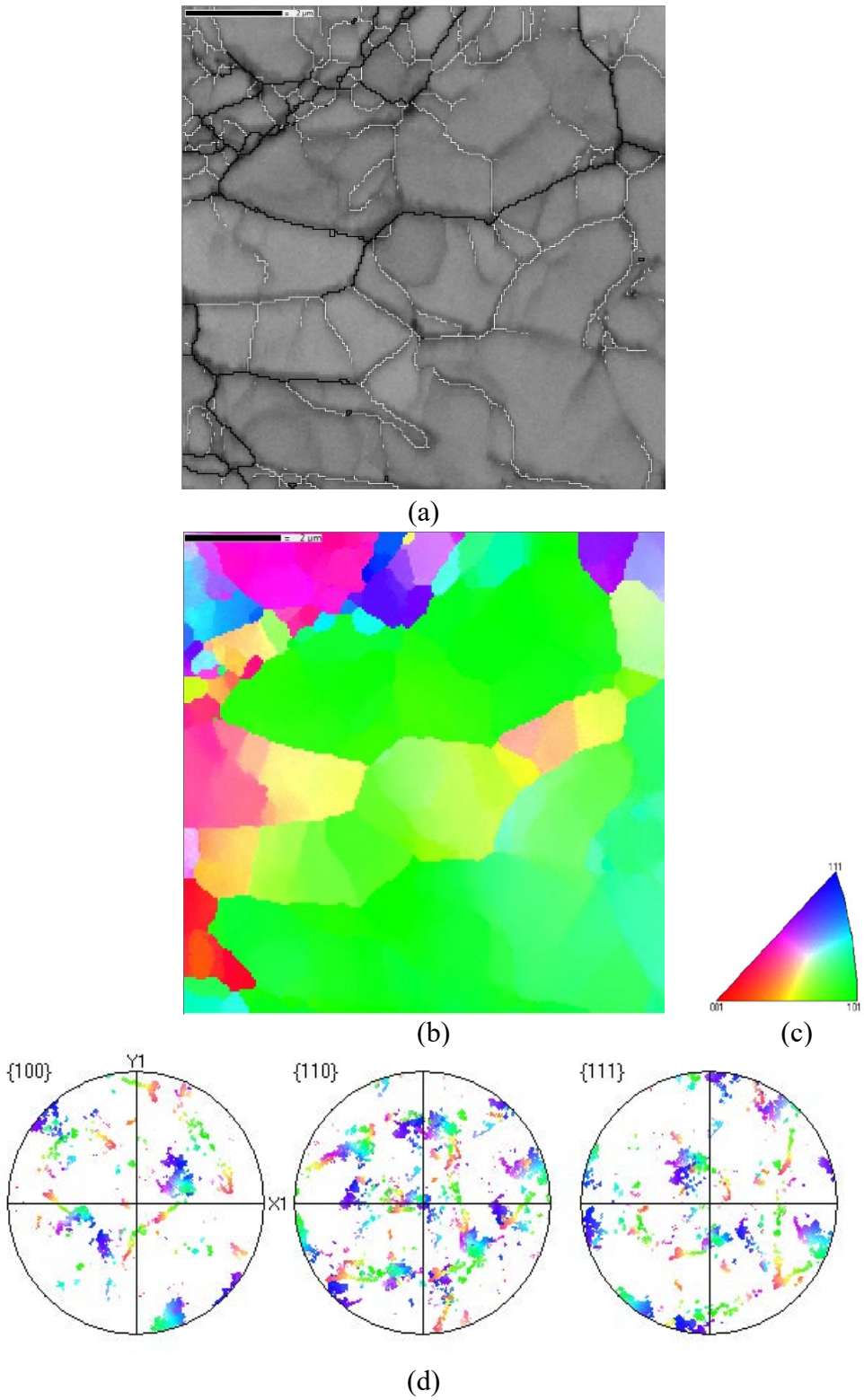

Figure 50. EBSD band contrast image (a) showing grain boundaries for 100 hr low deformation region LAGB (<2.5°) white lines and HAGBs (<15°) black lines. Orthogonal IPF map Z (b) for 100 hr low deformation region. IPF legend (c). Note: 2 µm scale bar is presented in the image. Pole figure map (d) of {100}, {110}, and {111} for IPF.

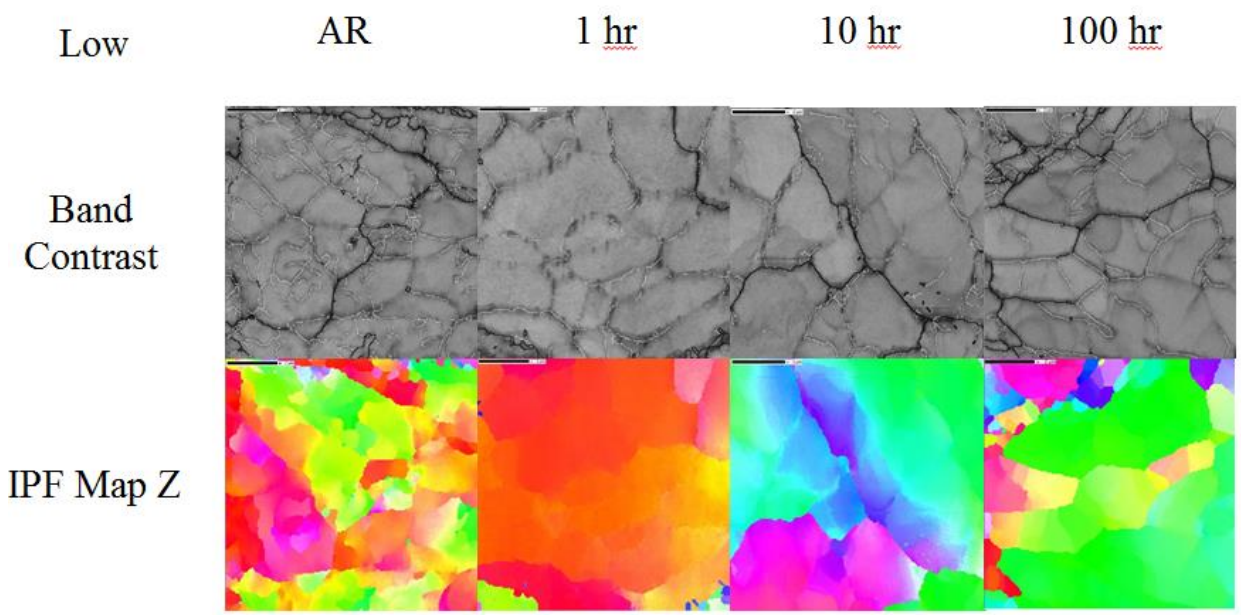

Figure 51. Overall EBSD images of low deformation regions AR, 1 hr, 10 hr, and 100 hr.

4.4 220 AR Medium Deformation Regions

The average grain size for Medium deformation region was determined to be approximately 1 μm to 2 μm for the AR, 1 hr, 10hr, and 100 hr sample. In the medium deformation regions, grains do not appear equiaxed compared to the powder and low deformation regions. This shows that there is approximately a 50 percent reduction in the width of the grains as compared to the powder and low deformation regions, associated with plastic deformation from the impact process. The reduction in width shows that the medium deformation regions undergo higher deformation than the low deformation regions. SEM micrographs in SE and BSE mode show that the electron beam channeling contrast correlates to the inverse pole figure map and shows the difference in grain deformation and the "tie-dye" contrast within grains. The SE and BSE images also correlate the results of the extrapolated EBSD data to the SE and BSE images on the different contrast. Note: no micrograph of SE or BSE for medium deformation region 1 hr was imaged because it was not relocated after EBSD.

The microstructural effects of recovery and recrystallization were observed through the AR to 100 hr samples. The observation of the medium deformation region for the annealing response was similar to the low deformation region.

The inverse pole figure maps from the medium deformation region as-received to 100 hr sample shows that there is no texture that developed during annealing. This information shows that the deformation process does not cause the same amount of deformation around the medium deformation region and that the removal of "tie-dye" shows grain recrystallization within grains. Thus, because the grains did not fully recrystallize and nucleate into a different grain the grains could not change orientation. For instance samples AR to 1 hr show "tie-dye", while samples 10 and 100 hr show very few grains with "tie-dye" contrast in grains. Figure 62 shows the overall

EBSD maps for medium deformation regions. Additional EBSD maps can be found in appendix A.

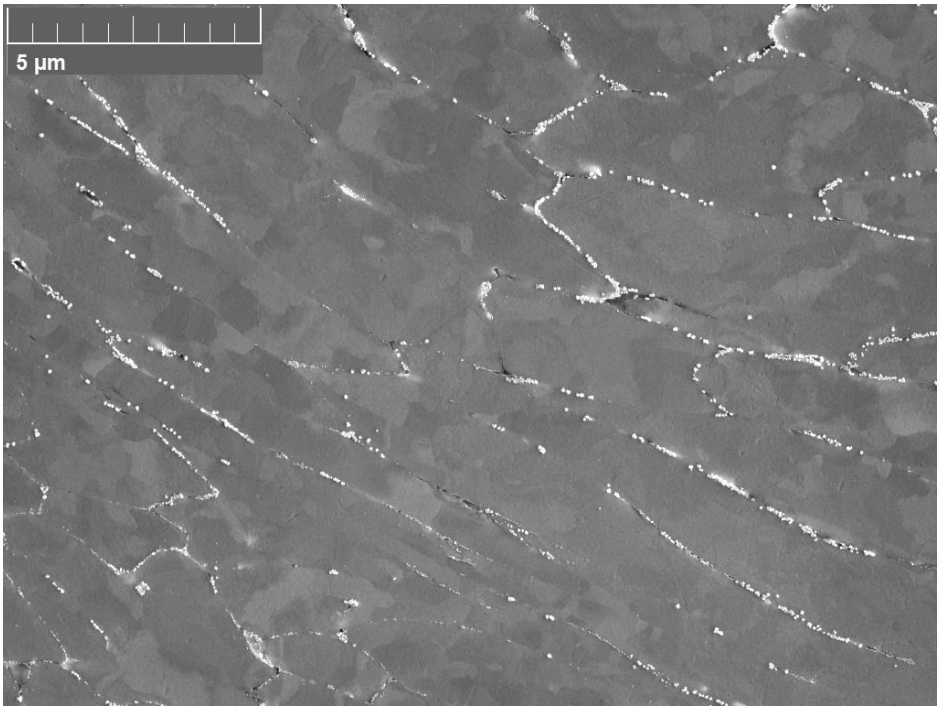

Figure 52. SEM micrograph taken in SE mode of AR medium deformation region.

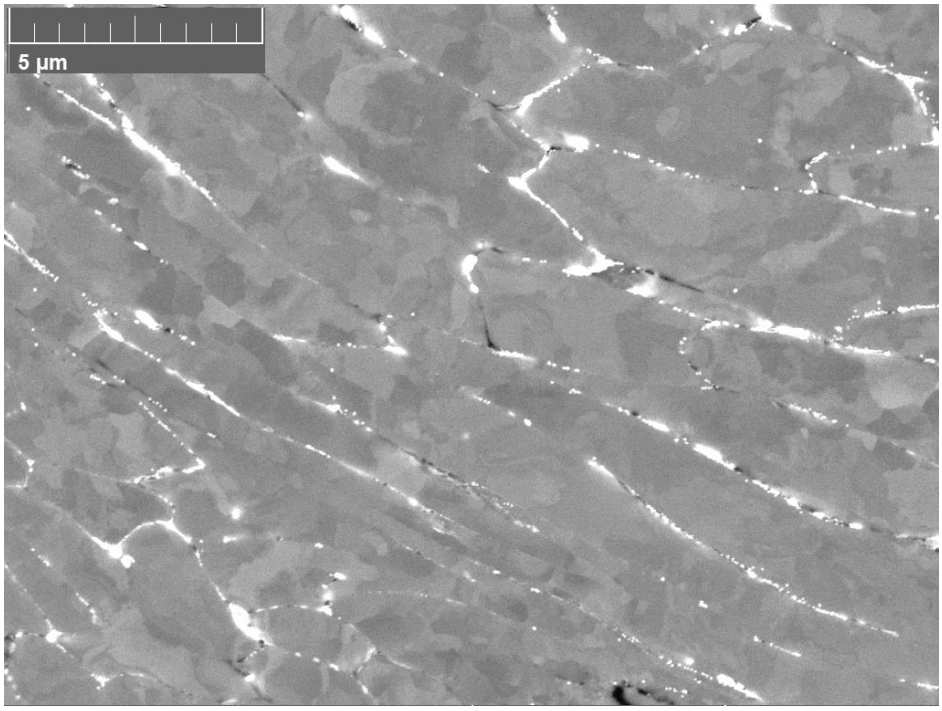

Figure 53. SEM micrograph taken in BSE mode of AR medium deformation region.

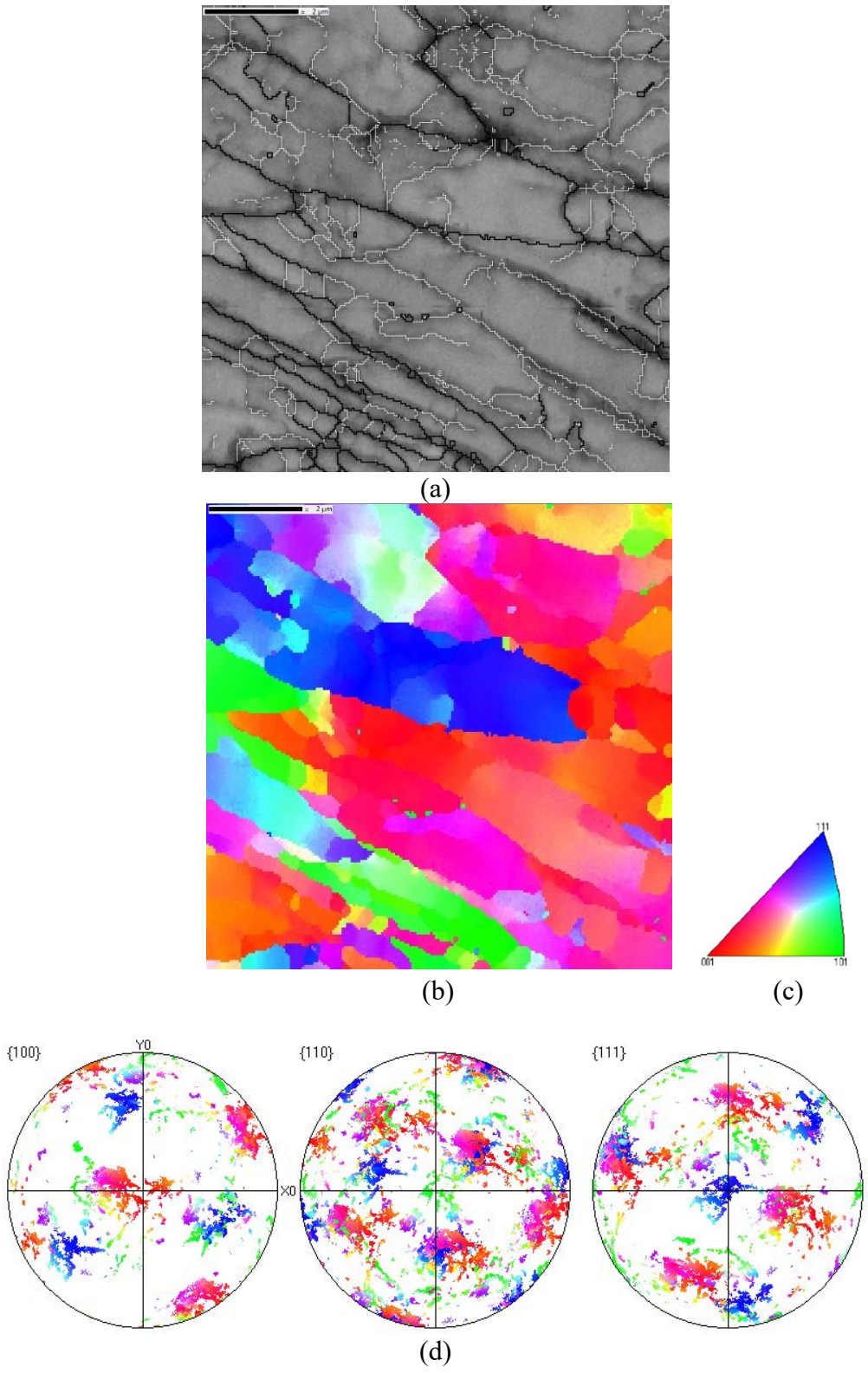

Figure 54. EBSD band contrast image (a) showing grain boundaries for AR medium deformation region site LAGB (<2.5°) white lines and HAGBs (<15°) black lines. Orthogonal IPF map Z (b) for AR medium deformation region. IPF legend (c). Note: 2 µm scale bar is presented in the image. Pole figure map (d) of {100}, {110}, and {111}.

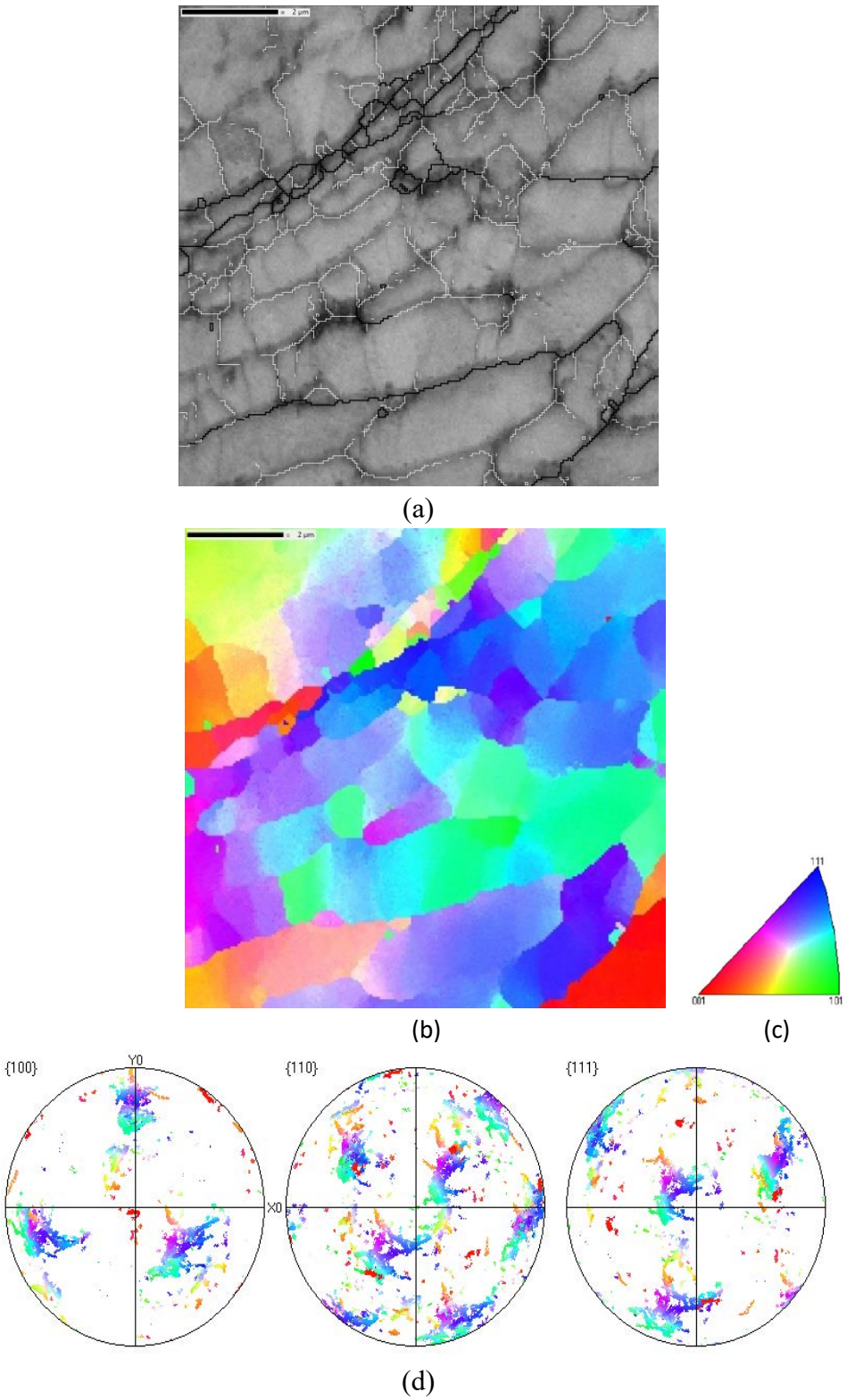

Figure 55. EBSD band contrast image (a) showing grain boundaries for 1 hr medium deformation region LAGB (<2.5°) white lines and HAGBs (<15°) black lines. Orthogonal IPF map Z (b) for 1 hr medium deformation region. IPF legend (c). Note: 2 µm scale bar is presented in the image. Pole figure map (d) of {100}, {110}, and {111}.

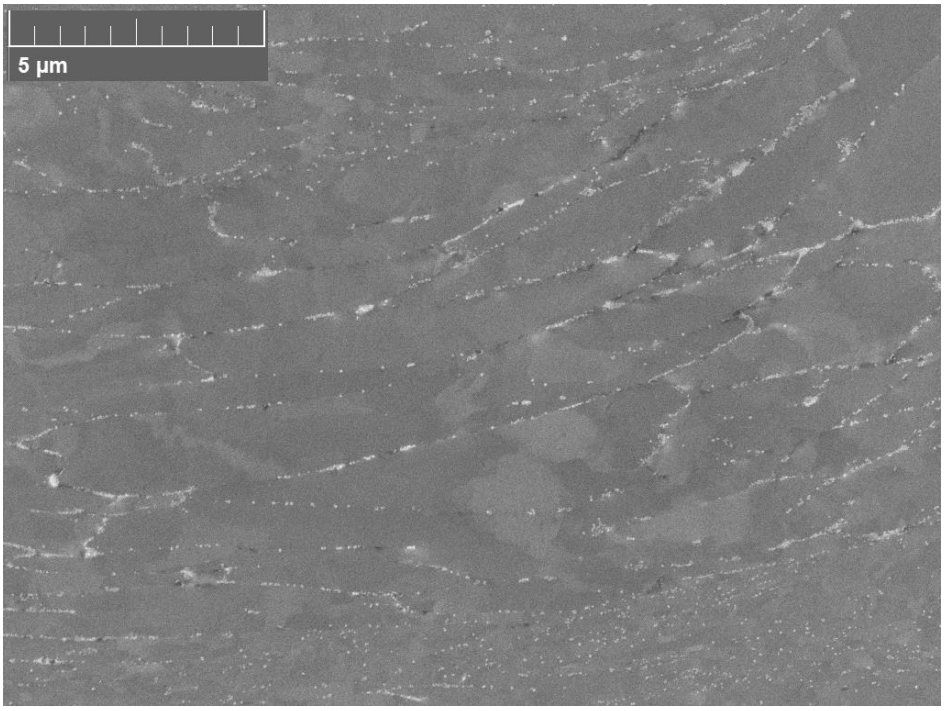

Figure 56. SEM micrograph taken in SE mode of 10 hr medium deformation region.

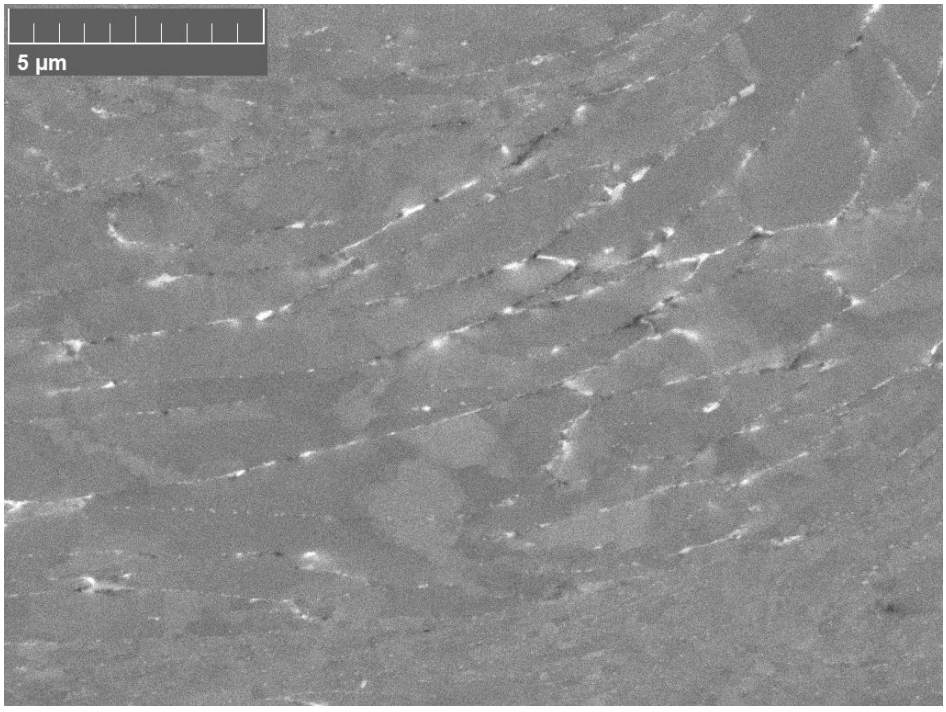

Figure 57. SEM micrograph taken in BSE mode of 10 hr medium deformation region.

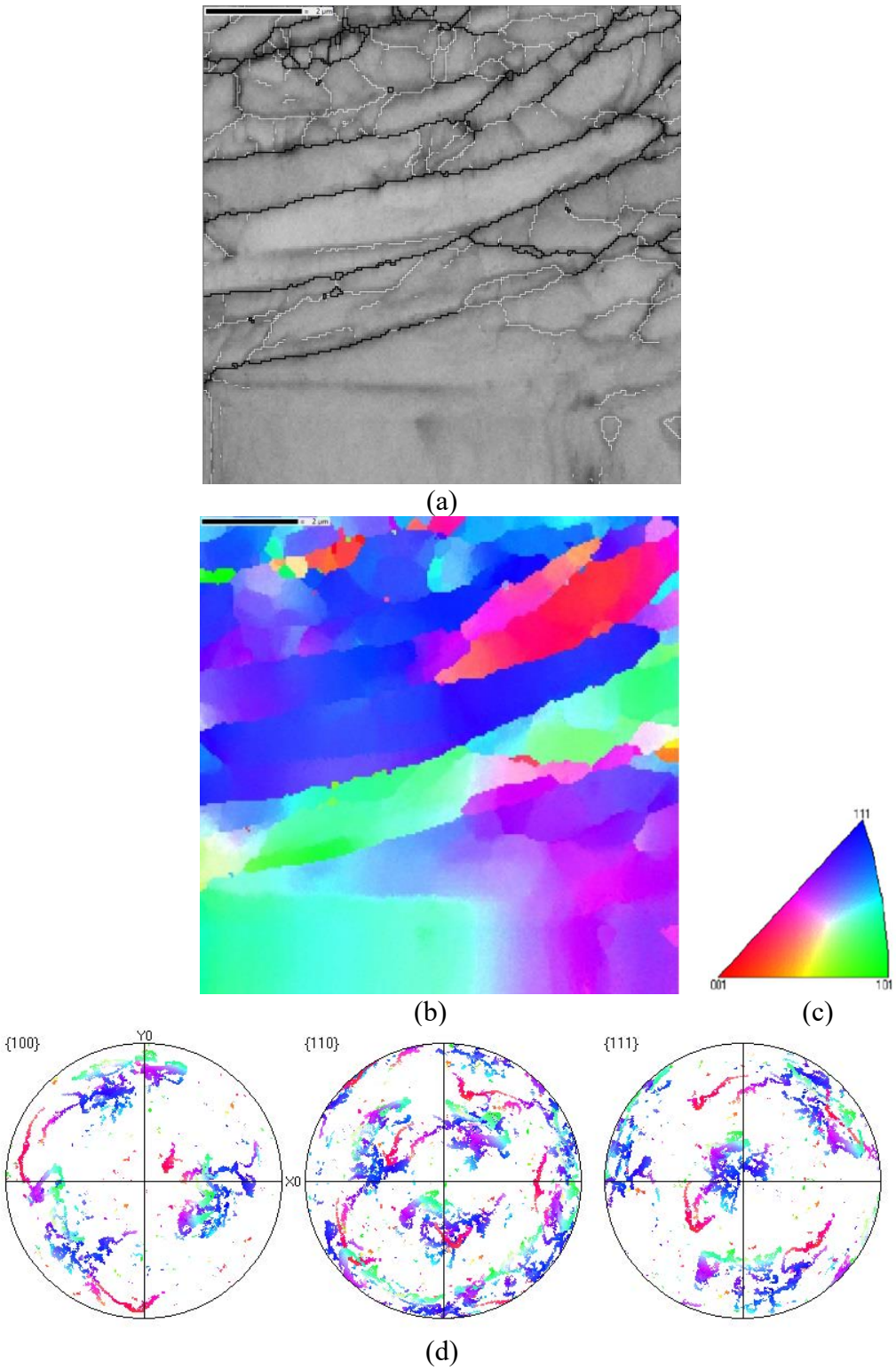

Figure 58. EBSD band contrast image (a) showing grain boundaries for 10 hr medium deformation region LAGB (<2.5°) white lines and HAGBs (<15°) black lines. Orthogonal IPF map Z (b) for 10 hr medium deformation region. IPF legend (c). Note: 2 µm scale bar is presented in the image. Pole figure map (d) of {100}, {110}, and {111}.

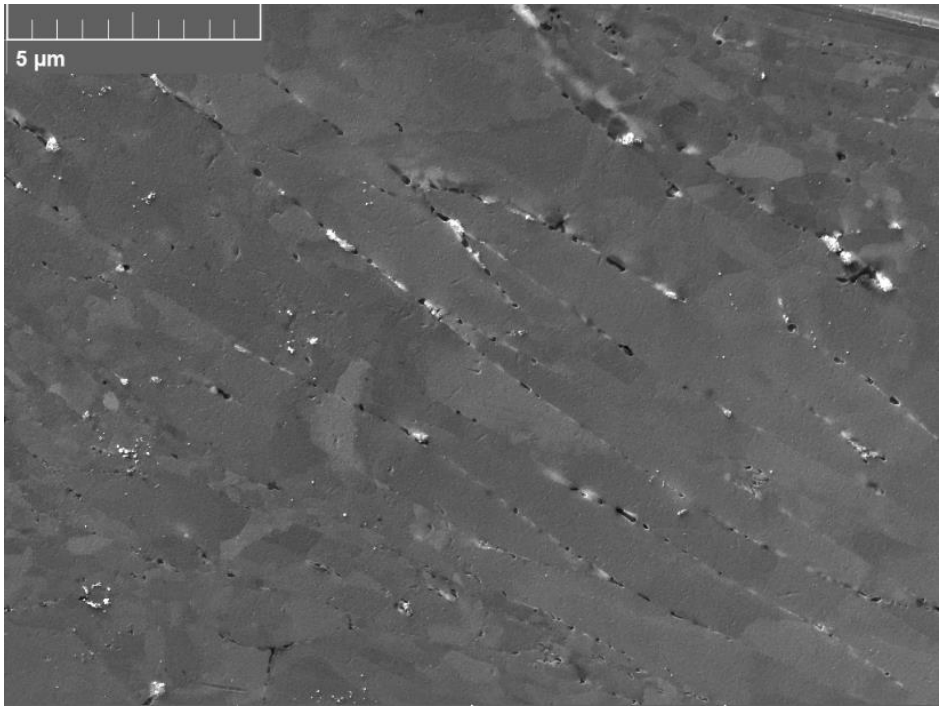

Figure 59. SEM micrograph taken in SE mode of 100 hour medium deformation region.

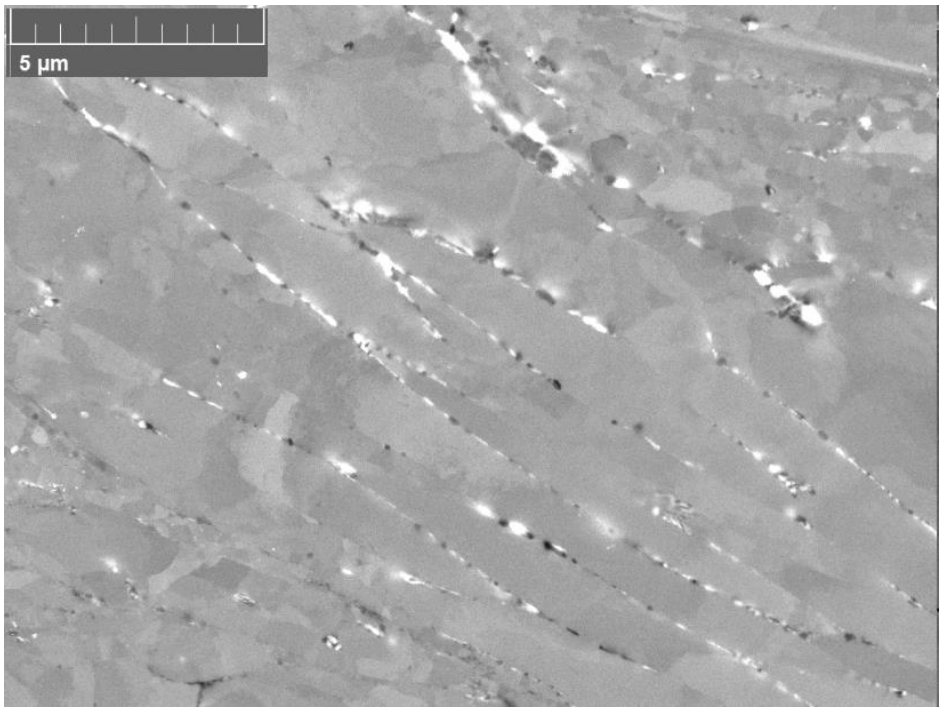

Figure 60. SEM micrograph taken in BSE mode of 100 hour medium deformation region.

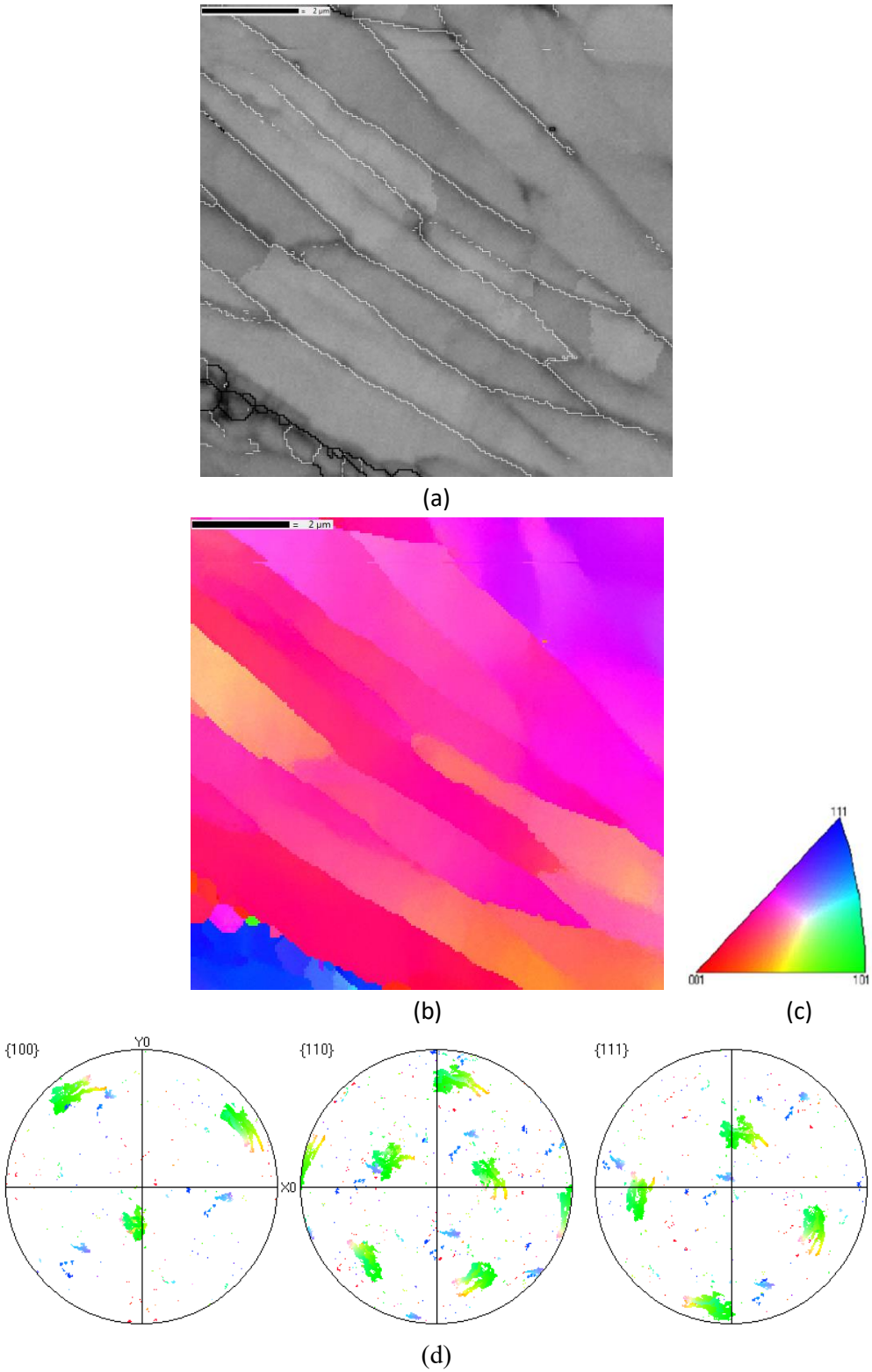

Figure 61. EBSD band contrast image (a) showing grain boundaries for 100 hr medium deformation region LAGB (<2.5°) white lines and HAGBs (<15°) black lines. Orthogonal IPF map Z (b) for 100 hr medium deformation region. IPF legend (d). Note: 2 µm scale bar is presented in the image. Pole figure map (d) of {100}, {110}, and {111}.

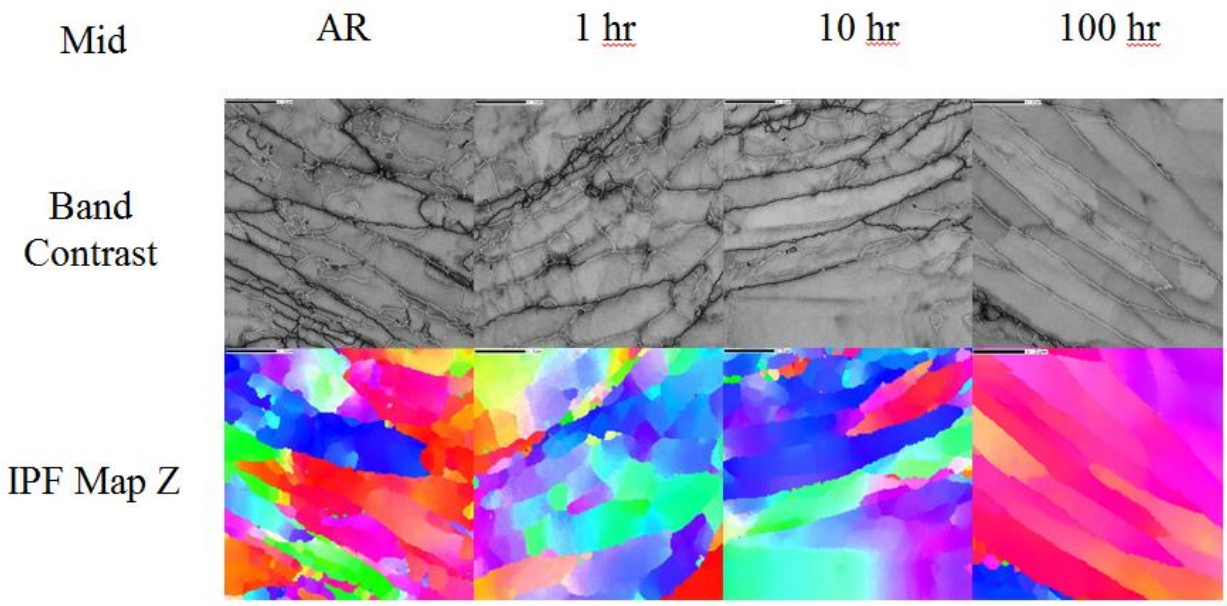

Figure 62. Overall EBSD images of medium deformation regions AR, 1 hr, 10 hr, and 100 hr.

4.5 220 High Deformation Regions

The average grain size for high deformation region was determined to be on the order of 241 nm for the AR deposit, with the smallest measured grain being roughly 30 to 40 nm (99% grain reduction in diameter). This reduction in diameter shows that the high deformation region has undergone recrystallization, most likely due to dynamic recrystallization. After 1 hr of heating, the average grain size was observed to be approximately 496 nm. For 10 hr, the average grain size is approximately 540 nm. Finally, for the 100 hr sample, the average grain size is approximately 589 nm. The reduction in grain size shows that the high deformation regions undergo higher deformation than the medium and low deformation regions. SEM micrographs in SE and BSE mode show that the electron beam channeling contrast compared to the inverse pole figure map shows the difference in grain deformation and that the "tie-dye" contrast within grains is no longer present. The SE and BSE images also compare the results of the extrapolated EBSD data to the SE and BSE images on the different contrast. Note: no micrograph of SE or BSE for high deformation region 10 hr was imaged because it was not relocated after EBSD. Figure 75 shows the high deformation region after ion milling to correlate with the as-received samples prepared from polishing.

The micrographs and EBSD provide data to show that the AR high deformation regions have undergone recrystallization as evidence by the grain size and non-existent "tie-dye" contrast. The recrystallization in the AR could be due to dynamic recrystallization or static recrystallization. The dynamic recrystallization could be caused by the induced strain from the powder impact. The static recrystallization could be caused by the strain increasing as another or multiple other powders impact the original powder inducing enough strain to cause recrystallization with a sufficient gas stream temperature. While the static recrystallization is

probable the dynamic recrystallization is far more likely, due to the insufficient gas stream temperature.

The inverse pole figures of the high deformation regions from the AR sample shows deformation within a grain after the grain has already been recrystallized. This extra strain within the grain could cause strain induced boundary migration from AR to 1 hr. The grain orientation from the AR to 1 hr, 10 hr and 100 hr samples are more randomized and start to become less scattered as the annealing time increases, which indicates a reduction in the number of grains with a simultaneous increase in the size of the grains. Figure 74 shows the overall EBSD maps for high deformation regions. Additional EBSD maps can be found in appendix A.

The high deformation regions have undergone grain growth from the annealing process. The grain growth from the AR state to 1 hr could undergo strain induced boundary migration and grain growth from the free surface energy effects. The grain data follows a logarithmic trend shown in Figure 73. Appendix B refers to the grain data that was used for this analysis.

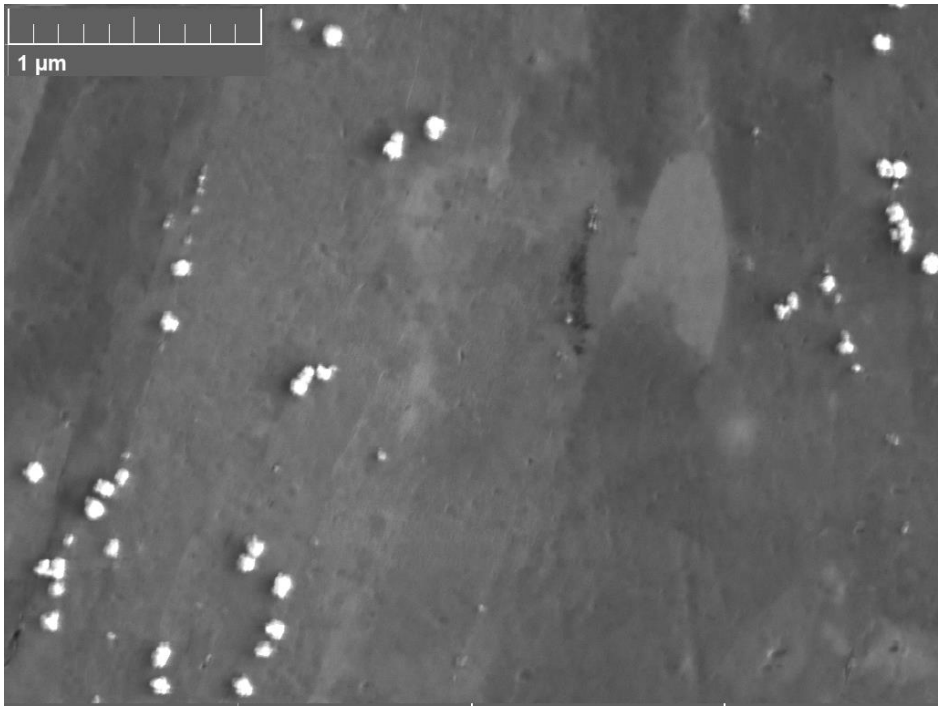

Figure 63. SEM micrograph taken in SE mode of AR high deformation region.

Figure 64. SEM micrograph taken in BSE mode of AR high deformation region.

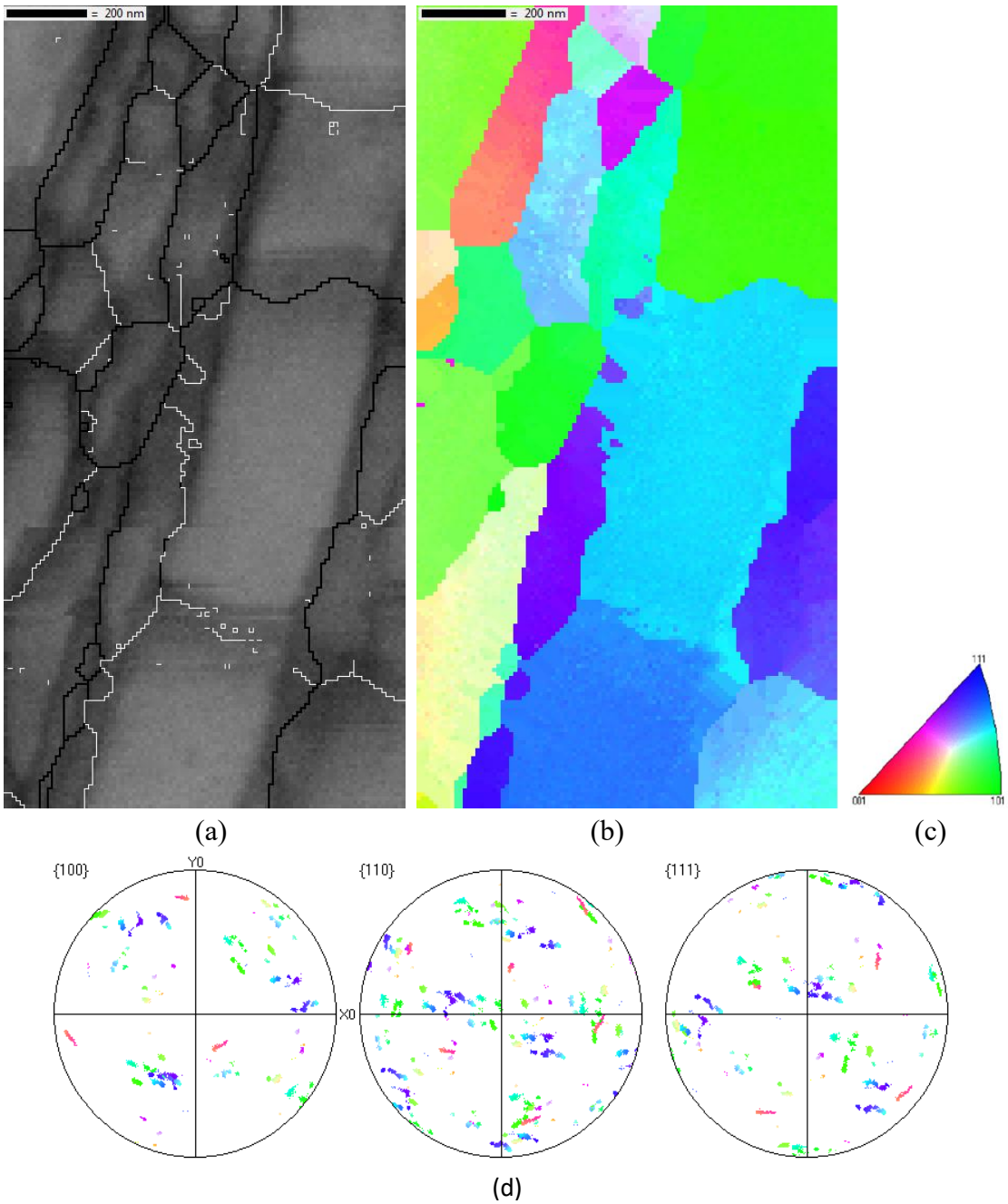

Figure 65. EBSD band contrast image (a) showing grain boundaries for AR high deformation region LAGB (<2.5°) white lines and HAGBs (<15°) black lines.Orthogonal IPF map Z (b) for AR high deformation region. IPF legend (c). Note: 200 nm scale bar is presented in the image. Pole figure map (d) of {100}, {110}, and {111}.

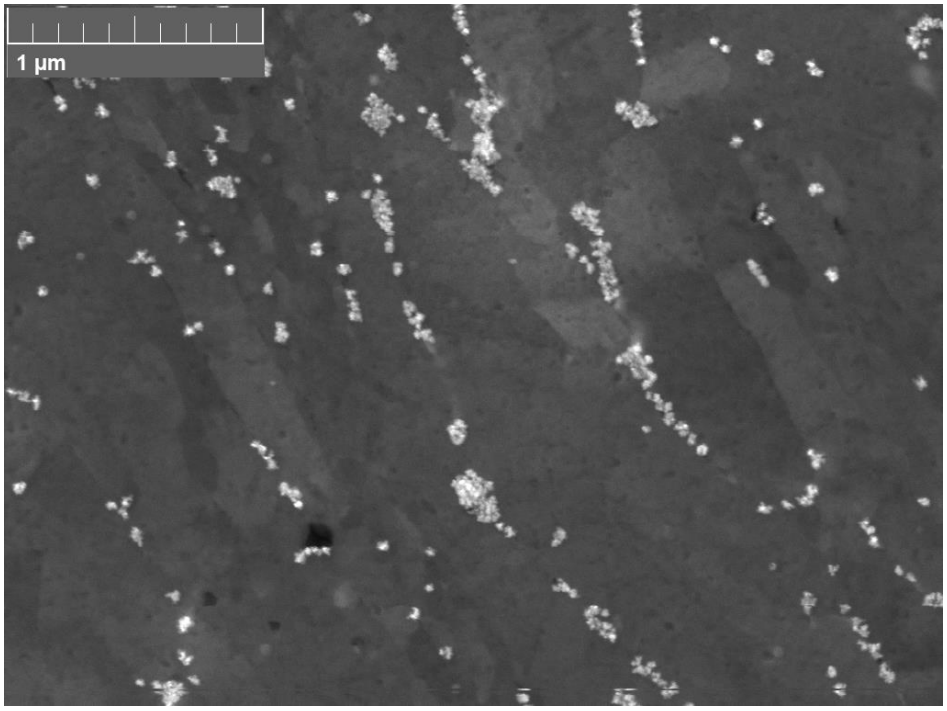

Figure 66. SEM micrograph taken in SE mode of 1 hr high deformation region.

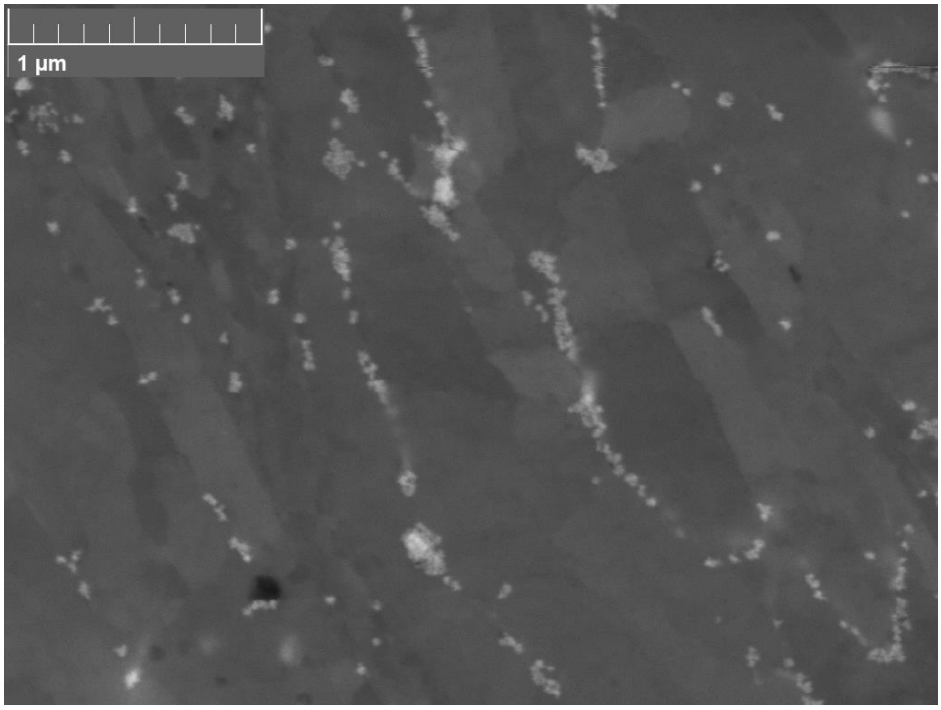

Figure 67. SEM micrograph taken in BSE mode of 1 hr high deformation region.

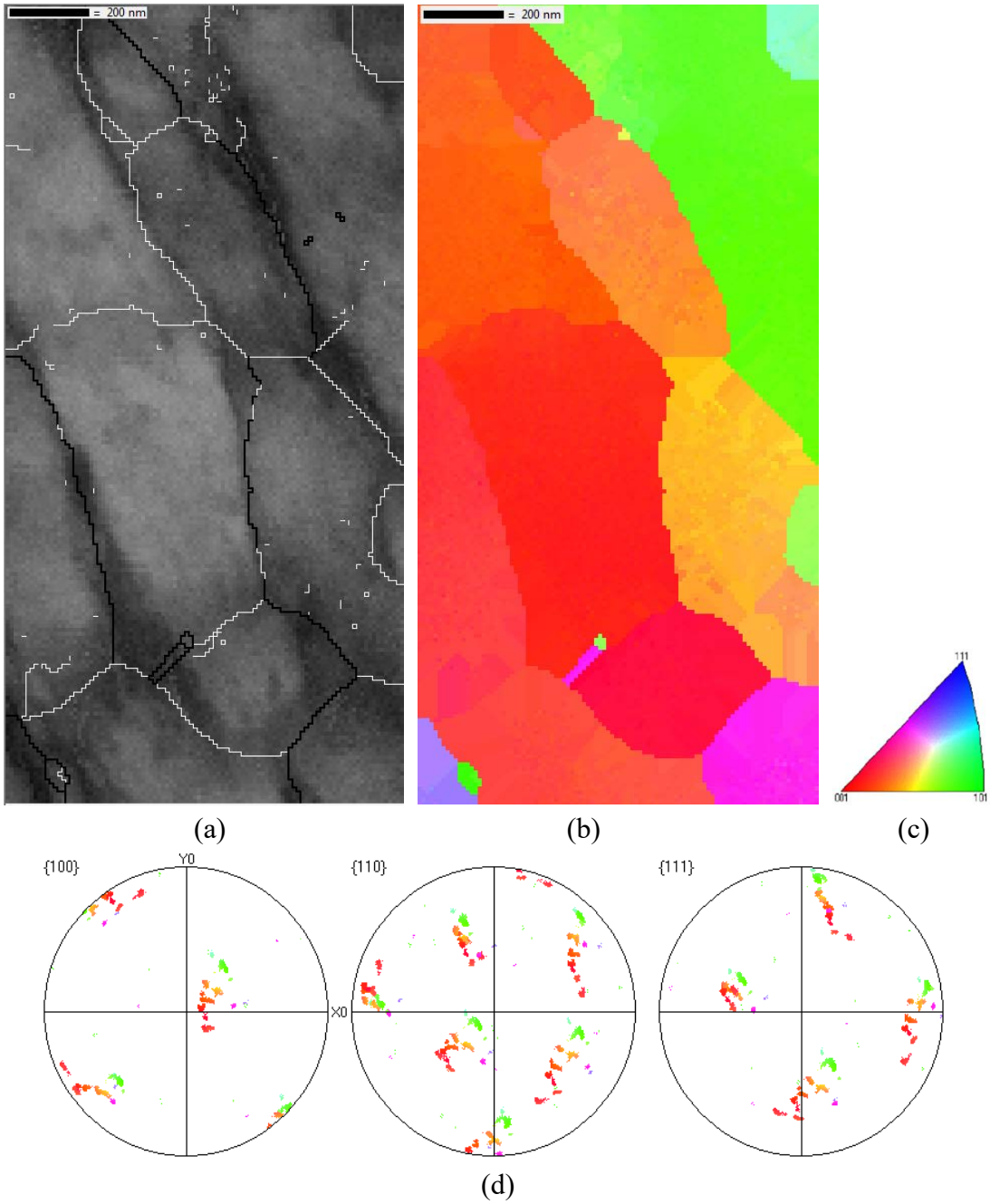

Figure 68. EBSD band contrast image (a) showing grain boundaries for 1 hr high deformation region LAGB (<2.5°) white lines and HAGBs (<15°) black lines. Orthogonal IPF map Z (b) for 1 hr high deformation region. IPF legend (c). Note: 200 nm scale bar is presented in the image. Pole figure map (d) of {100}, {110}, and {111}.

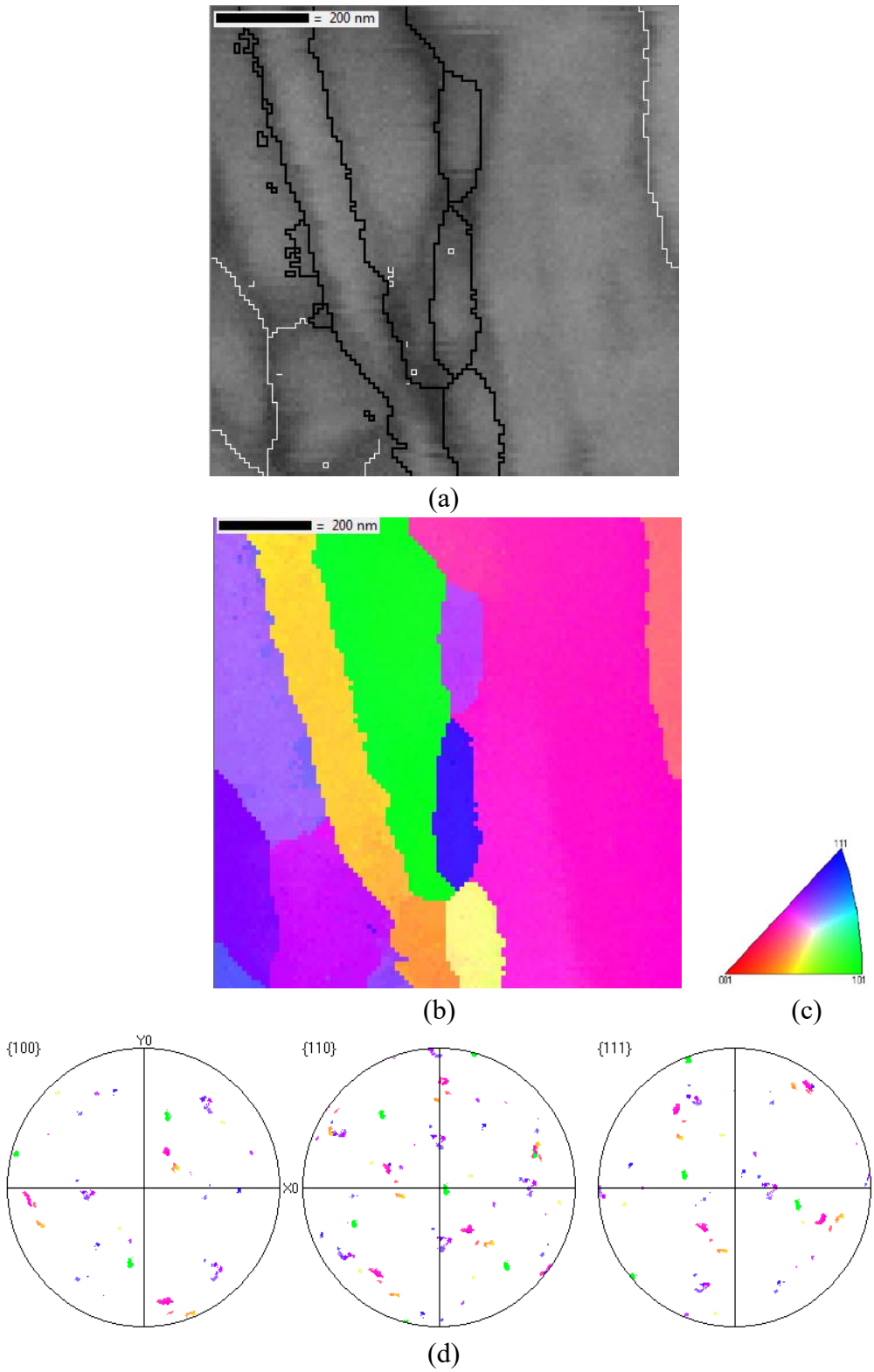

Figure 69. EBSD band contrast image (a) showing grain boundaries for 10 hr high deformation region LAGB (<2.5°) white lines and HAGBs (<15°) black lines. Orthogonal IPF map Z (b) for 10 hr high deformation region. IPF legend (c). Note: 200 nm scale bar is presented in the image. Pole figure map (d) of {100}, {110}, and {111}.

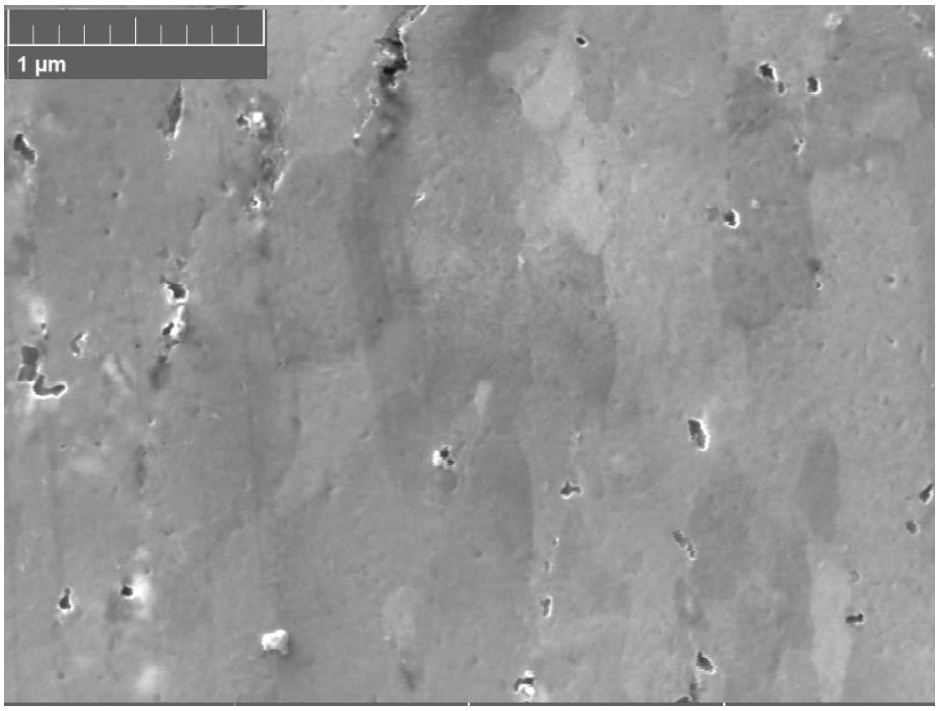

Figure 70. SEM micrograph taken in SE mode of 100 hour high deformation region.

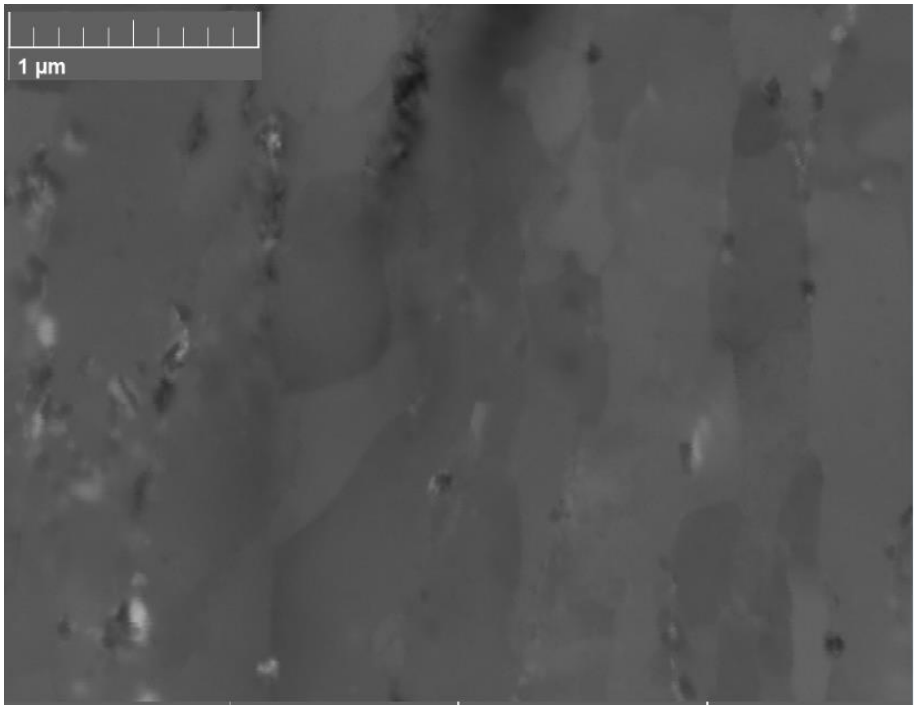

Figure 71. SEM micrograph taken in BSE mode of 100 hour high deformation region.

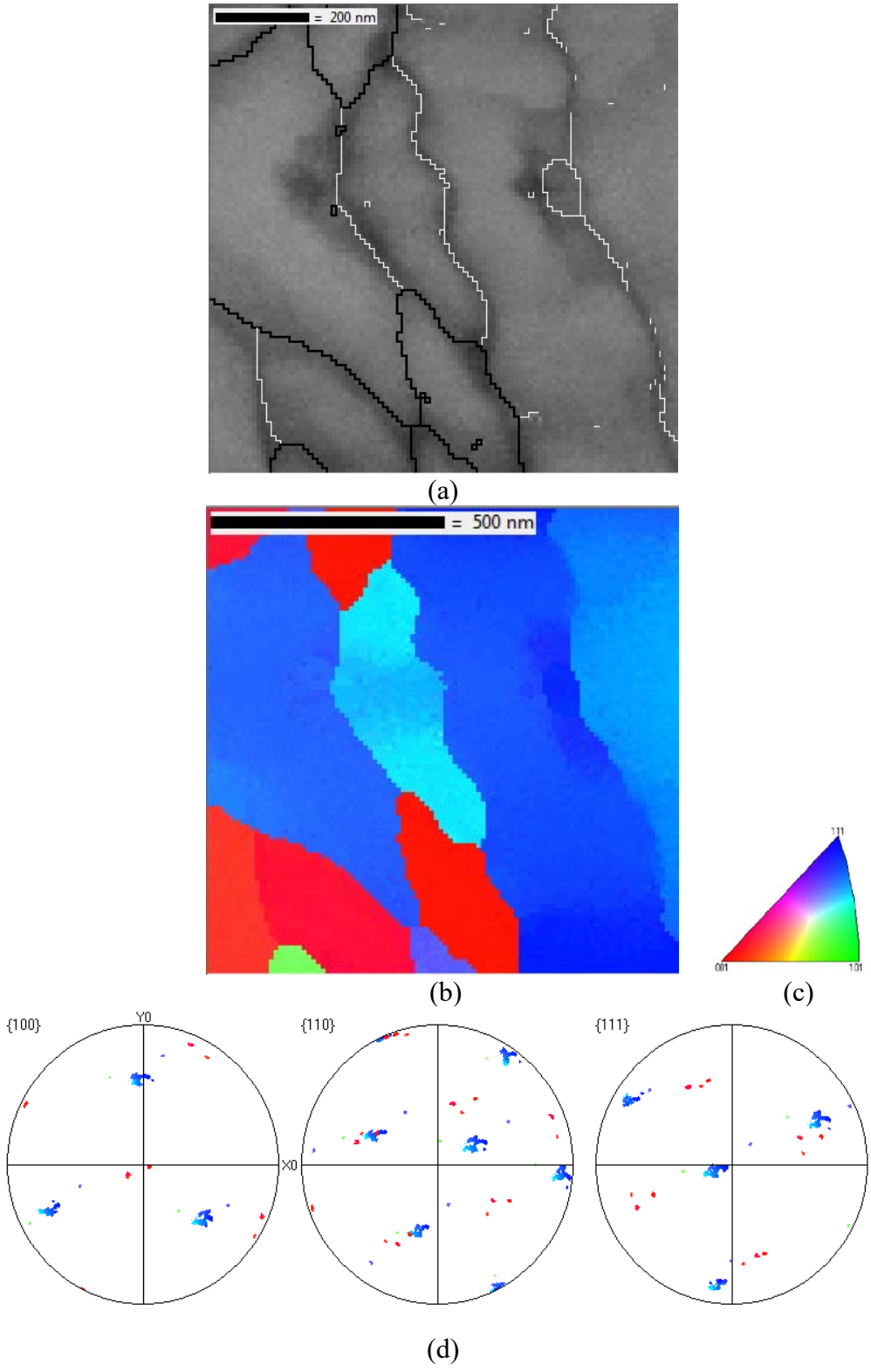

Figure 72. EBSD band contrast image (a) showing grain boundaries for 100 hr high deformation region LAGB (<2.5°) white lines and HAGBs (<15°) black lines. Orthogonal IPF map Z (b) for 100 hr high deformation region. IPF legend (c). Note: 200 or 500 nm scale bar is presented in the image. Pole figure map (d) of {100}, {110}, and {111}.

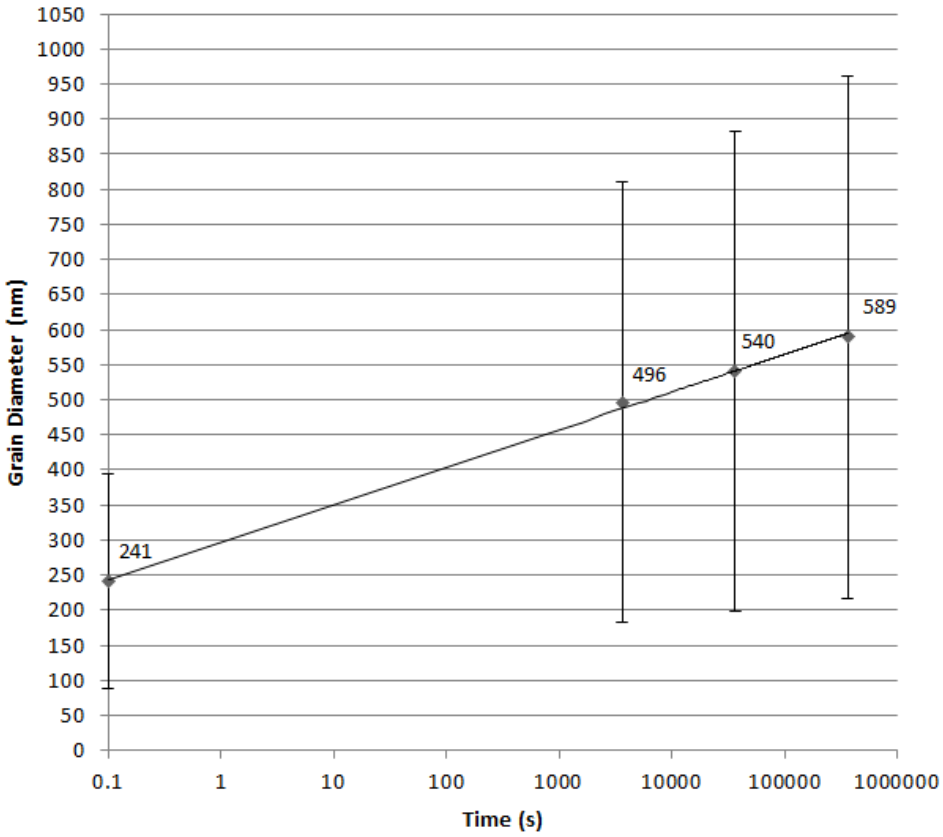

Figure 73. The grain growth for high deformation region from AR to 100 hr at 200°C, the large error bars are addressed in the text.

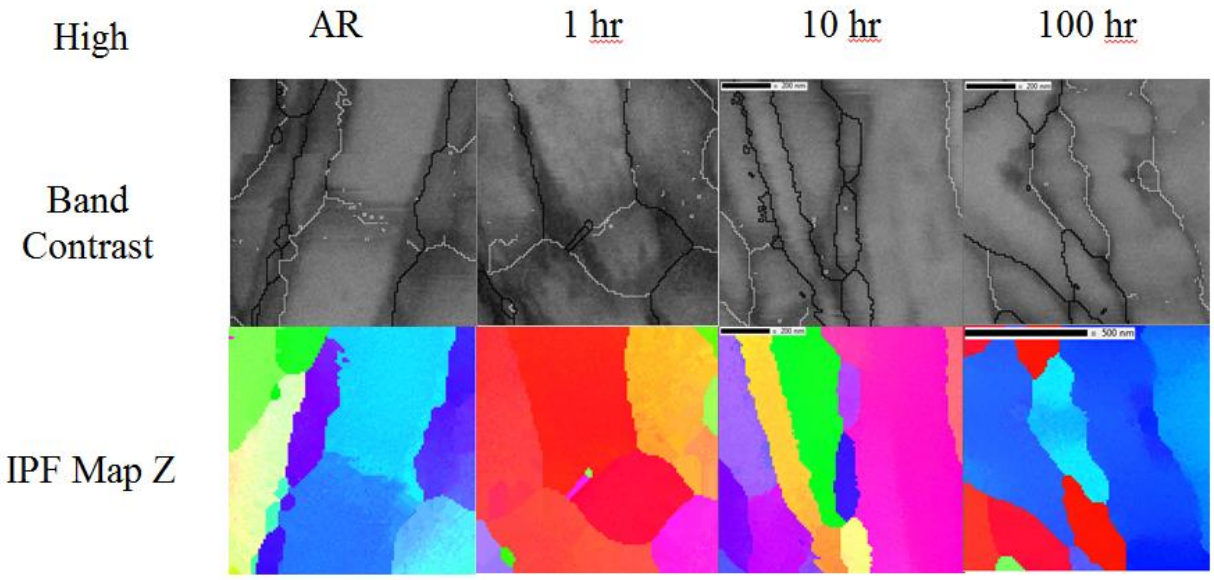

Figure 74. Overall EBSD images of high deformation regions AR, 1 hr, 10 hr, and 100 hr.

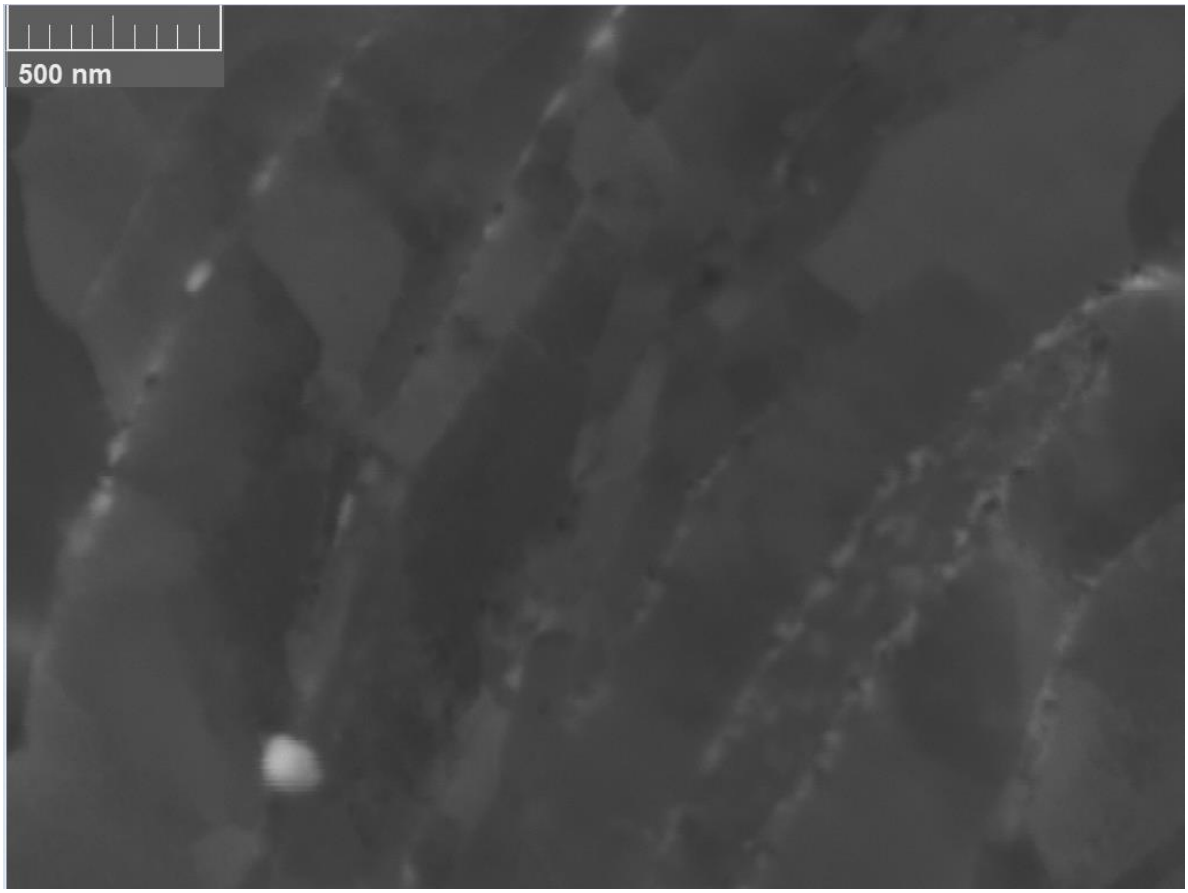

Figure 75. SEM Micrograph taken in BSE mode of a high deformation AR region after ion milling.

4.6 Microhardness Data

The following results are a qualitative microhardness comparison of the CS samples for AR, 1 hr, 10 hr, and 100 hr. These results include a 5x5 array of evenly spaced indents. The location of the array was randomly chosen to obtain a random sample of hardness values across various microstructural regions in the CS deposit. The results include BSE and Vickers Hardness results showing low, medium, and high deformation regions. BSE mode images were taken of the overalls shown in Figures 208 to 211. Results of Vickers microhardness data can be seen in Figure 77 for samples AR, 1hr, 10 hr, and 100 hr. The results of correlative images by BSE mode for the different deformation regions low, medium, and high can be seen in Figure 78 to Figure 89.

Figure 77 shows the array of 25 indents taken from the AR 1 hr, 10 hr, and 100 hr samples, respectively. A linear profile of hardness values from each array was created and placed on the same graph to compare the hardness values across different sample conditions. An indent from the lowest, middle, and highest hardness values were imaged in BSE mode to assess the microstructural dependence of the hardness value to the different deformation regions for each sample.

The lower hardness value correlated with indents in the predominantly low deformation regions. The middle hardness value correlated with predominantly medium deformation regions. The higher hardness values correlated with regions of high deformation. It is important to note that these hardness indents each encompass various areal fractions of low, medium, and high deformation regions, but there is obvious and strong correlation to the hardness value and the dominance of one particular type of deformation. More importantly, it was observed as the annealing time increased the hardness values across the entire array of hardness values decreased in each region show in Figure 68.

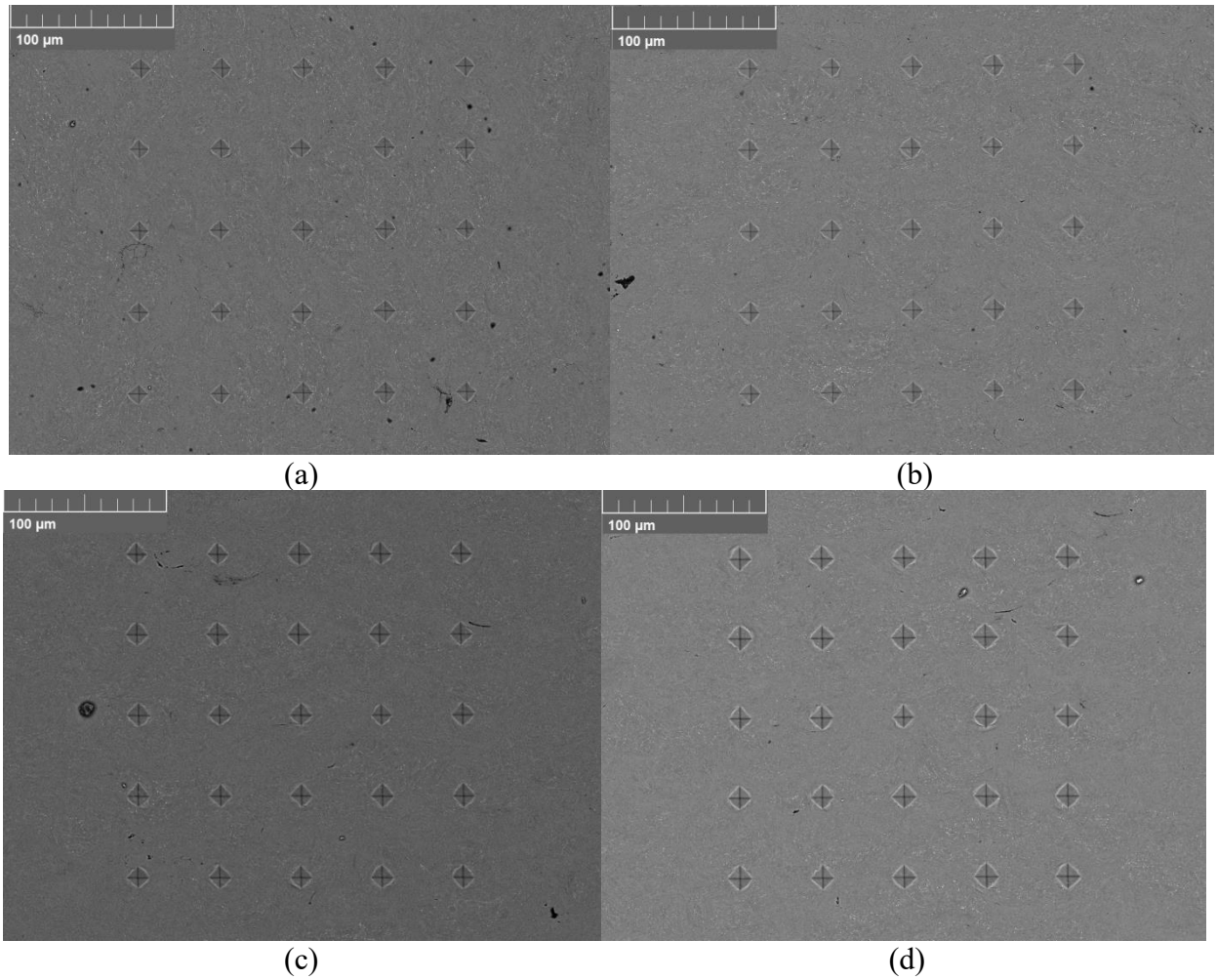

Figure 76. SEM micrograph taken in BSE Mode of CS samples for Overall 25 Microhardness Indents for AR (a), 1 hr (b), 10 hr (c), and 100 hr (d).

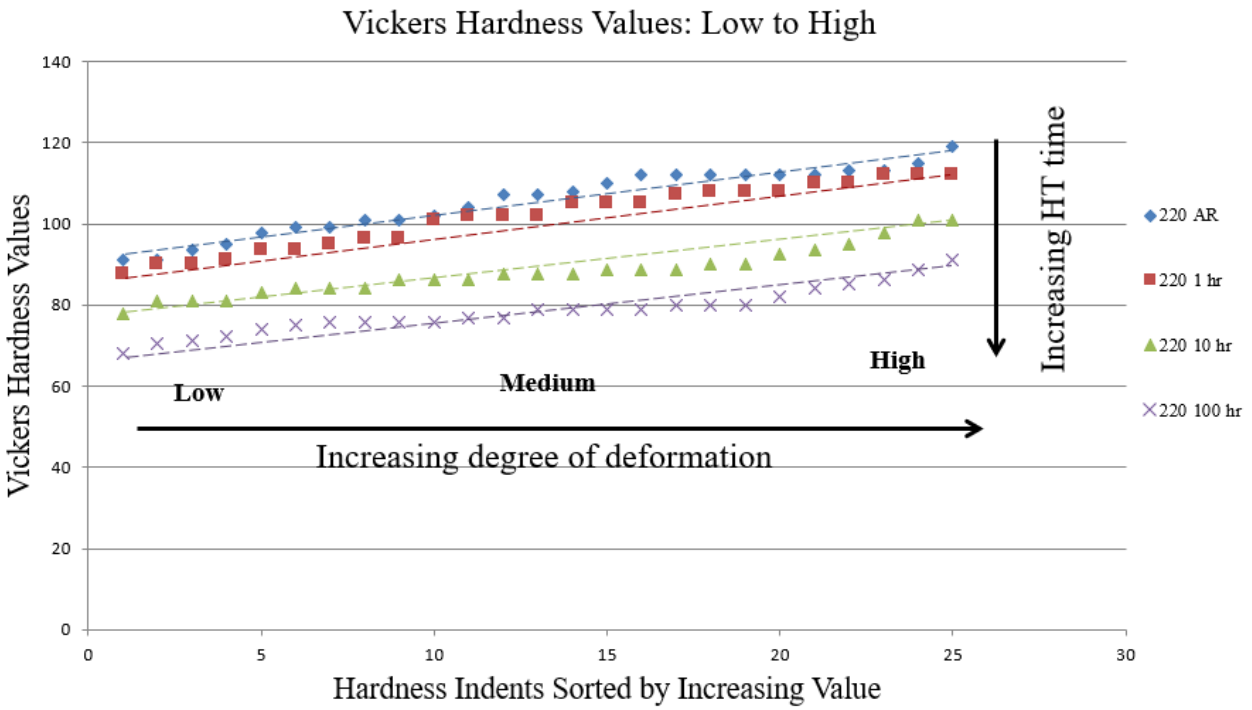

Figure 77. HV values: sorted by increasing values for AR, 1 hr, 10 hr, and 100 hr CS samples. The dashed lines are to show the difference in microhardness between each sample.

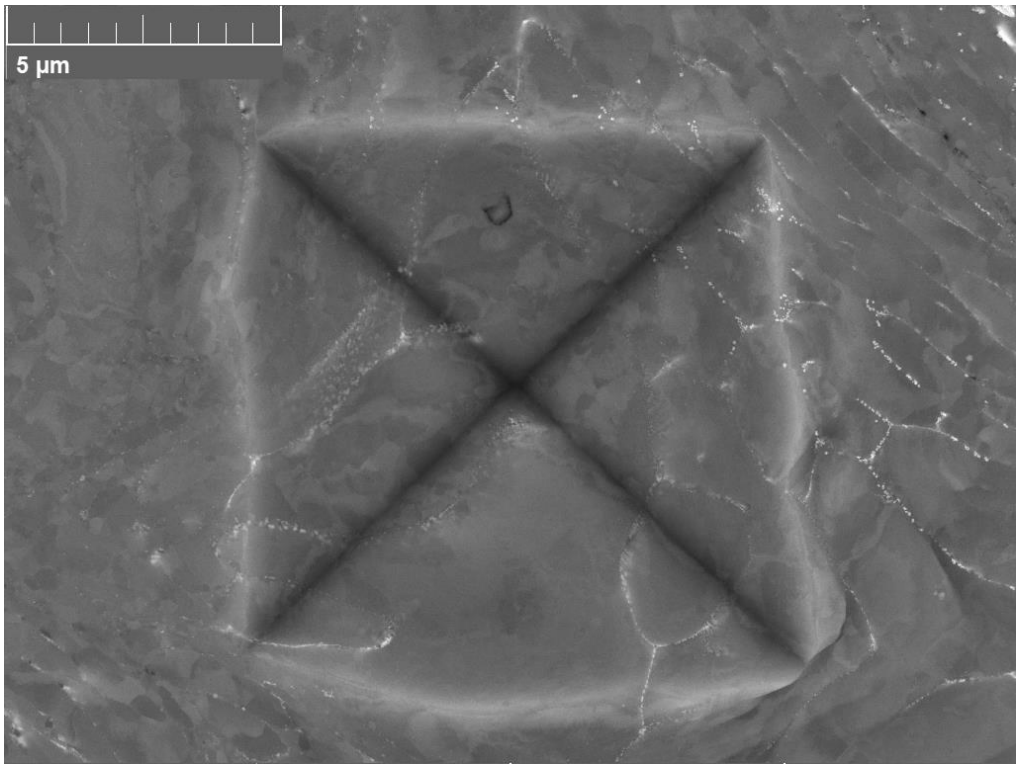

Figure 78. SEM micrograph taken in BSE mode of AR low deformation region indent. The measured microhardness value was 99.2.

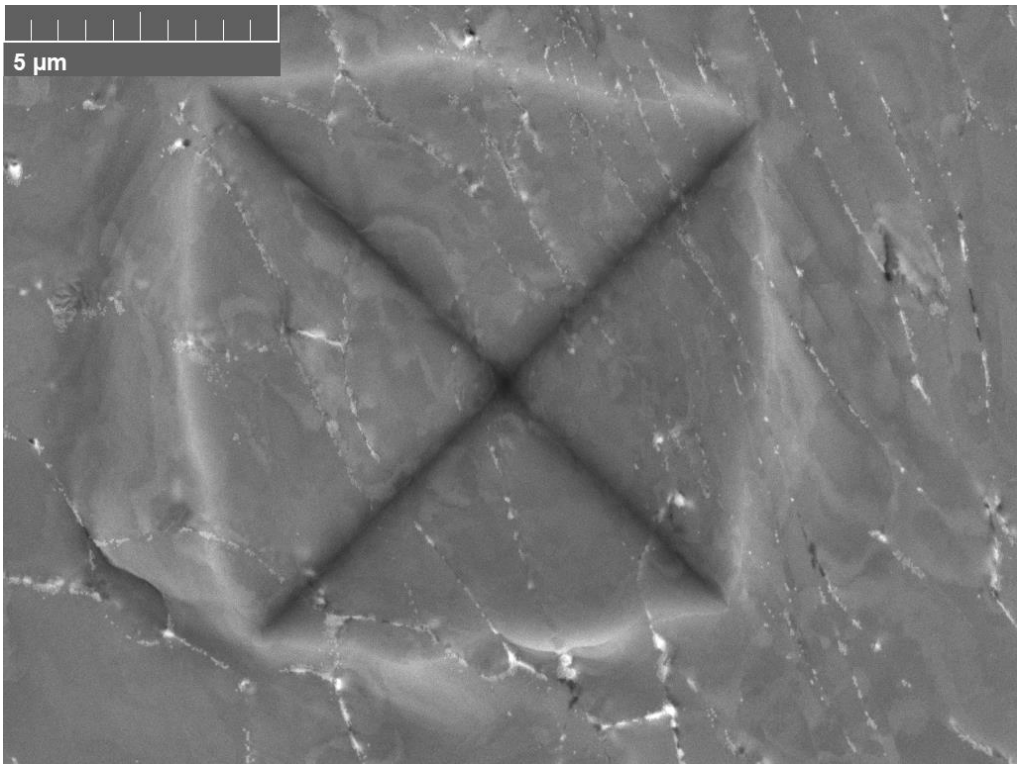

Figure 79. SEM micrograph taken in BSE mode of 1 hr low deformation region indent. The measured microhardness value was 93.7.

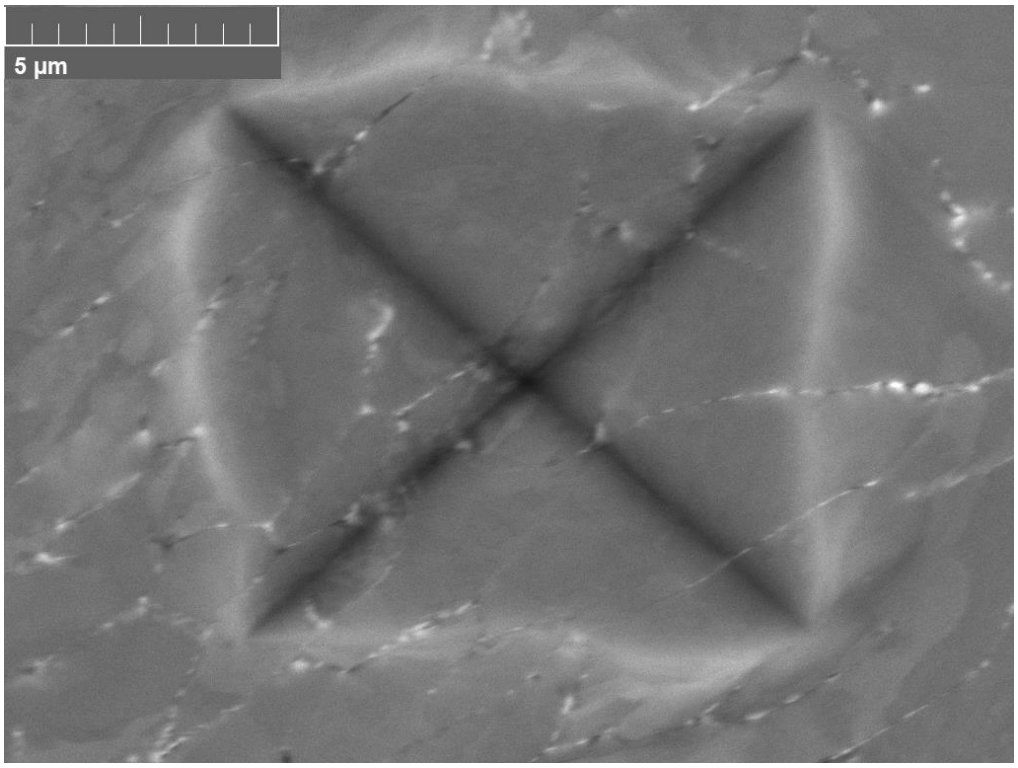

Figure 80. SEM micrograph taken in BSE mode of 10 hr low deformation region indent. The measured microhardness value was 80.8.

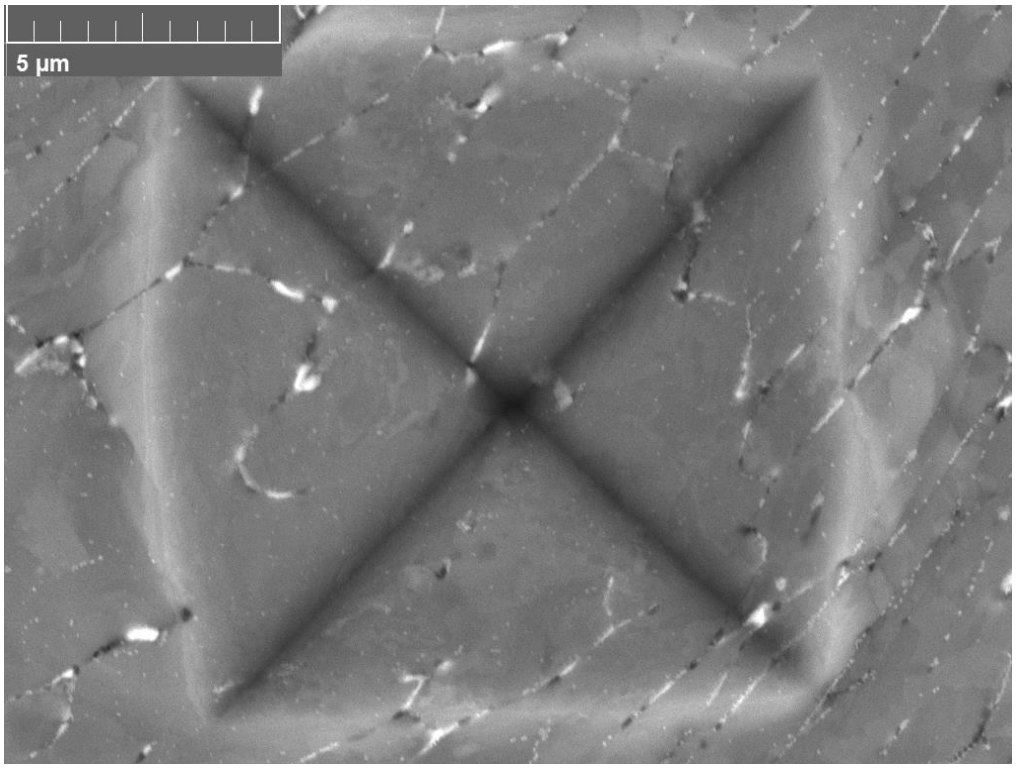

Figure 81. SEM micrograph taken in BSE mode of 100 hr low deformation region indent. The measured microhardness value was 67.9.

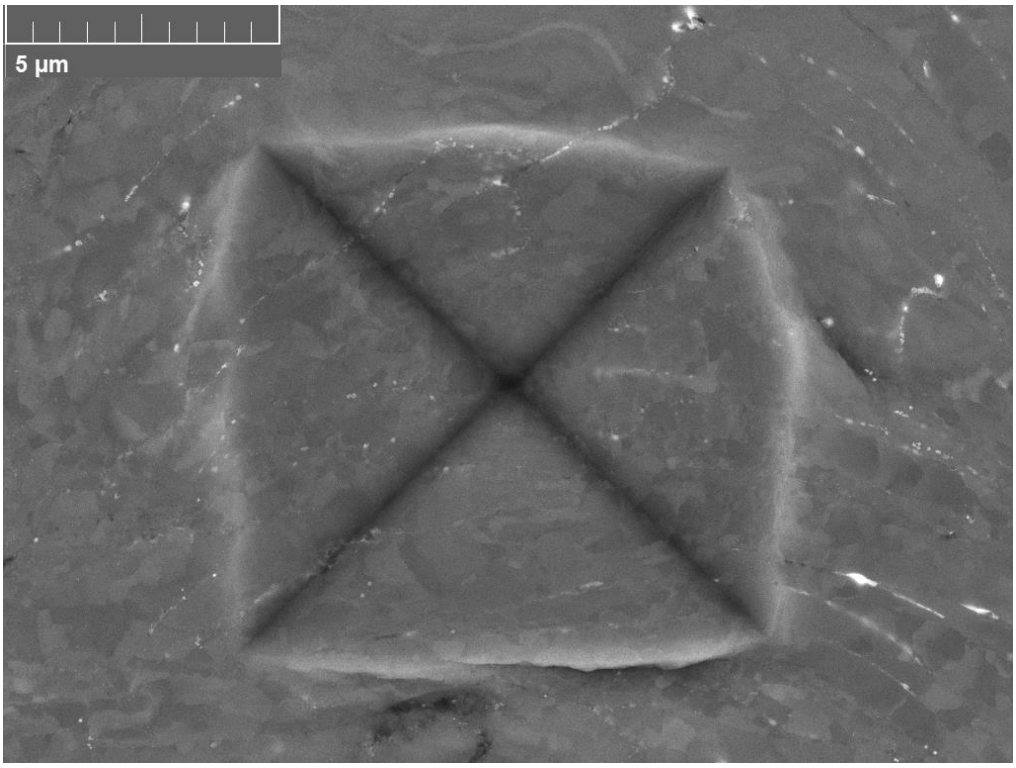

Figure 82. SEM micrograph taken in BSE mode of AR medium deformation region indent. The measured microhardness value was 107.

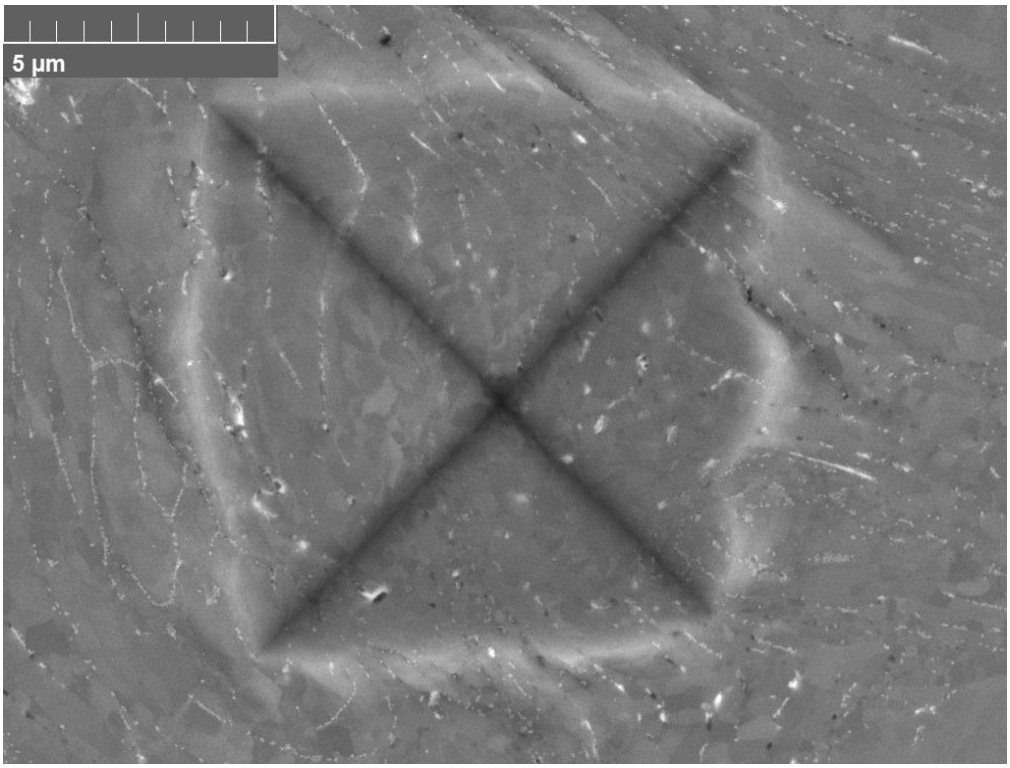

Figure 83. SEM micrograph taken in BSE mode of 1 hr medium deformation region indent. The measured microhardness value was 101.

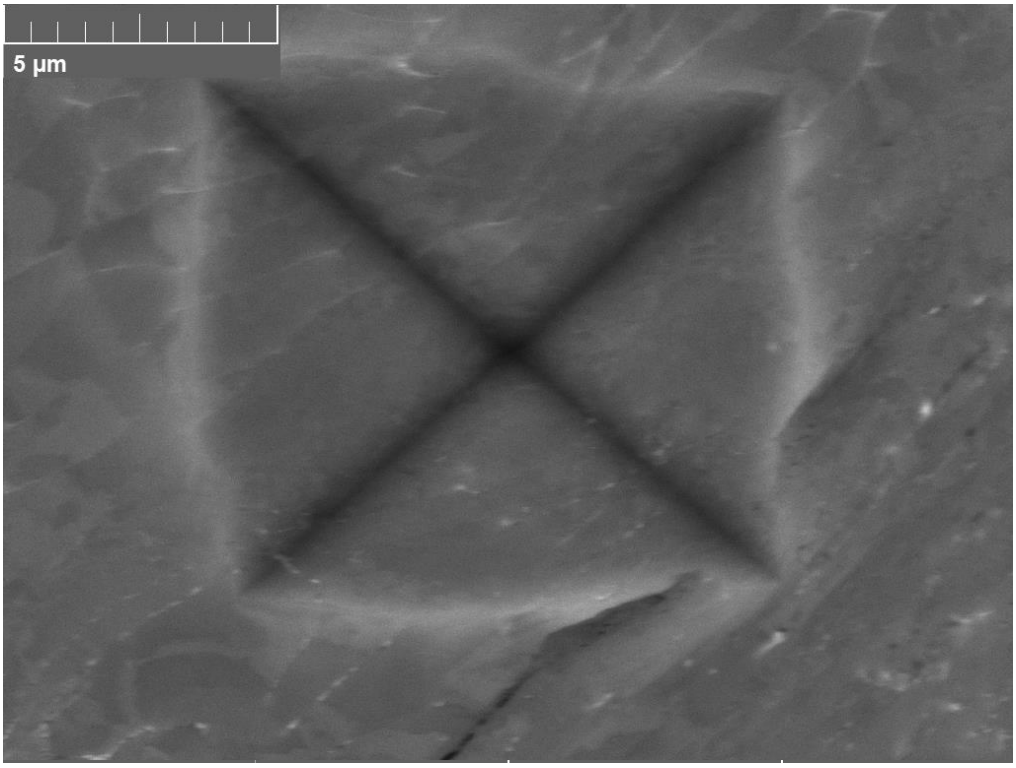

Figure 84. SEM micrograph taken in BSE mode of 10 hr medium deformation region indent. The measured microhardness value was 88.7.

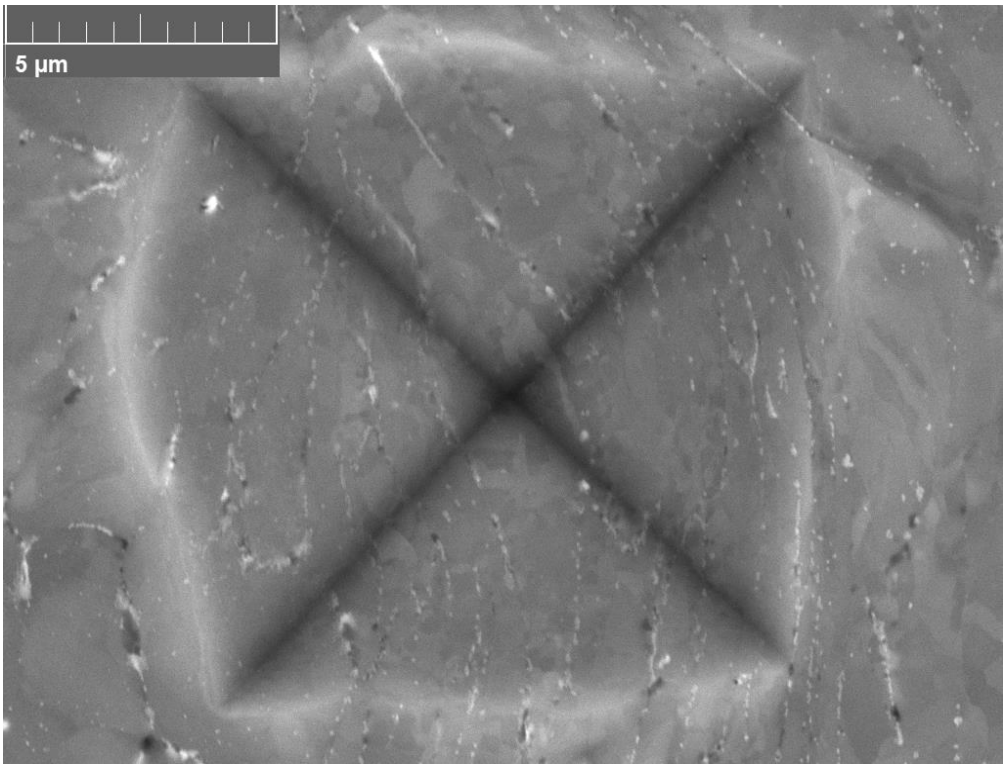

Figure 85. SEM micrograph taken in BSE mode of 100 hr medium deformation region indent. The measured microhardness value was 74.9.

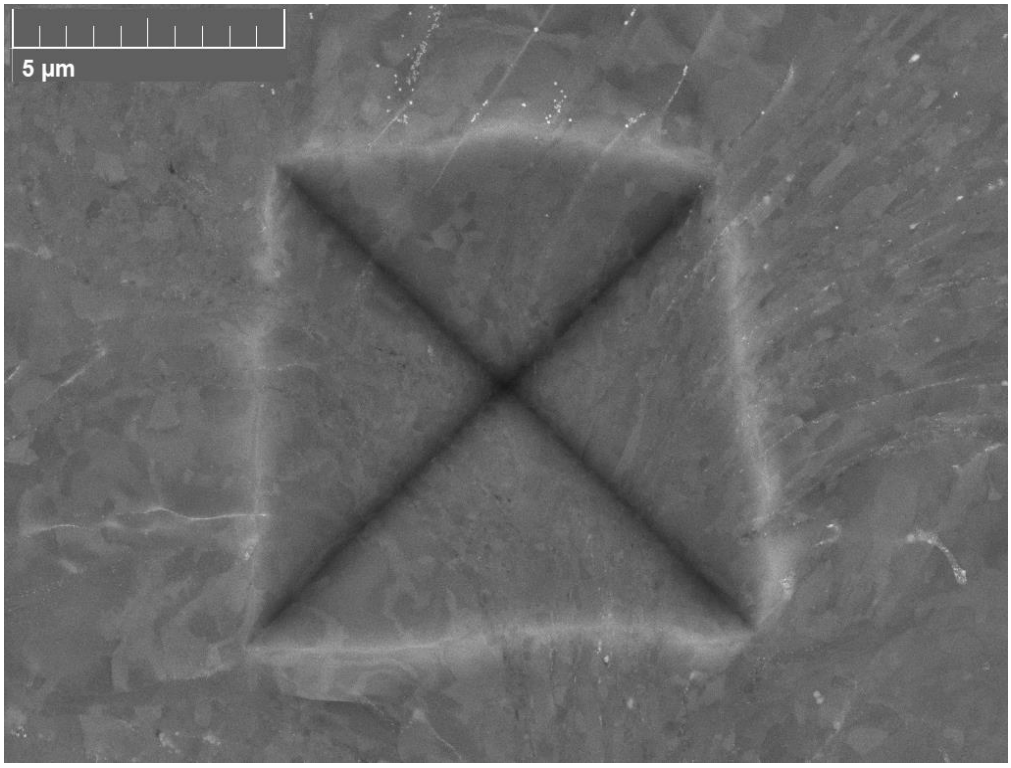

Figure 86. SEM micrograph taken in BSE mode of AR high deformation region indent. The measured microhardness value was 119.

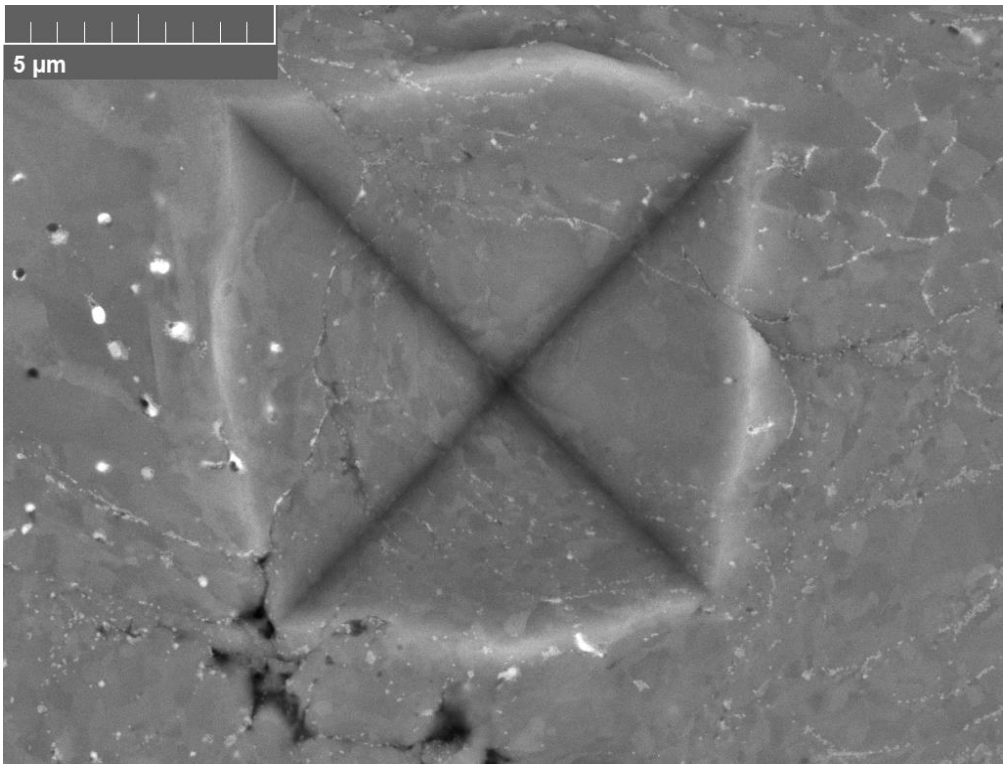

Figure 87. SEM micrograph taken in BSE mode of 1 hr high deformation region indent. The measured microhardness value was 112.

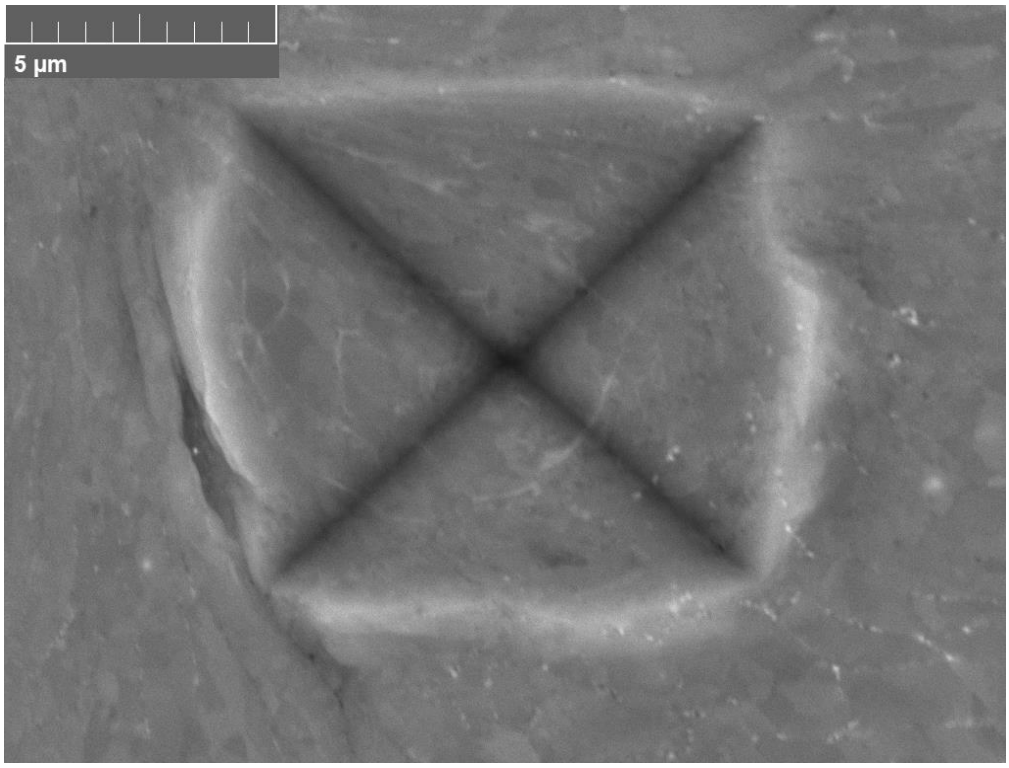

Figure 88. SEM micrograph taken in BSE mode of 10 hr high deformation region indent. The measured microhardness value was 101.

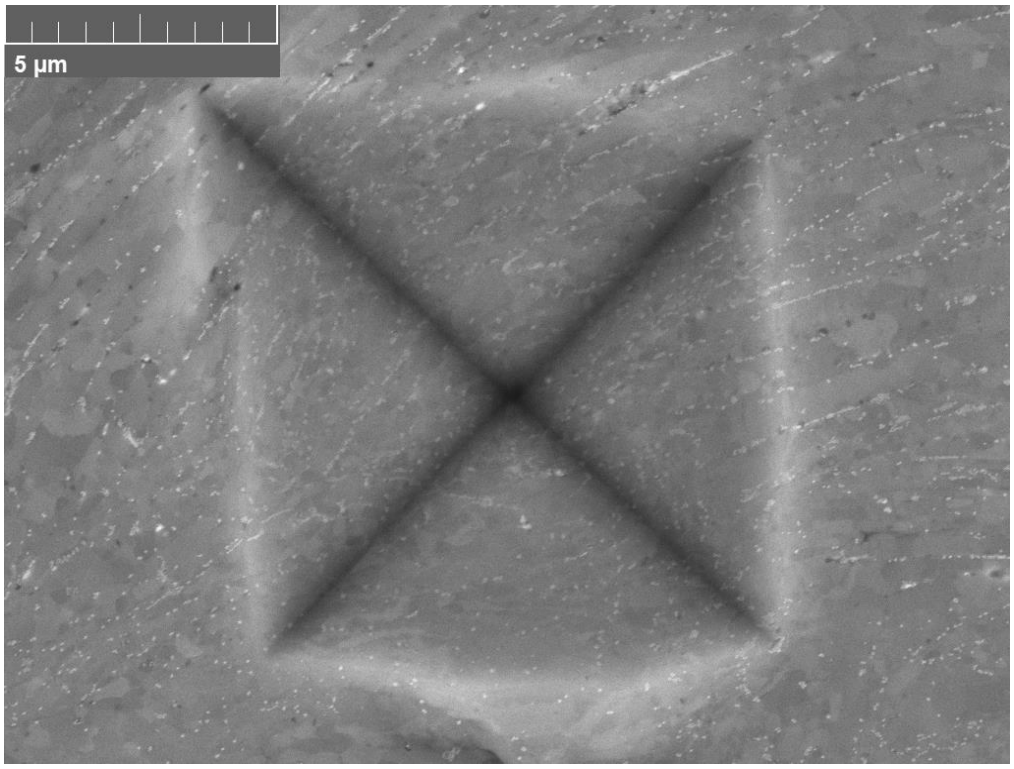

Figure 89. SEM micrograph taken in BSE mode of 100 hr high deformation region indent. The measured microhardness value was 91.1.

Chapter 5: Conclusions and Future Work

The purpose of this project was to characterize the annealing response of the 6061 CS sample. The cross section of CS Al 6061 microstructural images and EBSD provided quantitative and qualitative information on the grain size and orientation of the CS microstructure. The three different deformation regions (low, medium, and high) were characterized with respect to grain size, deformation, crystallographic orientation, and microhardness.

5.1 Conclusions

The EBSD detector was able to recognize approximately 80 to 90 percent of the low, medium and high deformation region in the AR CS conditions. Despite the difficulties in obtaining EBSD data from extremely fine grains, highly deformed aluminum, the different regions of typical cold sprayed microstructures were almost fully characterized by the Oxford Nordlys Nano EBSD system. Eliminations of the effects of hydrocarbons was achieved by cleaning the chamber with a plasma cleaner. Drifting was minimized, improving the ability to maintain consistency in mapping. Through careful sample preparation, elimination of hydrocarbons and optimization of the SEM parameters, EBSD revealed that the high deformation regions in the AR state were comprised of recrystallized grains with 30 to 40 nm diameter, which represents an astounding, 99% reduction diameter.

The low deformation regions showed that the average grain diameter was approximately 2 μm to 3 μm across all sample conditions, which was comparable to the original starting grain size of the powder. Low deformation regions did not exhibit any change in grain size through the annealing process, although evidence of recovery and recrystallization were observed. The

orientation of the grains also showed random distribution similar to the powder that was used for the CS samples and maintained random orientation throughout the duration of the heat treatment. The Mg_2Si particles in the low deformation regions appear to pin grain boundary and prevent grain boundary migration.

The medium deformation regions showed that the average grain diameter was approximately half that of the grains in the low deformation regions and have a typical diameter of 1 to 2 μm. These grains also typically exhibit random orientation. The annealing response for the medium deformation region showed that there was no significant change in grain size between AR to 100 hrs. When annealed, the medium deformation region showed evidence of recovery and partial recrystallization of the grains. No grain growth occurred within the medium deformation region. The Mg_2Si particles in the medium deformation regions appear to pin grain boundary and prevent grain boundary migration.

The low and medium deformation regions would undergo recrystallization, although a small fraction showed signs of complete recrystallization. The recrystallization is shown within the low and medium deformation regions from going from an extreme “tie-dye” deformation within grains to a singular orientation. The grain orientation of the low and medium regions was similar to the powder having random mainly random orientations. There was not a large enough sampling of grains within the regions per annealing state to make a conclusive statement about if there is texture. The results tend to lead that there is no texture within the regions.

The high deformation regions exhibited increasing average grain diameter from the as-received state to the 100 hrs, with typical grain diameter increasing by 244 percent. The AR and 1 hr sample have a random orientation, while the 100 hr sample started to exhibit common

orientations. It was concluded that high deformation region has already undergone recrystallization, likely dynamically, and experience significant grain growth occurred from the 100 hour heat treatment.

The high deformation regions showed to have undergone dynamic recrystallization, because there is deformation within grains. This agrees with the study done by Zou et al. that the ultrafine grains were created by dynamic recrystallization was produced by subgrain rotation and lattice distortion. The rapid grain growth observed from as-received to 1 hr showed that both the surface energy and excess strain as driving force for grain growth. The Mg_2Si particles are scattered randomly within the high deformation regions, and not along clear boundary lines, and therefore, do not appear to inhibit grain growth as it does in the low and medium deformation regions.

The microhardness study provided direct correlation between the degree of deformation and grain size with measured hardness. While this result may seem simple, it provides sound correlation with the observed changes in microstructure for all three deformation regions. This study provides a concise overview of the annealing response of the cold spray deposits.

5.2 Future Work

The following is a list of future works that could be completed to understand the microstructure and its response to the thermal treatments more thoroughly. Further EBSD investigation should be conducted to collect a larger sample size for the different deformation regions. With the larger data set, conclusive results of grain size and grain orientation can be collected. This grain orientation data will help to inform the understanding of a conclusive result on texture in the deformed and recrystallized regions of the deposit.

Further investigation of Al using a Focused Ion Beam (FIB) and EBSD detector should be performed. Serial sectioning CS regions with the FIB to create 3D models could help enhance understanding of the deformation mechanisms at play in these materials.

References

1. A. Papyrin, V.K., S. Klinkov, A. Alkhimov, V. Fomin, *Cold Spray Technology*, ed. A. Papyrin. 2007: Eslevier.

2. R. Dykhuizen, M.S., *Gas dynamic principles of cold spray.* Journal of Thermal Spray Technology, 1998: p. 205-212.

3. D.L. Gilmore, R.C.D., R.A. Neiser, T.J. Roemer, M.F. Smith, *Particle velocity and deposition efficiency in the cold spray process.* Journal of Thermal Spray Technology, 1999. **8**(4): p. 576-582.

4. Wen-Ya Li, C.-J.L., Hanlin Liao, *Significant influence of particle surface oxidation on deposition efficiency, interface microstructure and adhesive strength of cold-sprayed copper coatings.* Applied Surface Science, 2010: p. 4953-4958.

5. T. Stoltenhoff, H.K.a.H.J.R., *An Analysis of the Cold Spray Process and Its Coatings.* Journal of Thermal Spray Technology, 2002. **11**(4): p. 542-550.

6. T. Klassen, F.G., T. Schmidt, J.-O. Kliemann, K. Onizawa, K.-R. Donner, H. Gutzmann, K. Binder, H. Kreye, *Basic principles and application potentials of cold gas spraying.* Mat.-wiss. u.Werkstofftech, 2010. **41**(7): p. 575-584.

7. T. Schmidt, F.G., H. Assadi, H. Richter, T. Stoltenhoff, H. Kreye, T. Klassen, *From Particle Acceleration to Impact and Bonding in Cold Spraying.* Journal of Thermal Spray Technology, 2009. **18**(5-6): p. 794-808.

8. F. Gartner, T.S., T. Stollenhoff, H. Kreye, *Recent developments and potential applications of cold spraying.* Advanced Materials & Processes, 2006. **8**(7): p. 611-618.

9. E. Sansoucy, G.K., A.L. Moran, B. Jodoin *Mechanical Characteristics of Al-Co-Ce Coatings Produced by the Cold Spray Process.* Journal of Thermal Spray Technology, 2007. **16**(5-6): p. 651-660.

10. B. Jodoin, L.A., E. Sansoucy, A Zuniga, P. Richer, E.J. Lavernia, *Effect of particle size, morphology and hardness on cold gas dynamic sprayed alluminum alloy coatings.* Surface Coatings and Technology, 2006. **201**: p. 3422-3429.

11. R. McCune, W.D., O. Popoola, E. Cartwright, *Characterization of Copper Layers Produced by Cold Gas-Dynamic Spraying.* Journal of Thermal Spray Technology, 2000. **9**(1): p. 73-82.

12. X. Luo, Y.L., C. Li, *A comparison of cold spray deposition behavior between gas atomized and dendritic porous electrolytic Ni powders under the same spray conditions.* Materials Letters, 2016. **163**: p. 58-60.

13. W. Choi, L.L., V. Luzin, R. Neiser, T. Gnaupel-Herold, H.J. Prask, S. Sampath, A. Gouldstone, *Integrated characterization of cold sprayed aluminum coatings.* Acta Materialia, 2007. **55**: p. 857-866.

14. D. Goldbaum, J., Ajaja , R.R. Chromik, W. Wong , S. Yue , E. Irissou, J. Legoux, *Mechanical behavior of Ti cold spray coatings determined by a multi-scale indentation method.* Materials Science & Engineering A, 2011. **530**: p. 253-265.

15. Victor K. Champagne, D.J.H., Surya P.G. Dinavahi, and Pillip F. Leyman, *Theoretical and Experimental Particle Velocity in Cold Spray.* Journal of Thermal Spray Technology, 2010: p. 425-431.

16. J. Vlcek, L.G., H. Huber, and E. Lugscheider, *A Systematic Approach to Material Eligibility for the Cold-Spray Process.* Journal of Thermal Spray Technology, 2005. **14**(1): p. 125-133.

17. Wilson Wong, E.I., Anatoly N. Ryabinin, Jean-Gabriel Legoux, and Stephen Yue, *Influence of Helium and Nitrogen Gases on the Properties of Cold Gas Dynamic Sprayed Pure Titanium Coatings* Journal of Thermal Spray Technology, 2011. **20**((1-2)): p. 213-226.

18. Villafuerte, J., *Cold Spray: A New Technology.* Welding Journal, 2005. **84**(5): p. 24-29.

19. F. Gartner, T.S., T. Schmidt, H. Kreye *The cold spray process and its potential for industrial applications.* Journal of Thermal Spray Technology, 2006. **15**(2): p. 223-232.

20. Karthikeyan, J., *Cold spray technology.* Advanced Materials & Processes, 2005: p. 33-35.

21. A. Sova, S.G., A. Okunkova, I. Smurov, *Potential of cold gas dynamic spray as additive manufacturing technology.* Springer, 2013: p. 2269-2278.

22. Champagne, V., *The repair of magnesium rotorcraft components by cold spray.* Journal of Failure Analysis Prevention, 2008. **8**: p. 164-175.

23. Helfritch, V.K.C.D.J., *Mainstreaming cold spray push for applications.* Surface Engineering, 2014: p. 396 - 403.

24. Xuemei Wang, F.F., Michael A. Klecka, Matthew D. Mordasky,, *Characterization and modeling of the bonding process in cold spray.* ScienceDirect, 2015: p. 149-162.

25. A.M. Birt, V.C., R.D. Sisson Jr., D. Apelian, *Microstructural analysis of Ti–6Al–4V powder for cold gas dynamic spray applications.* Advanced Powder Technology, 2015: p. 1335 - 1347.

26. K. Ogawa, K.I., K. Ichimura, Y. Ichikawa, S. Ohno, and N. Onda, *Characterization of Low-Pressure Cold-Sprayed Aluminum Coatings.* Journal of Thermal Spray Technology, 2008. **17**(5-6): p. 728-735.

27. T. Schmidt, F.G., H. Assadi, H. Kreye, *Development of a generalized parameter window for cold spray deposition.* Acta Materialia, 2006. **54**: p. 729-742.

28. T.S. Price, P.H.S., and D.G. McCartney *Effect of Cold Spray Depostion of a Titanium Coating on Fatigue Behavior of a Titanium Alloy.* Journal of Thermal Spray Technology, 2006. **15**(4): p. 507-512.

29. H. Assadi, F.G., T. Stoltenhoff, H. Kreye, *Bonding mechanism in cold gas spraying.* Acta Materialia, 2003. **51**: p. 4379-4394.

30. C. Chen, Y.X., S. Yin, M. Planche, S. Deng, R. Lupoi, H. Liao, *Evaluation of the interfacial bonding between particles and substrate in angular cold spray.* Materials Letters, 2016. **173**: p. 76-79.

31. T. Stoltenhoff, C.B., F. Gartner, H. Kreye, *Microstructures and key properties of cold-sprayed and thermally sprayed copper coatings.* Surface Coatings and Technology, 2006. **200**: p. 4947-4960.

32. C. Borchers, F.G., T. Stoltenhoff, H. Assadi, H. Kreye, *Microstructural and macroscopic properties of cold sprayed copper coatings.* Journal of Applied Physics, 2003. **93**(12): p. 10064-10070.

33. C. Borchers, F.G., T. Stoltenhoff, H. Kreye, *Microstructural bonding features of cold sprayed face centered cubic metals.* Journal of Applied Physics, 2004. **96**(8): p. 4288-4292.

34. D. Goldbaum, R.R.C., S. Yue, E. Irissou, and J. Legoux, *Mechanical Property Mapping of Cold Sprayed Ti Splats and Coatings.* Journal of Thermal Spray Technology, 2011. **20**(3): p. 486-496.

35. T. Hussain, D.G.M., P.H. Shipway, and D. Zhang, *Bonding Mechanisms in Cold Spraying:The Contributions of Metallurgical and Mechanical Components.* Journal of Thermal Spray Technology, 2009. **18**(3): p. 364-379.

36. W. Li, X.G., M. Yu, H. Liao, C. Coddet, *Investigation of Impact Behavior of Cold-Sprayed Large Annealed Copper Particles and Characterization of Coatings.* Journal of Thermal Spray Technology, 2011. **20**(1-2): p. 252-259.

37. X. Zhou, X.W., H. Guo, J. Wang, and J. Zhang, *Deposition behavior of multi-particle impact in cold spraying process.* International Journal of Minerals, Metallurgy and Materials, 2010. **17**(5): p. 635-640.

38. N. Kahraman, B.G., *Microstructural and mechanical properties of Cu-Ti plates bonded through explosive welding process.* Journal of Materials Processing Technology, 2005. **169**: p. 67-71.

39. Reza Abbaschian, L.A., and Robert E. Reed-Hill, *Physical Metallurgy Principles*. 2009: Cengage Learning.

40. Yu Zou, W.Q., Eric Irissou, Jean-Gabriel Legoux, Stephen Yue, Jerzy A. Szpunar, *Dynamic recrystallization in the particle/particle interfacial region of cold-sprayed nickel coating: Electron backscatter diffraction characterization.* ELSEVIER, 2009: p. 899-902.

41. Derby, B., *The Dependence of Grain Size on Stress During Dynamic Recrystallizatin.* Acta metallurgica, 1991: p. 955-962.

42. N. Hosseini, M.H.A., F. Karimzadeh, M.H. Enayati, *Structural evolution and grain growth kinetics during isothermal heat treatment of nanostructured Al6061.* Materials Science and Engineering A, 2009: p. 107-111.

43. S. Zahiri, D.F., and M. Jahedi, *Recrystallization of Cold Spray-Fabricated CP Titanium Structures.* Journal of Thermal Spray Technology, 2009. **18**(1): p. 16-22.

44. W. li, X.P.G., C. Verdy, L. Dembinski, H.L. Liao, C. Coddet, *Improvement of microstructure and property of cold-sprayed Cu- 4 at.%Cr-2 at.%Nb alloy by heat treatment.* Scripta Materialia, 2006. **55**: p. 327-330.

45. A.C. Hall, D.J.C., R.A. Neiser, T.J. Roemer, and D.A. Hirschfeld, *The Effect of a Simple Annealing Heat Treatment on the Mechanical Properties of Cold-Sprayed Aluminum.* Journal of Thermal Spray Technology, 2006. **15**(2): p. 233-238.

46. P. Coddet, C.V., C. Coddet, F. Debray, *Mechanical properties of Cu-0.1 Ag Alloys Depostied by Cold Spray with Various Powder Feed Rate and Heat Treatment.* Journal of Thermal Spray Technology, 2015. **24**(1-2): p. 119-125.

47. C. Borchers, F.G., T. Stoltenhoff, H. Kreye, *Formation of persistent dislocation loops by ultra-high strain-rate deformation during cold spraying.* Acta Materialia, 2005. **53**: p. 2991-3000.

48. F. Gartner, T.S., J. Voyer, H. Kreye, S. Riekehr, M. Kocak, *Mechanical properties of cold-sprayed and thermally sprayed copper coatings.* Surface Coatings and Technology, 2006. **200**: p. 6770-6782.

49. E. Calla, D.G.M., P.H. Shipway, *Effect of deposition conditions on the properties and annealing behavior of cold-sprayed copper.* Journal of Thermal Spray Technology, 2006. **15**(2): p. 255-262.

50. HUMPHREYS, F.J., *Grain and subgrain characterisation by electron backscatter diffraction.* Journal of Materials Science Letters, 2001: p. 3833-3854.

51. *oxford-instruments*, in *https://www.oxford-instruments.com/products/microanalysis/ebsd*. 2015.

52. M.R. Rokni, C.A.W., G.A. Crawford, *Microstrucutral evolution of 7075 Al gas atomized powder and high-pressure cold sprated depostion.* Surface & Coatings Technology, 2014: p. 254-263.

53. L.N. Brewer, J.F.S., E.S.K. Menon, D.J. Woo, *The connections between powder variability and coating microstructures for cold spray deposition of austenitic stainless steel.* ELSEVIER, 2018: p. 50-60.

54. Bandar AL-Mangour, P.V., Rosaire Mongrain, Eric Irissou, and Stephen Yue, *Effect of heat treatment on the microstructure and mechanical properties of stainless steel 316L coatings produced by cold spray for biomedical applications.* ASM International, 2013: p. 641-652.

55. Yu Zou, D.G., Jerzy A. Szpunar, Stephen Yue, *Microstructure and nanohardness of cold-sprayed coatings: electron backscattered diffraction and nanindentation studies.* ELSEVIER, 2010: p. 395-398.

56. G.S. Dyakonov, E.Z., S. Mironov, I.P. Semoenova, R.Z. Valiev, S.L. Semiatin, *An EBSD ivestigation of ultrafrine-grain titanium for biomedical applications.* Materials Science & Engineering A, 2015: p. 305-310.

57. Morteza Shamanian, H.M., Mehdi Safari, and Jerzy A. Szpunar, *EBSD Study on Grain Boundary and Microtexture Evolutions During Friction Stir Processing of A413 Cast Aluminum Alloy.* ASM International, 2016: p. 2824-2835.

58. CHEN Yong-jun, J.H., Hans J. ROVEN, *Application of EBSD technique to ultrafine grained and nanostructured materials processed by severe plastic deformation: Sample preparation, parameters optimization and analysis.* Transactions of Nonferrous Metals Society of China, 2012: p. 1801-1809.

59. Delphic Chen, J.-C.K., Wen-Tuan Wu, *Effect of microscopic parameters on EBSD spatial resolution.* Ultramicroscopy, 2011: p. 1488-1494.

60. Y.B. Zhang, A.E., F.X. Lin, *A method to correct coordinate distortion in EBSD maps.* Materials Characterization, 2014: p. 158-165.

61. Vivian Tong, J.J., Angus J. Wilkinson, T. Ben Britton, *The effect of pattern overlap on the accuracy of high resolution electron backscatter diffraction measurements.* Ultramicroscopy, 2015: p. 62-73.

62. Humphreys, F.J., *Characterisation of fine-scale microstructures by electron backscatter diffraction (EBSD).* Scripta Materialia, 2004: p. 771-776.

63. P.B. Prangnell, J.R.B., P.J. Apps, *Ultra-fine grain structures in aluminium alloys by severe deformation processing.* Materials Science & Engineering A, 2004: p. 178-185.

64. Dicks, K. *Introduction to EBSD*. 2003.

65. Kaibyshev, A.M.a.R., *Microstructure and Mechanical Properties of an Al-Li-Mg-Sc-Zr Alloy Subjected to ECAP.* Metals, 2016: p. 1-14.

66. K. Balani, T.L., A. Agarwal, J. Karthikeyan, N. Munroe, *Effect of carrier gases on microstructural and electrochemical behavior of cold-sprayed 1100 coatings.* Surface Coatings and Technology, 2004. **195**: p. 272-279.

67. T. Kairet, M.D., F. Campana, J. Janssen, *Influence of the powder size distribution on the microstructure of cold-sprayed copper coatings studied by x-ray diffraction.* Journal of Thermal Spray Technology, 2007. **16**(5-6): p. 610-618.

68. E. Sansoucy, P.M., L. Ajdelsztajn, B. Jodoin, *Properties of SiC-reinforced aluminum alloy coatings produced by the cold gas dynamic spraying process.* Surface Coatings and Technology, 2008: p. 3988-3996.

69. L. Venkatesh, N.M.C., G. Sundararajan, *The Influence of Powder Particle Velocity and Microstructure on the Properties of Cold Sprayed Copper Coatings.* Journal of Thermal Spray Technology, 2011. **20**(5): p. 1009-1021.

70. M. Yandouzi, E.S., L. Ajdelsztajn, B. Jodoin, *WC-based cermet coatings produced by cold gas dynamic and pulsed gas dynamic spraying processes.* Surface Coatings and Technology, 2007. **202**: p. 382-390.

71. Paul D. Eason, J.A.F., Shane C. Kennett, Timothy J. Eden, Karem Tello,, *On the characterization of bulk copper produced by cold gas dynamic spray.* Materials Science and Engineering A, 2011: p. 8174 - 8178.

72. Paul D. Eason, T.J.E., Shane C. Kennett, and Michael J. Kaufman, *A Structure Property Processing Comparison of Cold rolled PM Copper.* Powder Metallurgy & Mining, 2012.

Appendix A – Additional EBSD sites for powder, (low, medium, and high) deformation regions

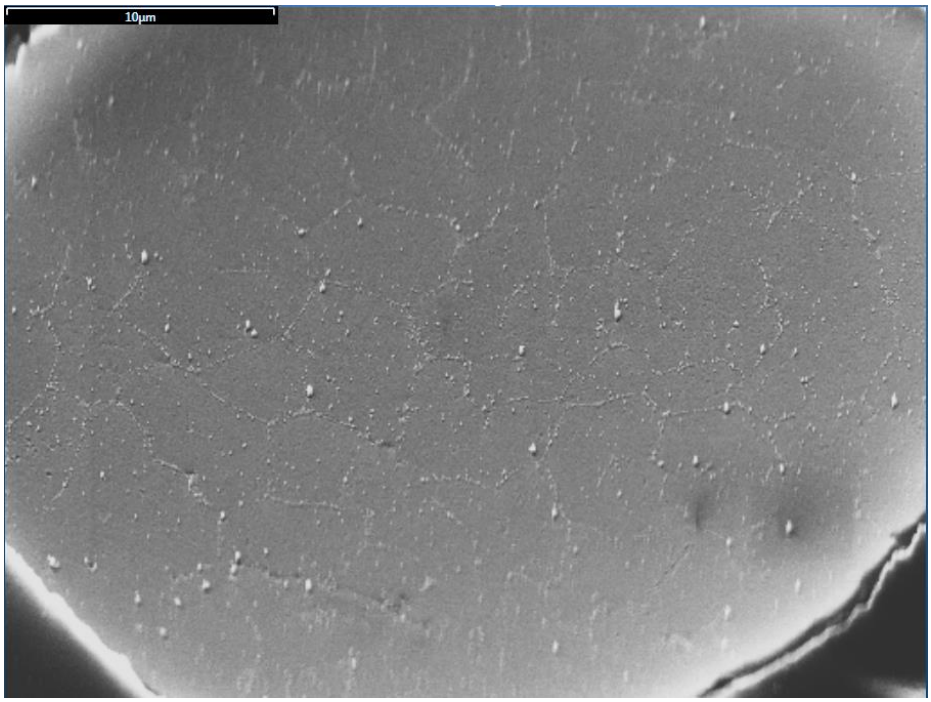

Figure 90. SEM micrograph taken in SE mode of powder site 2. Note a 10 um scale bar is presented in the image.

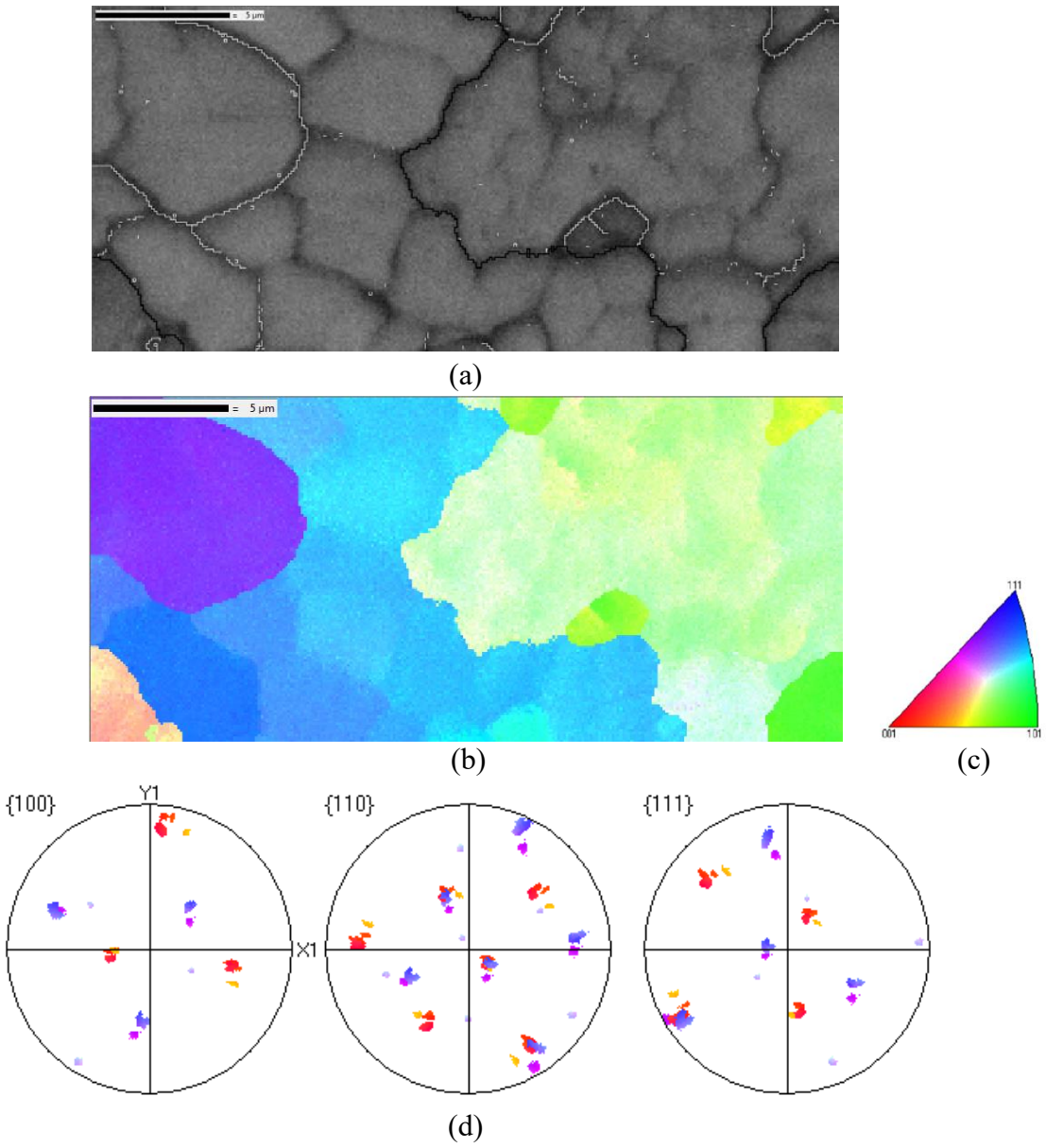

Figure 91. EBSD band contrast image (a) showing grain boundaries from powder cross section site 2 LAGB (<2.5°) white lines and HAGBs (<15°) black lines. Orthogonal IPF map Z (b) for a randomly selected powder cross section site 1. IPF legend (c). Note: 5 µm scale bar is presented in each image. Pole figure map (d) of {100}, {110}, and {111} for site 2.

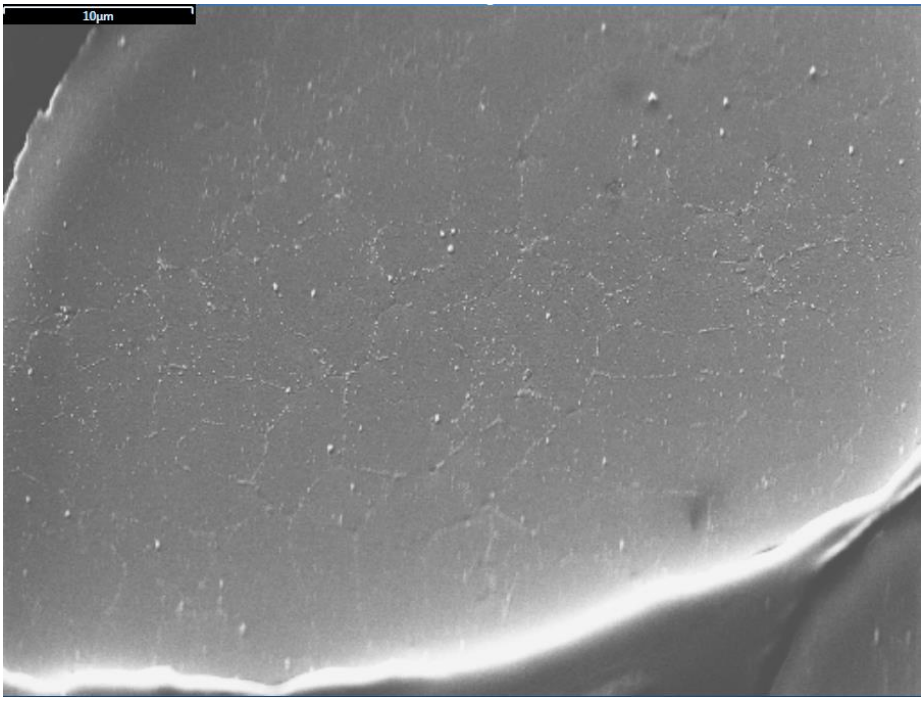

Figure 92. SEM micrograph taken in SE mode of powder site 3. Note a 10 um scale bar is presented in the image.

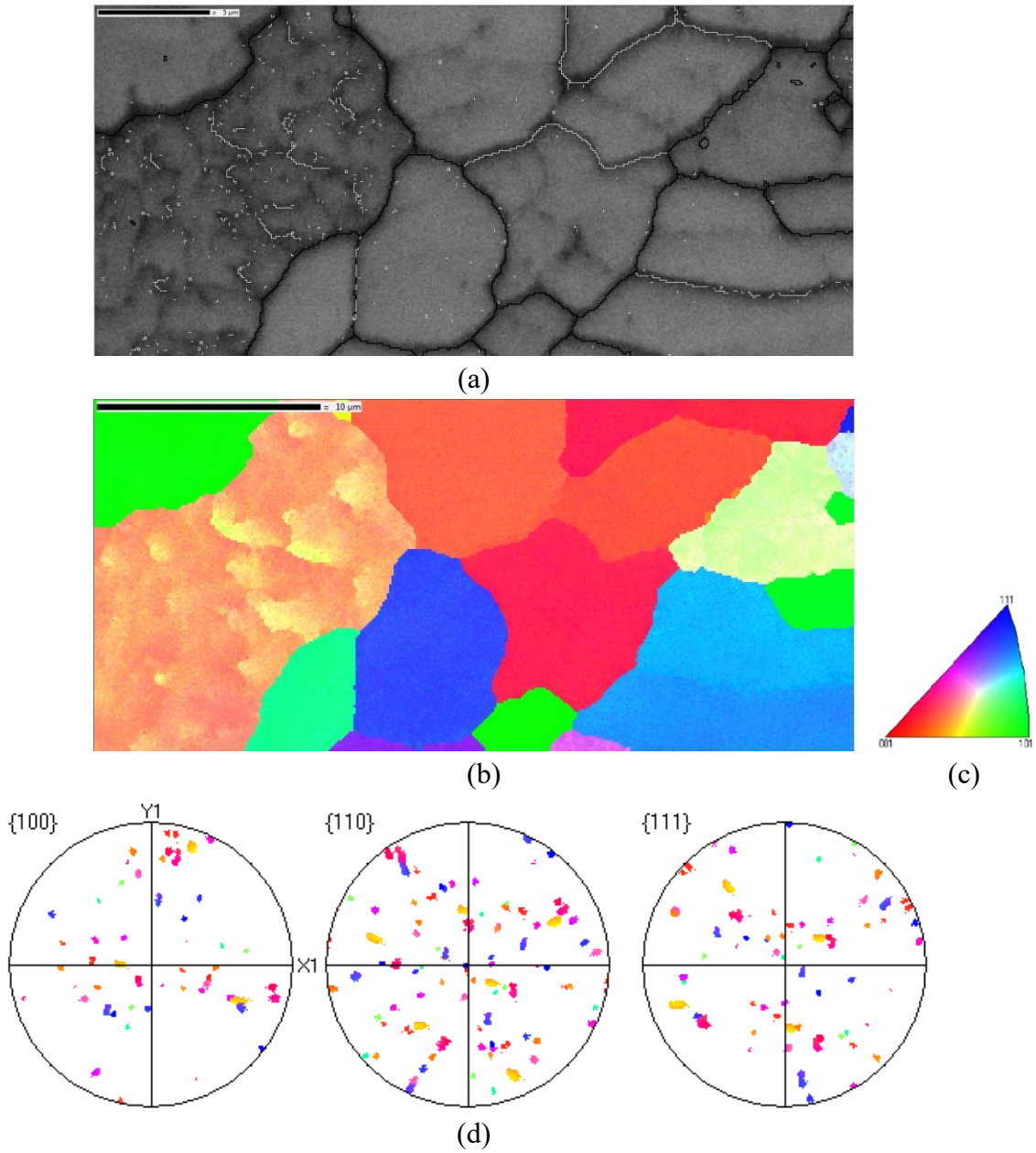

Figure 93. EBSD band contrast image (a) showing grain boundaries from powder cross section site 3 LAGB (<2.5°) white lines and HAGBs (<15°) black lines. Orthogonal IPF map Z (b) for a randomly selected powder cross section site 1. IPF legend (c). Note: 5 and 10 µm scale bar is presented in the image. Pole figure map (d) of {100}, {110}, and {111} for site 3.

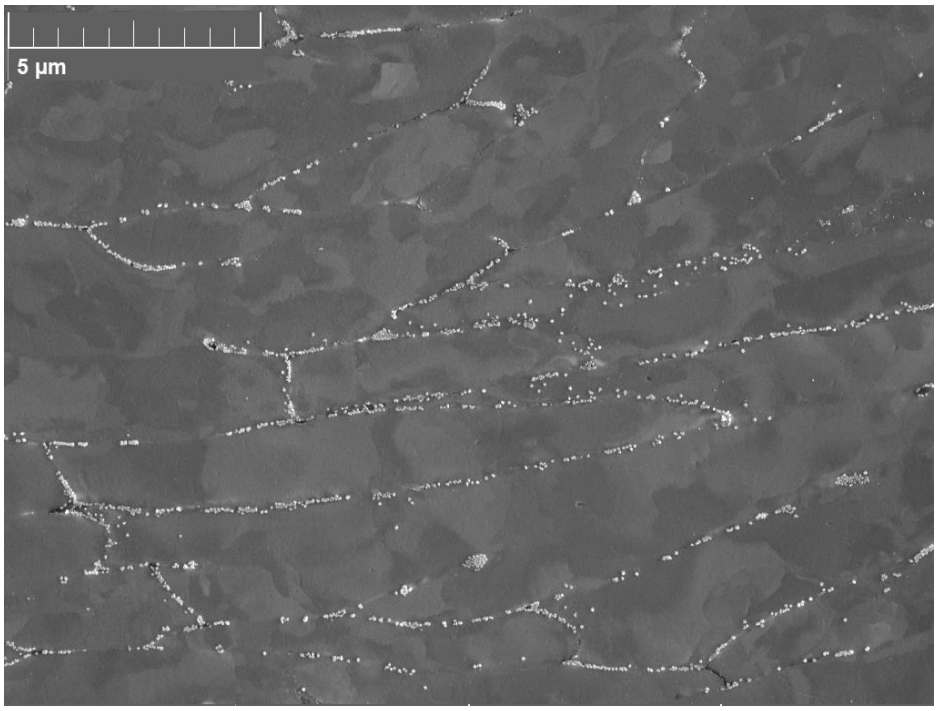

Figure 94. SEM micrograph taken in SE mode of AR Mid deformation site 1.

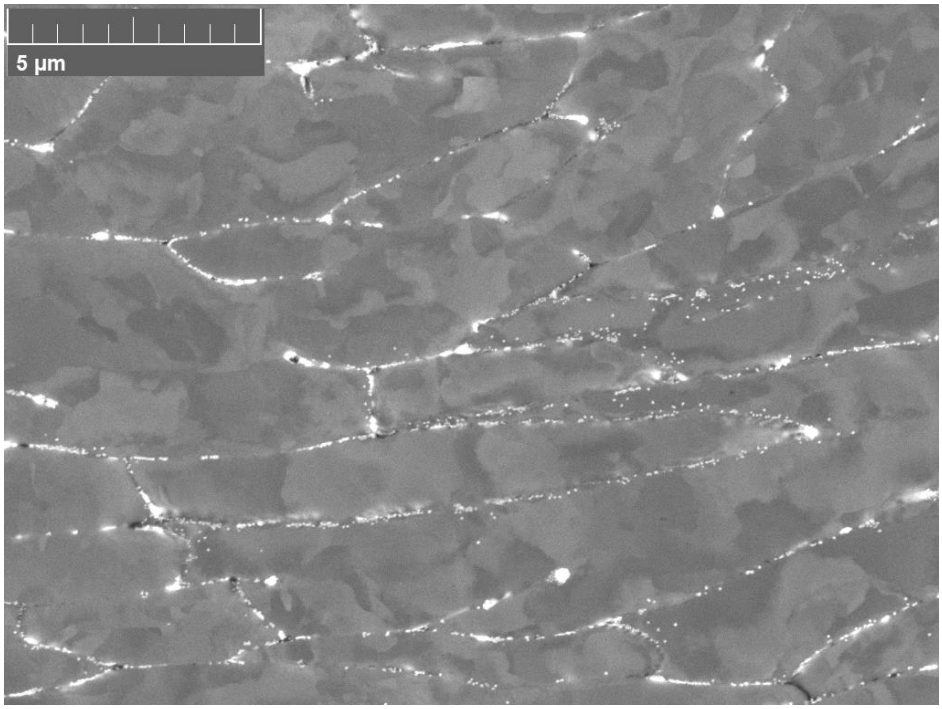

Figure 95. SEM micrograph taken in BSE mode of AR medium deformation region site 1.

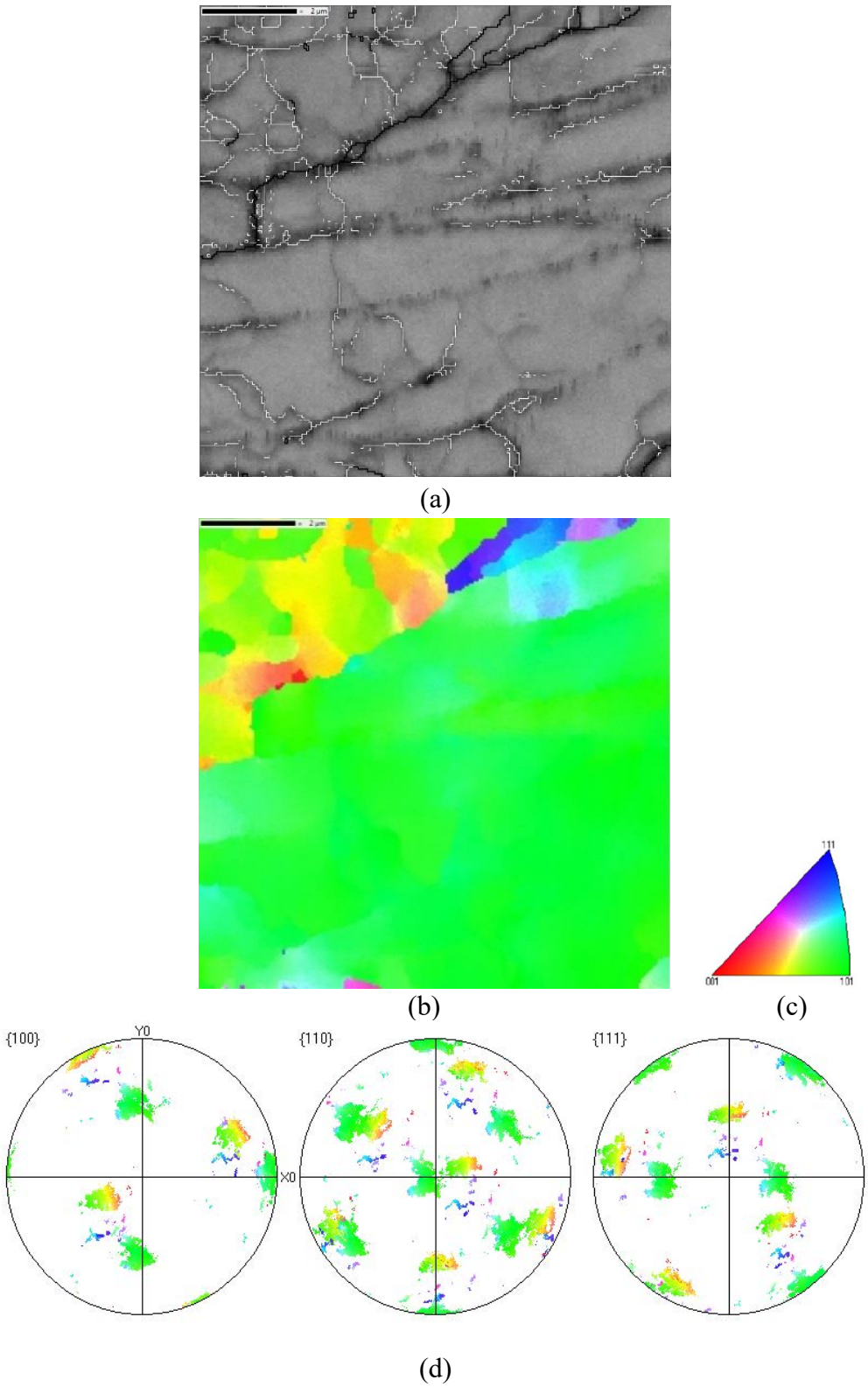

Figure 96. EBSD band contrast image (a) showing grain boundaries for AR medium deformation region site 1 LAGB (<2.5°) white lines and HAGBs (<15°) black lines. Orthogonal IPF map Z (b) for AR mid deformation site 1. IPF legend (c). Note: 2 µm scale bar is presented in the image. Pole figure map (d) of {100}, {110}, and {111}.

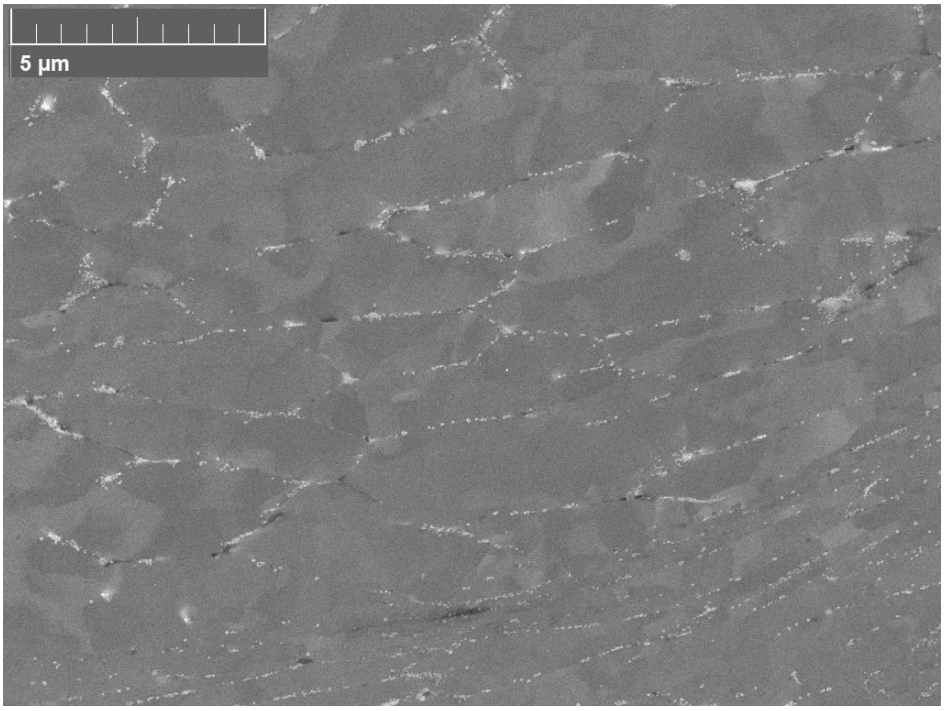

Figure 97. SEM micrograph taken in SE mode of 10 hr medium deformation region site 2

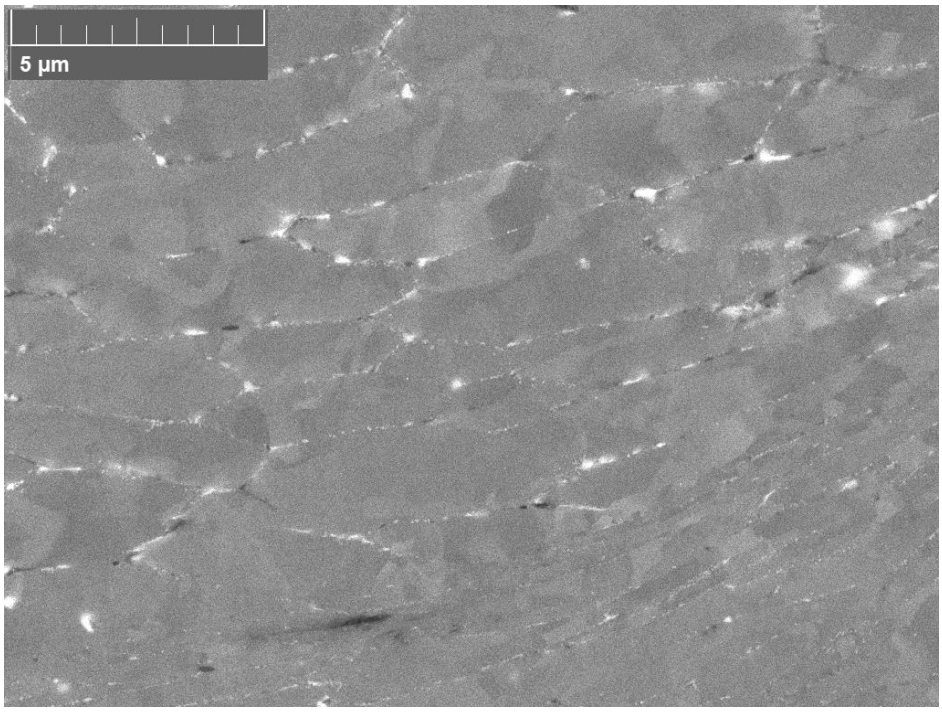

Figure 98. SEM micrograph taken in BSE mode of 10 hr medium deformation region site 2.

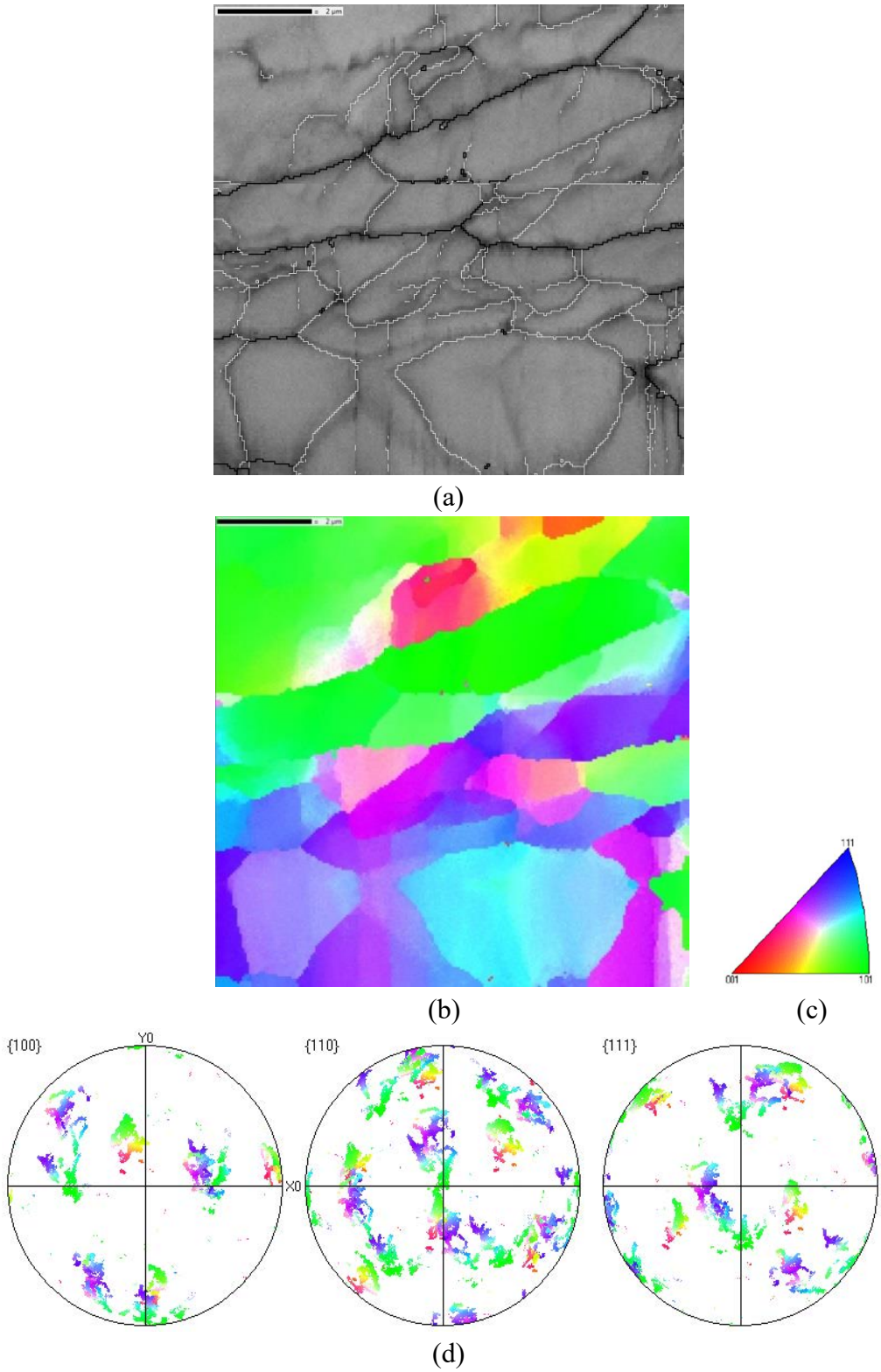

Figure 99. EBSD band contrast image (a) showing grain boundaries for 10 hr medium deformation region site 2 LAGB (<2.5°) white lines and HAGBs (<15°) black lines. Orthogonal IPF map Z, X, and Y (a, b, and c) for 10 hr Mid deformation site 2. IPF legend (d). Note: 2 µm scale bar is presented in the image. Pole figure map (d) of { 100 }, { 110 }, and { 111 }.

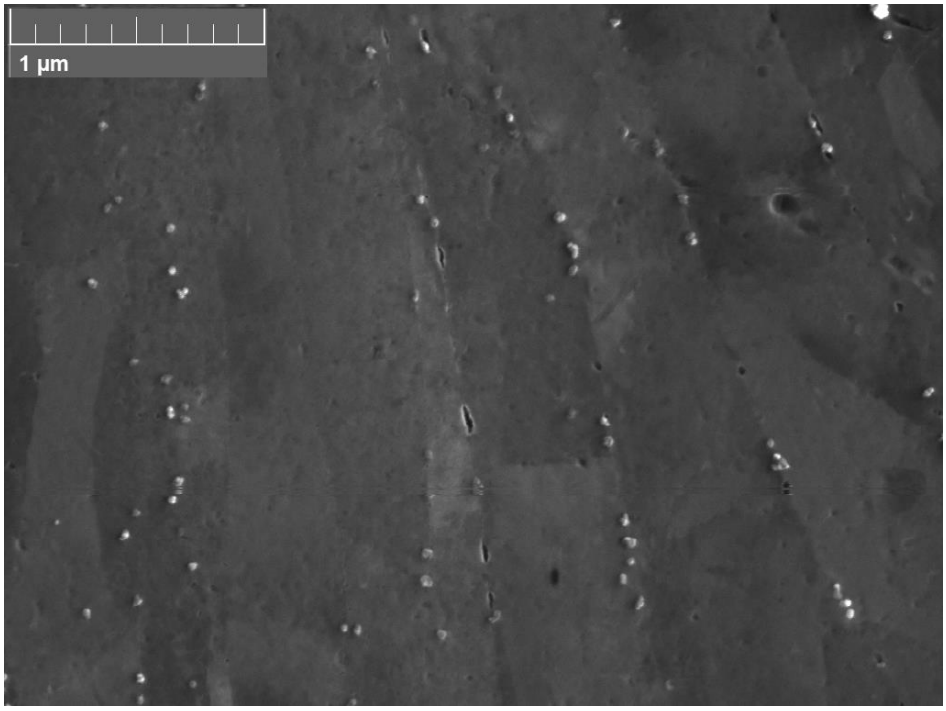

Figure 100. SEM micrograph taken in SE mode of AR High deformation site 1.

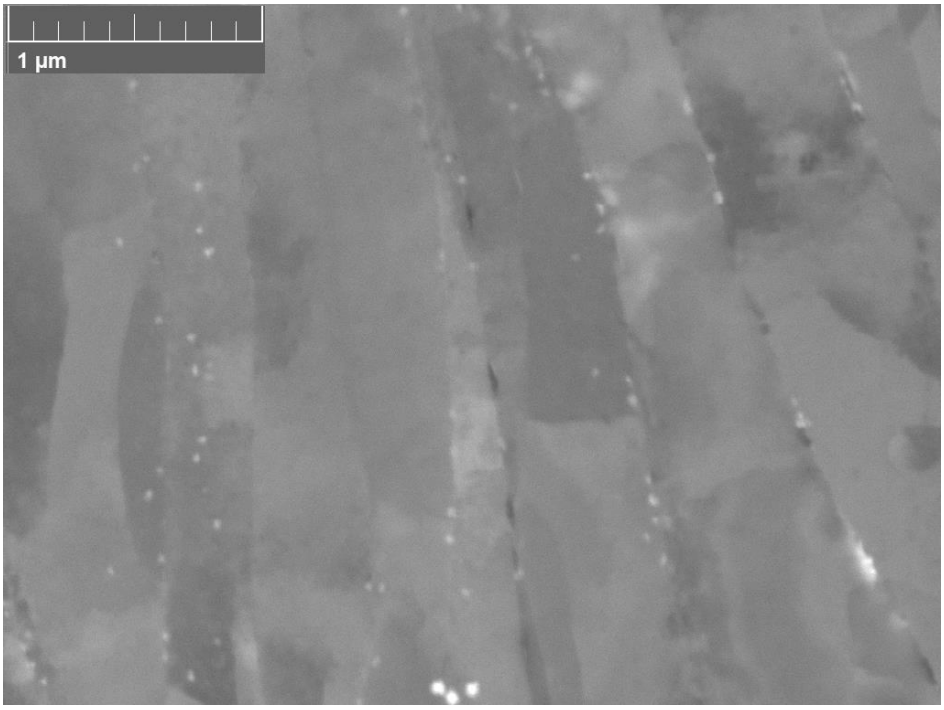

Figure 101. SEM micrograph taken in BSE mode of AR High deformation site 1.

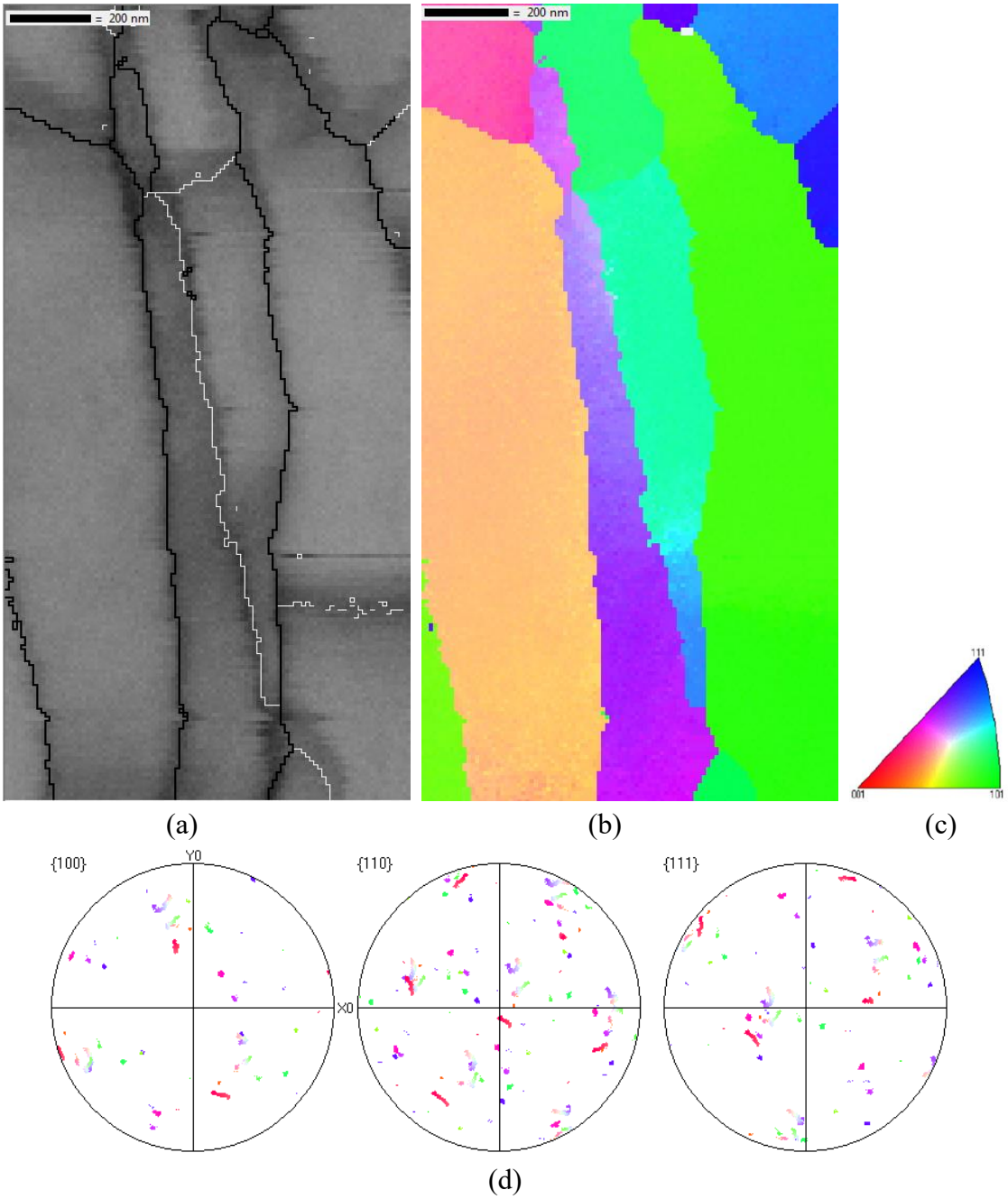

Figure 102. EBSD band contrast image (a) showing grain boundaries for AR high deformation region site 1 LAGB (<2.5°) white lines and HAGBs (<15°) black lines. Orthogonal IPF map Z (b) for AR high deformation site 1. IPF legend (c). Note: 200 nm scale bar is presented in the image. Pole figure map (d) of {100}, {110}, and {111}.

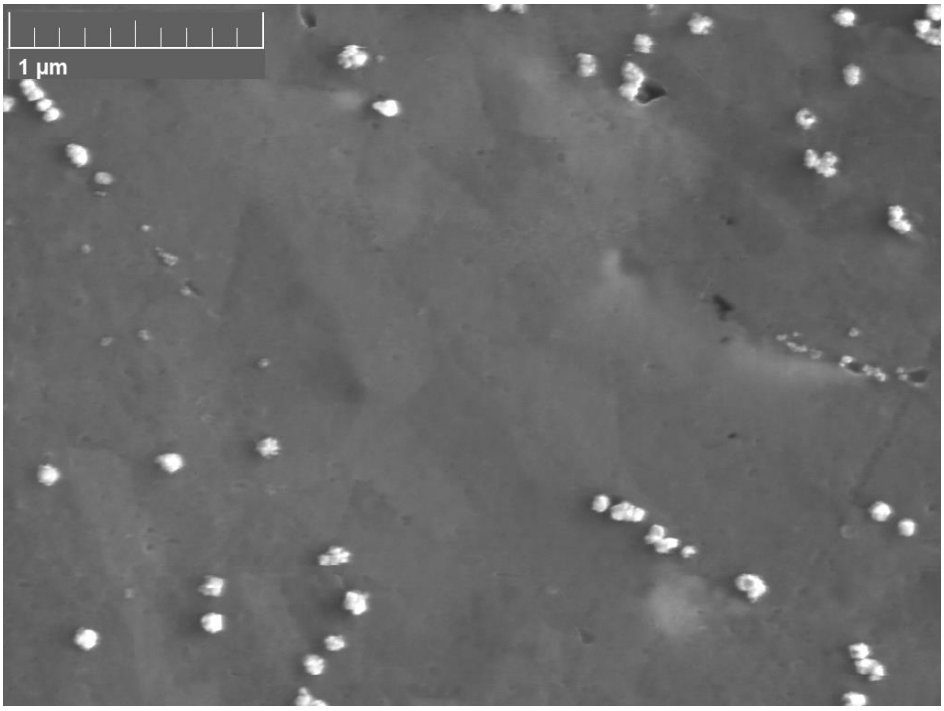

Figure 103. SEM micrograph taken in SE mode of AR high deformation region site 3.

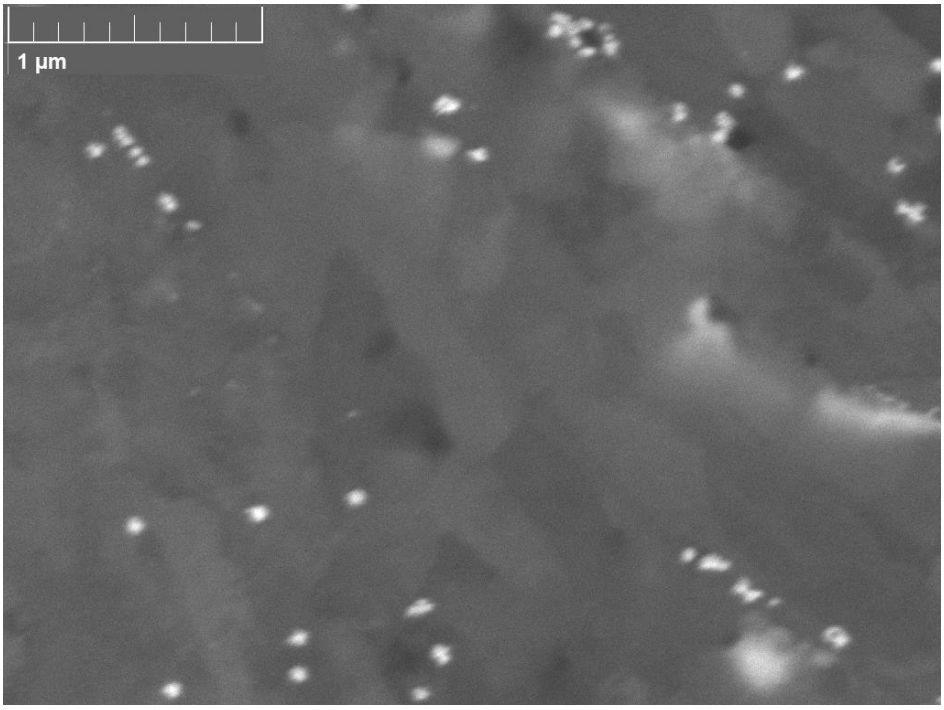

Figure 104. SEM micrograph taken in BSE mode of AR high deformation region site 3.

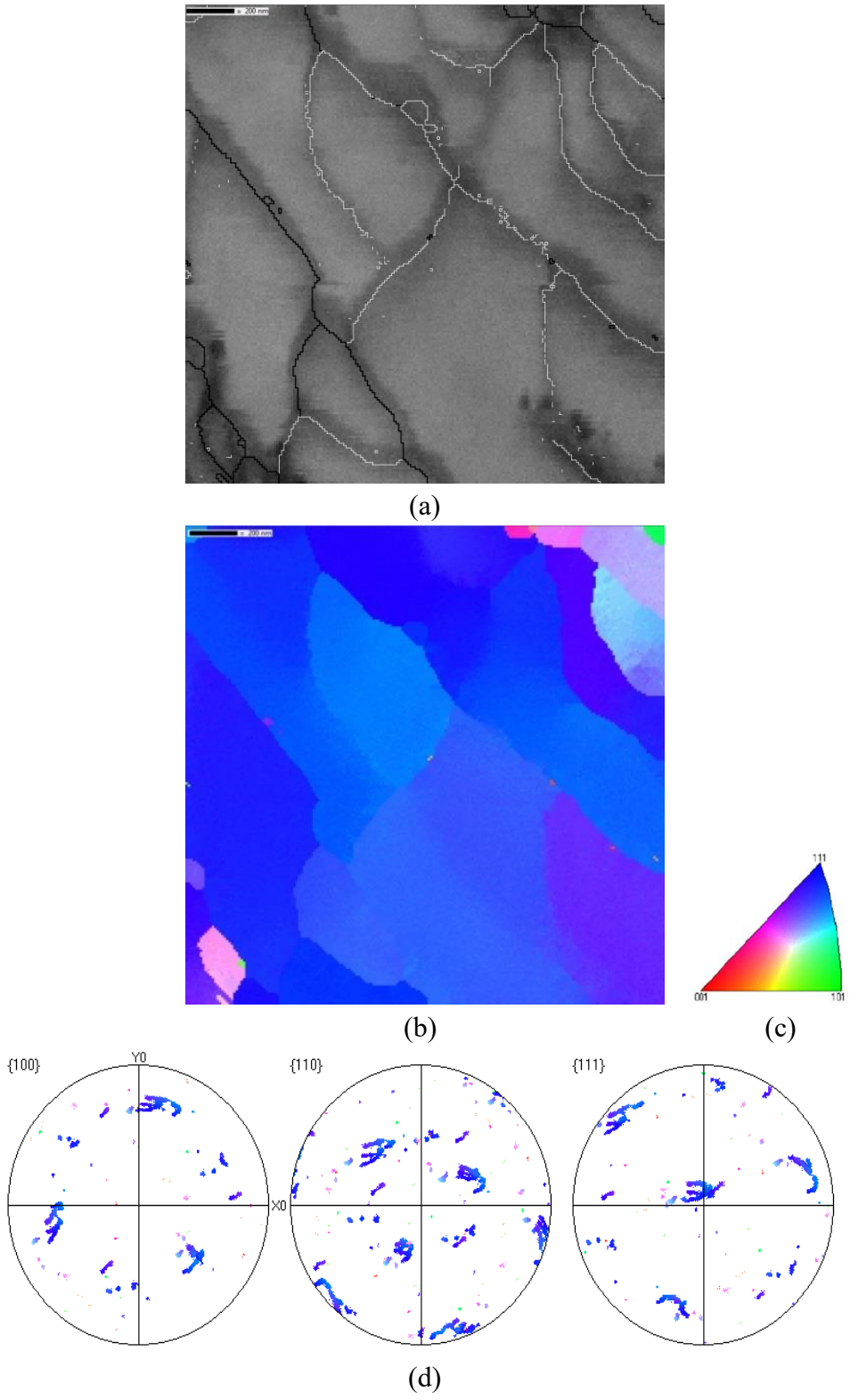

Figure 105. EBSD band contrast image (a) showing grain boundaries for AR high deformation region site 3 LAGB (<2.5°) white lines and HAGBs (<15°) black lines.Orthogonal IPF map Z (b) for AR high deformation site 3. IPF legend (c). Note: 200 nm scale bar is presented in the image. Pole figure map (d) of {100}, {110}, and {111}.

Appendix B – Grain Size data for high deformation regions

As-received High deformation regions

Nr.	Area [µm²]	d [µm]	Aspect ratio	Border grain	Grain ID
1	0.0997	0.35629	2.5309	corner	0
2	0.0851	0.32917	4.3922	edge	1
3	0.0183	0.15264	1.4553	edge	2
4	0.0173	0.14842	1.2436	edge	3
5	0.0219	0.16698	1.7145	edge	4
6	0.0803	0.31975	1.3161	corner	5
7	0.0261	0.1823	1.952	no	6
8	0.0871	0.33302	3.4152	no	7
9	0.1894	0.49107	1.1732	edge	8
10	0.0739	0.30674	3.4324	no	9
11	0.0128	0.12766	1.683	edge	10
12	0.0505	0.25357	1.6194	edge	11
13	0.0134	0.13062	2.1415	edge	12
14	0.5925	0.86856	3.0184	edge	13
15	0.0033	0.06482	2.2681	no	14
16	0.0602	0.27686	2.1143	no	15
17	0.006	0.0874	3.2787	no	16
18	0.0029	0.06077	1.2955	no	17
19	0.0923	0.34281	2.7661	edge	18
20	0.0367	0.21617	3.4864	edge	19
21	0.0749	0.30881	4.3944	no	20
22	0.0011	0.03742	1.7876	no	21
23	0.1315	0.40918	4.1952	edge	22
24	0.0021	0.05171	1.7801	no	23
25	0.0901	0.3387	1.8213	edge	24
26	0.0037	0.06864	1.9037	no	25
27	0.0036	0.0677	1.4108	no	26

1 hr High deformation regions

Nr.	Phase	Area [µm²]	d [µm]	Aspect ratio	Border grain
1	Aluminium	3.0936	1.9847	4.1093	corner
2	Aluminium	0.7708	0.99066	2.5063	edge
3	Aluminium	0.0896	0.33776	1.4974	corner
4	Aluminium	0.0024	0.05528	2.2328	no

5	Aluminium	0.7678	0.98873	4.6789	edge
6	Aluminium	0.0007	0.02985	1.0801	no
7	Aluminium	0.3434	0.66123	3.4431	edge
8	Aluminium	0.0334	0.20622	2.9316	edge
9	Aluminium	0.0009	0.03385	1.39	no
10	Aluminium	0.003	0.0618	4.8537	no
11	Aluminium	0.2804	0.59751	2.1723	edge
12	Aluminium	0.3016	0.61968	1.2588	corner
13	Aluminium	0.0792	0.31755	2.0412	corner
14	Aluminium	0.0033	0.06482	1.7766	no

10 hr High deformation regions

Nr.	Area [µm²]	d [µm]	Aspect ratio	Border grain	Grain ID
1	0.8384	1.0332	3.426	corner	0
2	0.2506	0.56487	8.1007	edge	1
3	0.2866	0.60408	3.6282	edge	2
4	1.672	1.4591	2.4509	corner	3
5	0.1452	0.42997	7.2683	corner	4
6	0.0214	0.16507	2.8884	no	5
7	0.0275	0.18712	3.8146	no	6
8	0.047	0.24463	1.9172	edge	7
9	0.0236	0.17334	1.7945	corner	8

100 hr High deformation regions

Nr.	Area [µm²]	d [µm]	Aspect ratio	Border grain	Grain ID
1	0.0582	0.27222	1.2411	edge	0
2	1.8772	1.546	2.0142	corner	1
3	0.424	0.73475	2.3956	edge	2
4	0.0937	0.3454	2.8872	no	3
5	0.1102	0.37458	2.5901	edge	4
6	0.1564	0.44625	2.908	corner	5
7	0.1262	0.40085	2.0666	edge	6